Electrically Controlled Manipulation Of Droplets On Smart Surfaces

From fundamental studies to practical applications

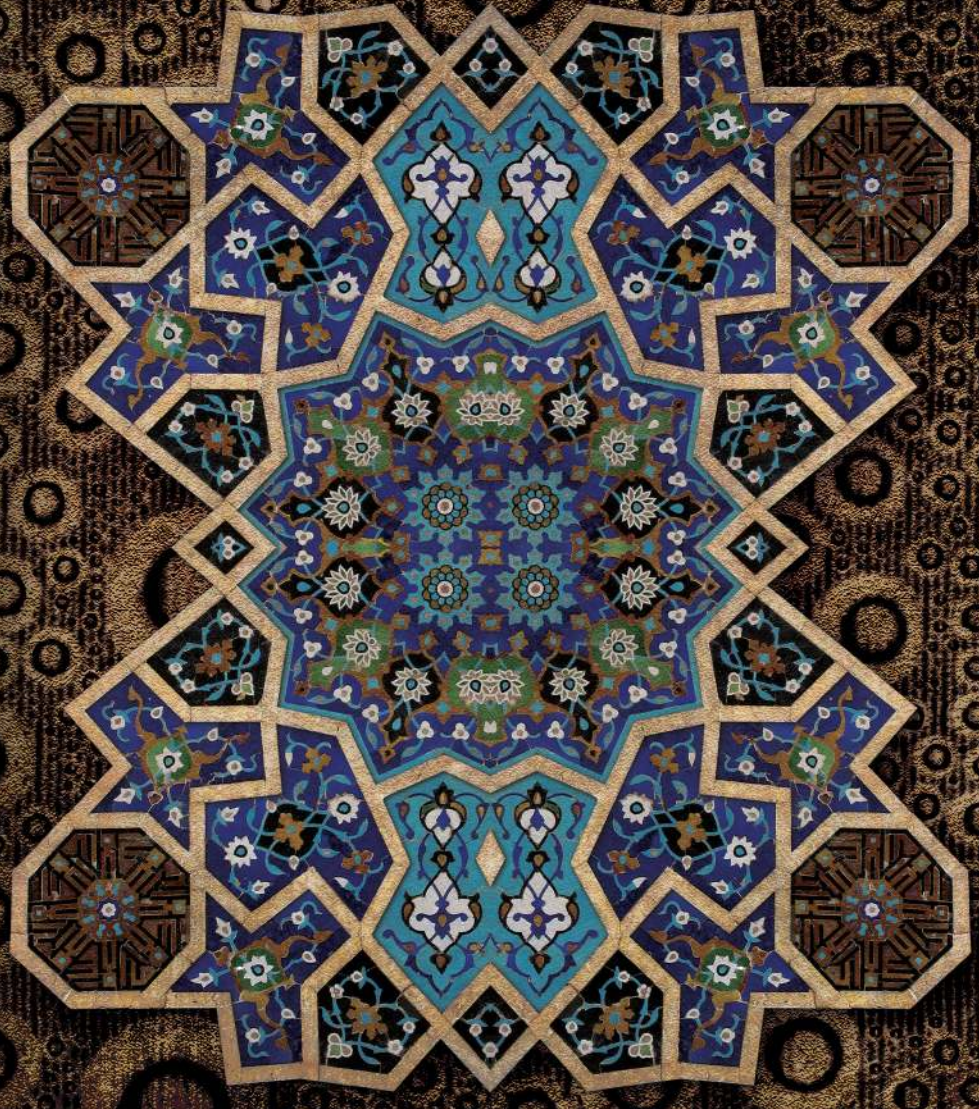

Davood Baratian

ELECTRICALLY CONTROLLED MANIPULATION OF DROPLETS ON SMART SURFACES

FROM FUNDAMENTAL STUDIES TO PRACTICAL APPLICATIONS

Davood Baratian

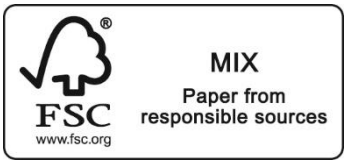
FSC
www.fsc.org
MIX
Paper from
responsible sources

ELECTRICALLY CONTROLLED MANIPULATION OF DROPLETS ON SMART SURFACES

FROM FUNDAMENTAL STUDIES TO PRACTICAL APPLICATIONS

DISSERTATION

to obtain
the degree of doctor at the University of Twente,
on the authority of the rector magnificus,
prof.dr.ir. A. Veldkamp,
on account of the decision of the Doctorate Board,
to be publicly defended
on the 2nd of December 2020 at 16:45 hours

by

Davood Baratian

born on the 21st of July 1986
in Esfahan, Iran

This dissertation has been approved by:

Promotor:

prof.dr. F.G. Mugele

Co-promotor:

dr. H.T.M. van den Ende

Graduation Committee

Prof. Dr. J.L. Herek	Chairman	University of Twente
Prof. Dr. F.G. Mugele	Promotor	University of Twente
Dr. H.T.M. van der Ende	Co-promotor	University of Twente
Dr. R. Ledesma Aguilar	Committee	University of Edinburgh
Prof. Dr.ir. C.R. Kleijn	Committee	TU Delft
Prof. Dr.ir. L. Lefferts	Committee	University of Twente
Dr. E.S. Kooij	Committee	University of Twente

This work is carried out at the Physics of Complex Fluids group at the University of Twente. This research is supported by the Dutch Technology Foundation STW, which is part of the Netherlands Organization for Scientific Research (NWO), partly funded by the Ministry of Economic Affairs.

Outside cover: An artistic impression reflecting rhythmic patterns of scrolling and interlacing foliage, tendrils, and flowers in Persian tiling artwork which associates the pattern of droplets on the surface with structured electrodes, and how it evolves in nature from randomness into regularity (background image). The element in the center is a tile masterpiece from "Atique" cathedral in Esfahan (9th century).
Inside cover: An artistic collage of dops in a wedge, featured on the front cover of *Soft Matter* journal.

ISBN: 978-90-365-5009-3
DOI: 10.3990/1.9789036550093

Author's contacts: davoodbaratian@gmail.com

To my family who are the true meaning of endless love …

Table of Contents

1

Introduction

This thesis is the study of controlling the behavior of water droplets on 'smart' surfaces. The word 'smart' refers to the surfaces with embedded electrodes over which the droplets are manipulated using electrical forces. The active control of the droplets is achieved by applying electrical potential over the electrodes, a technique known as 'electrowetting'. On one hand, to put the technological application of this concept into perspective, we describe the impact of electrical manipulation of droplets in dropwise condensation. On the other hand, the manipulation of a droplet, confined in a wedge structure, using electric fields, not only provides us with new insights in fundamental studies of droplet equilibrium morphology in complex geometries, but also helps to understand the different dynamic characteristics of drop motion which have a root in the interplay of electrical and capillary forces.

The motivation associated with using active electrical control for drop manipulation is explained in the first part of the introduction. Next is a short description of electrowetting fundamentals which explains how the electrical forces are applied to deform, thus move the droplets. Finally, this chapter ends with a guide through this thesis in more details.

1.1. Motivation

This thesis is an endeavor towards extending the potentials of a simple but unique technique, known as *electrowetting* (EW), which is widely used in the field of fluid mechanics, and physics of droplets. The capability of tuning the wettability of a surface by turning a knob, plus the active control on the shape, dynamics, and properties of a droplet against its contact surface, brings a lot of opportunities to dive deep into some questions which were not easy to address before. It helps us to find answers to some dilemmas which seem to be open questions for many years. It shows us that our understanding from this tool can be extended to the areas where there are still lots of room available for improvement, through overcoming the system's limitations using novel ideas out of our current techniques. It is an attempt to find new answers for long lasting questions.

Electrowetting phenomenon has been studied at least for a century by now [1]. Drop manipulation is one of the main areas where electrowetting provides control over various chemical or biological fluids in microfluidic platforms [2]–[4]. Later, "digital microfluidics" became a widely used technique for discretizing and manipulating of the droplets in a programmable way, to create, transport, divide, and merge the droplets [5], [6]. With that in mind, the research in this thesis can be divided in two main domains as it has been explained hereunder.

One of the less explored areas in the context of electrowetting is the study of an assembly of sessile droplets on the surface, as well as the properties of these droplets as a whole (known as Breath Figures). The condensate droplets on a cooling module, widely observable in heat exchangers, are good examples of such assemblies. These assemblies of droplets are of high relevance in painting, coating, and printing industries where the pigments or liquid chemicals are deposited on the

surface. These droplets cover the area either partially or completely. The question is: do we understand the physics behind the assembly of droplets when electric fields step into this picture? Can we expect a change in the droplet characteristics compared to no EW cases? If so, what can we learn when we dive deep into the evolutions of the assembly patterns and rearrangement of the droplets under electric fields (i.e. active external stimuli to the system)? In the first research domain, our goal is to find answers to the above questions. We consider the statistical properties associated with the assembly of droplets, and explore if the novel features, induced by EW, can be employed for practical applications where condensation plays an important role.

In the second domain, we use the same tool for investigating a different research question. Which shape does a droplet adapt to, in a non-conventional microchannel? One minimalistic example of these geometries is a wedge. How would a droplet settle between non-parallel walls? What if we use electrowetting to modify the wetting of surfaces in a wide range? The droplet needs to adapt its shape in order to comply to the new contact angle restriction. Are we able to control the droplet accurately in a wedge structure in this manner? If so, how can we use such manipulation in a practical way? In the second domain, the goal is to understand the configuration of a liquid droplet when it is confined in a complex rigid geometry. We extend the research in this domain further to study the motion and dynamics of the droplet in the wedge under electrowetting. Is there any characteristic feature with the motion of droplets under EW? How does the physics explain how the droplet moves with regards to the exerted forces?

1.2. Electrowetting principle

Electrowetting (EW), as suggested by the term itself, is a technique to increase the wettability of a liquid on a substrate, using electric fields [7]. Increasing the wettability implies spreading of the droplet on top of an electrode, and is manifested in reduction of the contact angle of the droplet with respect to the surface. The electrode is usually insulated by a thin dielectric layer to afford applying higher electric potential between the conductive droplet and the electrode, therefore Electrowetting On Dielectric – EWOD – is the most common form of using this technique in various applications.

Fig. 1 shows a classical electrowetting setting which consists of a flat electrode substrate, insulated with a thin layer of dielectric material. A droplet is placed on top in which a grounded wire is immersed (Fig. 1(a)). Since the droplet is conductive, the whole liquid is at the same potential, equal to zero. The droplet's contact angle on the surface is θ_y - known as Young contact angle - which is determined by the balance of forces acting on the contact line [8]. Fig. 2(a) shows these three forces: solid-liquid surface tension (σ_{sl}), solid-vapor surface tension (σ_{sv}), and liquid-vapor surface tension (σ_{lv}). At equilibrium, the balance of these forces determines the contact angle:

$$\sigma_{sl} - \sigma_{sv} + \cos\theta_y \, \sigma_{lv} = 0 \;\rightarrow\; \cos\theta_y = \frac{\sigma_{sv} - \sigma_{sl}}{\sigma_{lv}}$$

This relation is known as Young-Dupré equation.

When an electrical potential is applied between the two electrodes, a part of the energy provided by the battery is stored in the dielectric layer by creating an electric field which is formed in the dielectric layer, as depicted in Fig. 1(b). This electrical energy is equal to $E_e = \frac{1}{2} C U^2$ where U is the applied potential, and C is the

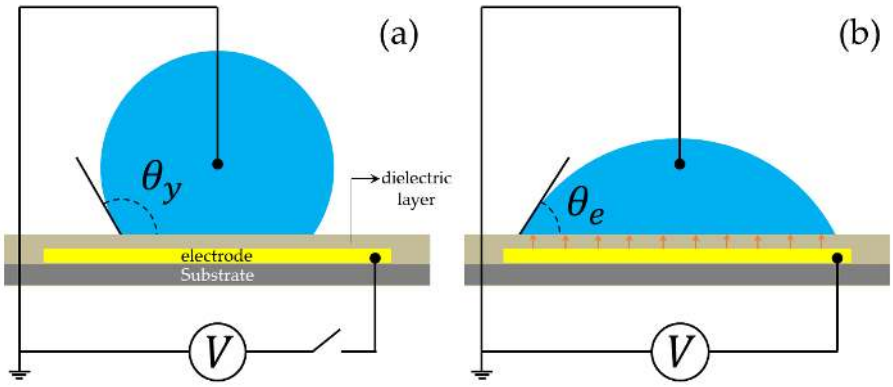

Fig. 1: Schematics showing the electrowetting principle in a classical setting. (a) A droplet placed on top of a substrate, creating a contact angle of θ_y knows as the Young contact angle. (b) An electrical potential is applied between the two electrodes and an electric field is created within the dielectric layer. The contact angle decreases to increase the capacitance of the system, in favor of enhancing the stored energy in the electric field.

system capacitance. The latter scales with the contact area of the droplet with the surface: $C = cA_{sl} = \frac{\varepsilon\varepsilon_0}{d}A_{sl}$. Here ε_0 is the vacuum permittivity, ε and d are the permittivity and thickness of the dielectric material respectively, and A_{sl} is the contact area of the droplet with the dielectric surface

The system would be more energetically favorable when it stores more energy in its electric field. Therefore, the liquid electrode (i.e. droplet) enhances the capacitive energy of the system by spreading over the surface to increase its contact area A_{sl}. However, the cost of this deformation is the increase of the surface energy since the droplet increases its surface area, as its volume if fixed. Eventually there is a balance between the gained electric energy and the surface energy, and the droplet reaches a new equilibrium shape where its contact angle is adjusted accordingly as depicted in Fig. 1(b). Under electrowetting, the contact angle is determined by the balance of solid-liquid, solid-vapor, and liquid-vapor surface tensions, plus the electrostatic stress which has been stepped into the force balance scheme, as depicted

in Fig. 2(b). In a way, electrowetting modifies the solid-liquid surface tension, and a new term, which is the sum of σ_{sl} and the electrostatic stress is introduced which is called 'apparent' solid-liquid surface tension. Hence the equilibrium contact angle, out of the new force balance scheme is described with Young-Lippman equation:

$$\cos\theta_e = \cos\theta_y + \frac{1}{2}\frac{c}{\sigma_{lv}}U^2$$

This equation related the contact angle under electrowetting to the Young contact angle and the non-dimensional electrowetting number $\eta = \frac{1}{2}\frac{c}{\sigma_{lv}}U^2$. On one hand, it implies that the droplet's contact angle can be predicted at a given applied electric voltage. On the other hand, by measuring the contact angle as a function of voltage, we can extract the properties of the dielectric layer, e.g. the layer thickness d once the surface tension and the dielectric constant values are known. This relation is valid up to the limit of contact angle saturation [7].

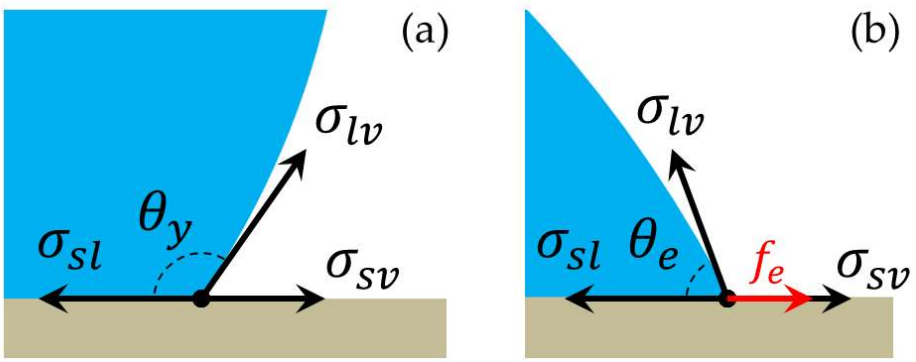

Fig. 2: The balance of forces acting on the triple contact line. (a) θ_y is the Young contact angle which is determined by the balance of solid-liquid, solid-vapor, and liquid-vapor surface tensions acting on the contact line. (b) Upon applying electric potential, an extra electric tension is added to the force balance equation which leads to spreading of the droplet over the surface. Due to the volume conservation, the contact angle of the droplet is reduced to adapt to the (apparent) electrowetting angle θ_e.

It is worth mentioning that the electrostatic force which causes spreading of the droplet, is not acting on a single point, i.e. the triple contact point, but on the droplet interface in the vicinity of the contact line, over a length scale comparable to the thickness of the dielectric layer which is typically $100\ nm - 10\ \mu m$. This implies that while the macroscopic (apparent) contact angle is observed as θ_e under electrowetting, the microscopic contact angle at micro(nano)-scale remains the same as θ_y. The Young contact angle is essentially defined by the material properties of the surface and the liquid in their ambient.

1.3. AC Electrowetting

Electrowetting experiments are conducted either by applying DC or AC voltage between the electrodes. In DC electrowetting, the accumulation of the charges at the electrode surfaces, and counter ions at the liquid-solid interface takes place. As a result, a uniform electric field forms in the dielectric layer (note that near the triple line, the electric field fringes are perpendicular to the drop's free surface).

However, in AC electrowetting, an alternating voltage (at a frequency of f) is applied between the electrodes, therefore, the charges on the electrode as well as the ions at the liquid-solid interface change sign all the time. Note that in any case, the attraction of ions towards the counter-charges results in the same spreading of droplet, for both positive and negative charges. An alternating electrical actuation, e.g. a sinusoidal wavefront, exerts harmonic tangential force to the contact line. Consequently, the drop contact line undergoes an oscillation at a frequency which is twice the AC voltage frequency ($2f$) [9]. Such harmonic movements facilitate the contact line to overcome the resistive pinning forces (originated from the chemical heterogeneity) on the surfaces much easier. The contact angle hysteresis (CAH)

decreases [10], [11]. Hence AC EW enhances the mobility of droplet by suppressing the contact angle hysteresis, apart from decreasing the contact angle.

1.4. Guide through the thesis

After this introduction, **Chapter 2** describes how EW modifies the distribution of droplets on the condensing surface by aligning the drops along the electrode structure and by enhancing coalescence. Both these effects are governed by the electrostatic energy landscape which can be modeled by numerical calculations. This chapter also provides practical insights towards optimizing applications involving dropwise condensation and discusses how to control the condensate patterns.

Chapter 3 is the follow-up study of the chapter 2 through focusing on the significant variation of statistical characteristics of the ensemble of droplets. These variations are manifested as the result of the migration and coalescence of condensate drops, under EW. This chapter explains the self-similarity of condensate patterns and shows how this feature deviates from its classical trend, once the coalescence cascades sets in under EW, and consequently the drop size distribution undergoes a different evolution. Furthermore, our results reveal other novel features which suggest that the condensation performance is expected to increase under EW.

Chapter 4 is a focus on the applied perspective of using EW for active controlling of condensation process, aimed on enhancing the heat transfer rates. We show that dropwise condensation under alternating electric fields manifests significant changes in thermal characteristics as well as shedding dynamics, compared to the classical dropwise condensation. In absence of Non-Condensable Gases (NCG's), we measure enhanced heat transfer with respect to the control, in correlation with increased shedding dynamics of condensate droplets

For the next two chapters, there is a slight twist in the research question where we use EW to study a liquid droplet confined between non-parallel rigid walls. In **chapter 5**, we address the dilemma of the equilibrium morphology of liquid drops exposed to geometric constraints. Under quasistatic conditions, the complex equilibrium shape of the droplet is monitored while the drop position, as well as configuration is controlled through applying an electric voltage. The analysis of forces imposed all over the drop's interface, shows a net force of zero. We show how the geometric constraint and electrowetting can be used to position droplets inside a wedge in a controlled way, without mechanical actuation.

In **chapter 6** we study the mobility of droplets in a wedge geometry under EW, and the subsequent reconfiguration of the droplet once the EW actuation is either applied or removed. We explore the different mobility regimes observed in droplet translation, and explain the characteristics of relaxation regimes by the status of the lubrication layer (between the droplet and the substrate) during the motion. Using a combination of experiments and numerical simulations, we show that the cross-over between these regimes arises from the interplay between the small-scale dynamics of the thin film of ambient fluid and the large-scale motion of the droplet. On the practical side, our study can help the rational design of devices based on EW-driven droplet transport.

Chapter 7 gives the overall conclusions out of the work in this thesis, followed by outlooks, describing the potential ideas on how to extend this work and proceed towards more practical applications or fundamental studies.

References

[1] G. Lippmann, "Relations entre les phénomènes électriques et capillaires." Gauthier-Villars Paris, France:, 1875.

[2] M. G. Pollack, R. B. Fair, and A. D. Shenderov, "Electrowetting-based actuation of liquid droplets for microfluidic applications," *Appl. Phys. Lett.*, vol. 77, no. 11, pp. 1725–1726, 2000.

[3] J. Lee and C.-J. Kim, "Liquid micromotor driven by continuous electrowetting," in *Proceedings MEMS 98. IEEE. Eleventh Annual International Workshop on Micro Electro Mechanical Systems. An Investigation of Micro Structures, Sensors, Actuators, Machines and Systems (Cat. No. 98CH36176*, 1998, pp. 538–543.

[4] W. C. Nelson and C.-J. 'CJ' Kim, "Droplet Actuation by Electrowetting-on-Dielectric (EWOD): A Review," *J. Adhes. Sci. Technol.*, vol. ahead-of-p, no. ahead-of-print, pp. 1–25, 2012.

[5] S. K. Cho, H. Moon, and C.-J. Kim, "Creating, transporting, cutting, and merging liquid droplets by electrowetting-based actuation for digital microfluidic circuits," *J. Microelectromechanical Syst.*, vol. 12, no. 1, pp. 70–80, 2003.

[6] M. G. Pollack, "Electrowetting-based microactuation of droplets for digital microfluidics." Duke University, 2001.

[7] F. Mugele and J. Heikenfeld, *Electrowetting: Fundamental Principles and Practical Applications*. John Wiley & Sons, 2018.

[8] P.-G. de Gennes, F. Brochard-Wyart, and D. Quéré, *Capillarity and Wetting Phenomena*. New York, NY: Springer New York, 2004.

[9] D. Mampallil, H. Burak Eral, A. Staicu, F. Mugele, and D. Van Den Ende, "Electrowetting-driven oscillating drops sandwiched between two substrates," *Phys. Rev. E - Stat. Nonlinear, Soft Matter Phys.*, vol. 88, no. 5, pp. 1–8, 2013.

[10] F. Li and F. Mugele, "How to make sticky surfaces slippery: Contact angle hysteresis in electrowetting with alternating voltage," *Appl. Phys. Lett.*, vol. 92, no. 24, pp. 2008–2010, 2008.

[11] T. D. J. C. M. Mannetje, C. U. Murade, D. Van Den Ende, and F. Mugele, "Electrically assisted drop sliding on inclined planes," *Appl. Phys. Lett.*, vol. 98, no. 1, pp. 10–13, 2011.

2

Electrically Controlled Evolution of Drop Condensation Patterns

We show that electrowetting (EW) with structured electrodes significantly modifies the distribution of drops condensing onto flat hydrophobic surfaces by aligning the drops and by enhancing coalescence. Numerical calculations demonstrate that drop alignment and coalescence are governed by the drop-size dependent electrostatic energy landscape that is imposed by the electrode pattern and the applied voltage. The resulting periodicity of the droplet pattern under EW can be further controlled by simply tuning the electrode geometry. We anticipate that this study will trigger a general theoretical analysis of drop condensation patterns in arbitrary energy landscapes. Furthermore, provides practical insights towards optimizing applications involving dropwise condensation.

This chapter has been adapted from the publication:
D. Baratian, R. Dey, H. Hoek, D. Van Den Ende, and F. Mugele, "Breath Figures under Electrowetting : Electrically Controlled Evolution of Drop Condensation Patterns," *Phys. Rev. Lett.*, vol. 120, no. 21, p. 214502, 2018.

2.1. Introduction

Dropwise condensation of water vapor is intrinsic to natural phenomena like dew formation [1] and dew or fog harvesting by animals (e.g., Namib Desert beetle) and plants such as Namib Desert plants [2]. Dropwise condensation of vapor is also utilized in various technologies like water-harvesting systems [3], heat exchangers for cooling systems [4], and desalination systems [5]. The efficacy of these technologies depends on the nucleation, coalescence, and growth of the condensate droplets on surfaces and on their subsequent shedding [6], [7]. The pattern formed by condensing droplets is classically referred to as a breath figure due to its similarity with the pattern formed by breathing on a cold surface [8]–[10].

To improve the efficiency of the dropwise condensation process, it is essential to control the underlying breath figure characteristics. In general, dropwise condensation can be controlled by regulating the mobility of the droplets on the surface. Enhanced dropwise condensation has been studied on superhydrophobic nanostructured surfaces [11]–[14], on superhydrophobic microgrooved and wettability-patterned surfaces [15], [16], and on liquid impregnated textured surfaces [17], [18]. However, in all the studies so far, droplet mobility is altered passively by tailoring the characteristics of the condensing surface through chemical or topographical patterning.

In this study, we go beyond such passive approaches and use an alternating (AC) electric field in an electrowetting (EW) configuration with patterned electrodes [19] to actively control the breath figure evolution on otherwise homogeneous hydrophobic surfaces. We demonstrate that EW significantly modifies the distribution of condensate drops using electrical forces and alters the statistical characteristics of the entire ensemble of droplets from those established for classical

breath figures with randomly distributed drops. The breath figure evolution under EW is characterized by size-dependent alignment of the condensate drops at the minima in the corresponding electrostatic energy landscapes and enhanced coalescence.

2.2. Experiments

The experimental setup consists of a condensation chamber and measuring instruments (see Fig. 1). Vapor is produced in a boiler which is heated by a hot plate (RCT Basic, IKA labortechnik). The water inside the boiler is bubbled with pressured air (08816-air-550R-plus, Sera) to produce a constant stream of vapor-air mixture at $36 \pm 1\,°C$ and 2 lit/min, monitored by a flowmeter (AWM5101VN flowmeter,

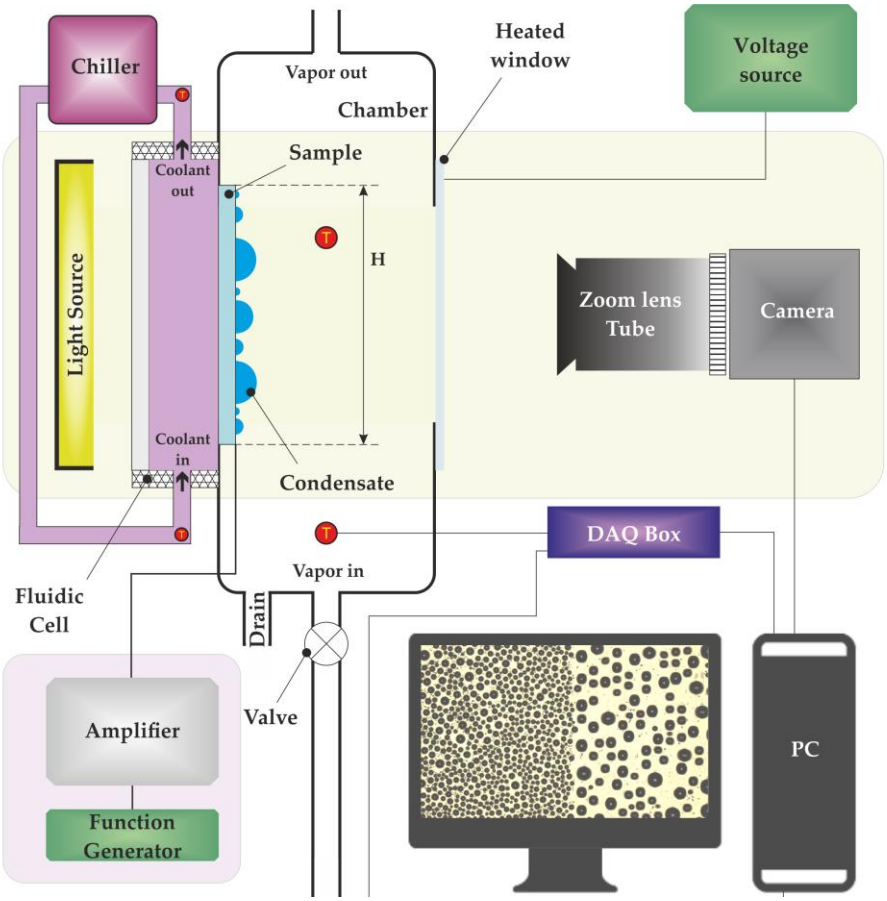

Fig. 1: Details of the experimental setup. Experiments are conducted both without EW actuation (control) and under EW on identical substrates and under identical conditions. The orientation of gravity is from top to bottom along the direction of the interdigitated electrodes.

Honeywell). Vapor enters to the condensation chamber from a bottom inlet and exits from an outlet in the top. The temperatures are measured by means of thermistors (TCS651, AmsTECHNOLOGIES) and a LabVIEW script. Multiple thermistors are located at multiple points to monitor the temperature of ambient, the heated water in the boiler, and the vapor at the chamber inlet, and at the vicinity of the surface. The sample is mounted vertically on a side window of a transparent fluidic cell (made from Perspex) in which the coolant is constantly recirculated by a chiller (Haake-F3-K, Thermo Fisher Scientific) controls the sample temperature. The coolant maintains the temperature of the substrate at 25 °C which is lower than the dew point of the vapor, and provides a supercooling of 11 ± 1 °C. For the condensation under EW, an AC voltage is applied between the interdigitated electrode pair at a frequency of 1 kHz using a function generator (Agilent 33220A) and a voltage amplifier (Trek PZD700A). The dropwise condensation process on such a vertically placed substrate, both without EW and under EW, is visualized at fixed surface temperature, vapor temperature, and vapor flow rate (see supplemental movie in [20]).

Stripe patterns of transparent interdigitated ITO electrodes are fabricated using photolithography on a glass substrate. The electrode pattern consists of ITO stripes and intermediate gaps of $w_e = w_g = 200\ \mu m$ in width, and H = 40 mm in length (Fig. 2). The pitch of the electrode pattern, i.e. the center-to-center distance between two adjacent electrode stripes, is l = 400 μm (see the blow-up in Fig. 2). The glass substrate containing the electrode pattern is coated by a 2 μm Parylene-C layer (PDS2010, SCS Labcoter) using chemical vapor deposition (CVD) technique to electrically insulate the electrodes. Thereafter, the substrate is further coated by a thin polymer layer (CytopTM, Asahi Glass Co., Ltd.) following a dipcoating procedure, which renders the surface hydrophobic. The substrate is then mounted

vertically inside a condensation chamber, such that gravity is oriented from top to bottom along the direction of the interdigitated electrodes (Fig. 2).

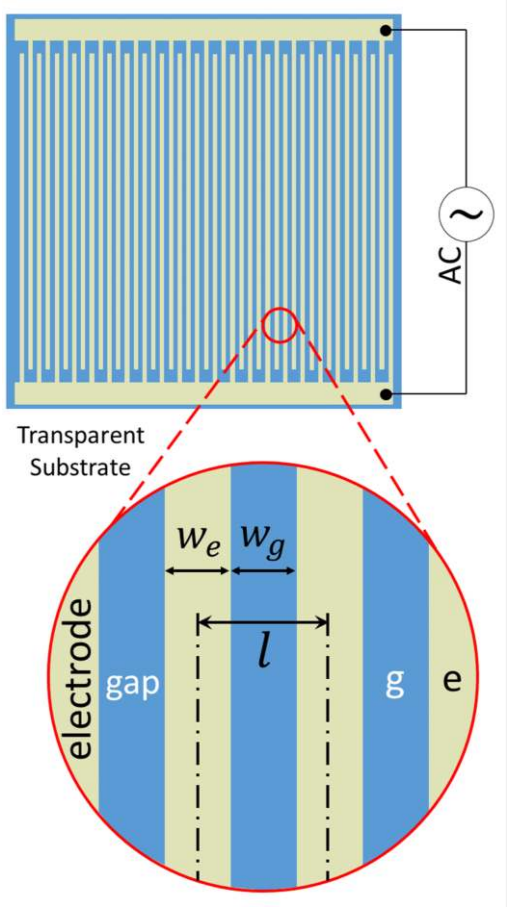

Fig. 2: The substrate used for the condensation experiments. The electrode pattern consists of ITO stripes and intermediate gaps of $w_e = w_g = 200\ \mu m$ in width, and H = 40 mm in length. The pitch of the electrode pattern, i.e. the center-to-center distance between two adjacent electrode stripes, is l = 400 μm.

2.3. Phenomenology

The condensation experiments are performed on a glass plate coated by a hydrophobic dielectric polymer film (Fig. 3(a)). The glass substrate contains a stripe pattern of transparent interdigitated ITO electrodes (Fig. 3(a)). An AC voltage with

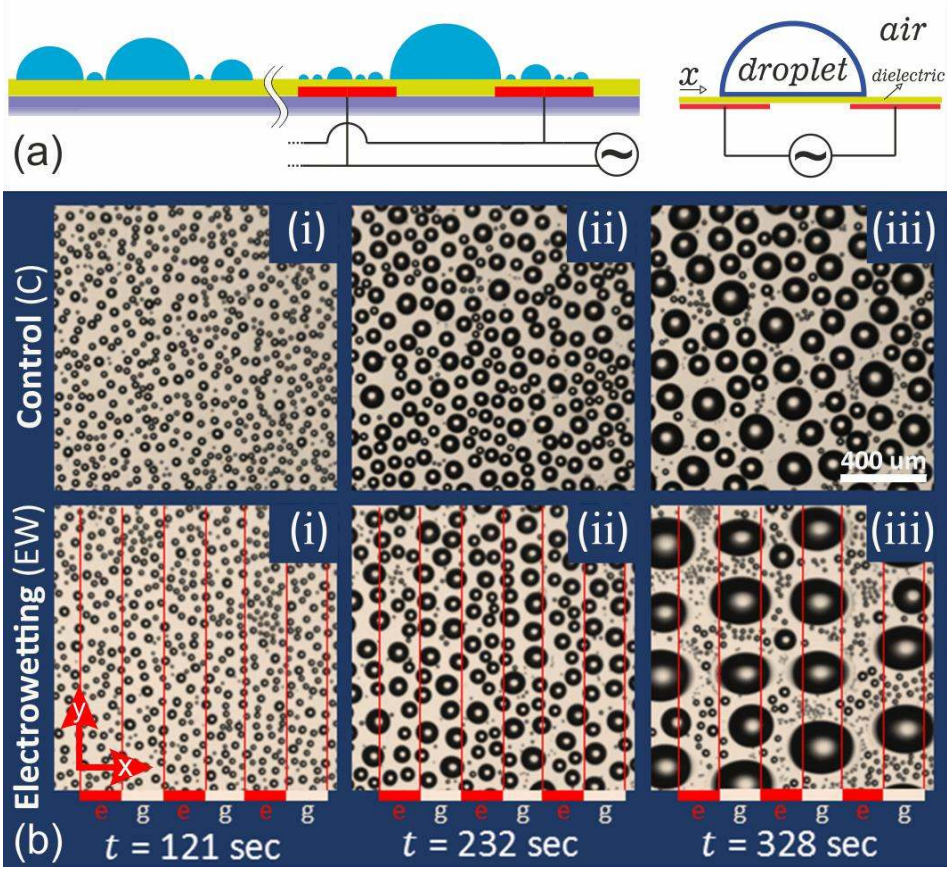

Fig. 3: (a) Schematic of the substrate used for the condensation experiments. Transparent interdigitated ITO electrodes (red) are patterned on the glass substrate (purple), which is then coated with a hydrophobic dielectric polymer film (green). A schematic of a condensate droplet under EW is also shown. (b) Comparison between breath figures without EW i.e. control (C) (C(i)–C(iii)) and under EW (Urms = 150 V; f = 1 kHz) (EW(i) – EW(iii)) at different time (t) instants. The electrode-gap (e, g) geometry underneath the dielectric film is indicated by the solid red and white lines. Gravity points from top to bottom, i.e. along the negative y direction.

a frequency of $f = 1\,kHz$ and a maximum amplitude of 150 V U_{rms} is applied. Condensation experiments are performed both without EW (control) and under EW on identical substrates and under identical experimental conditions. The condensation on the control and EW-functionalized surfaces is monitored using a high-resolution camera. We denote the time instant at which reliably detectable condensate drops of radius ~5 μm are detected for the first time as t = 0 s (for the image analysis procedure see appendix 3B). At the beginning, small drops appear at random locations on both the control and the EW-functionalized surfaces and grow without coalescence (Fig. 3(b), C(i), EW(i)). As the drops grow and then coalesce

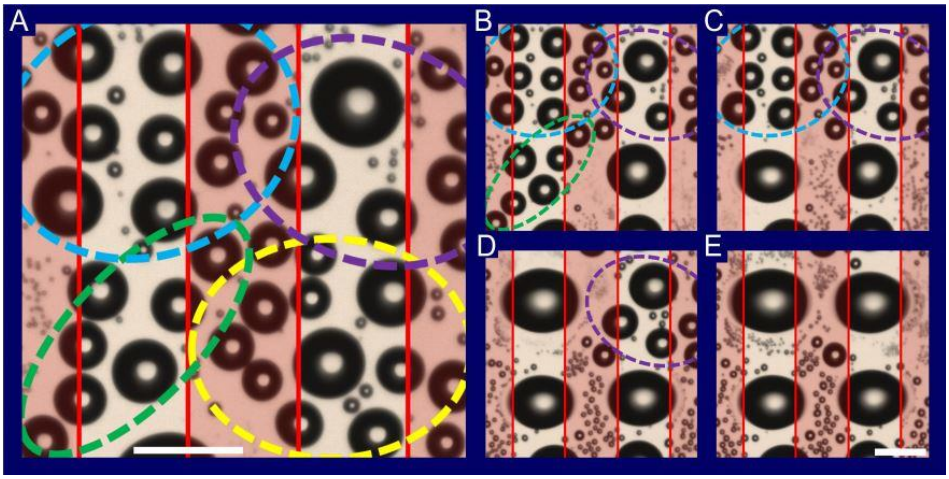

Fig. 4: Snapshots showing EW-induced rapid coalescence events (coalescence cascades) resulting in droplets having diameters comparable to the electrode spacing, and aligned above the gap-centers. The droplets involved in a particular coalescence cascade are identified in (A) by a colored dashed line. (A)-(B) show the creation of a large droplet due to the coalescence cascade involving the droplets grouped by the yellow dashed line in (A). Similarly, (B)-(C), (C)-(D), and (D)-(E) show the same for the droplets grouped by the green dashed line, the cyan dashed line, and the purple dashed line respectively. The individual coalescence events constituting a coalescence cascade cannot be captured using the imaging frame rate. The droplets created by the coalescence cascades are approximately monodisperse, with vacant areas around them. The bars in the images represent 200 μm.

frequently, the drops on the EW-functionalized surface initially align parallel to the electrode edges, displaced towards the gap centers (Fig. 3(b), EW(ii)).

As the droplets grow further and exceed a critical size, sequences of rapid coalescence events (coalescence cascades) create approximately monodisperse drops bridging the gap (w_g) between two adjacent electrodes and aligned along the gap centers (Fig. 3(b), EW(iii); Fig. 4). At the same time, the drops on the control surface remain randomly distributed, displaying more polydispersity and smaller average sizes (Fig. 3(b), C(iii)). The transformation in the breath figure under EW (Fig. 3(b), EW(ii)–EW(iii)) occurs within a narrow transition period. Eventually, the gravity-induced drop shedding occurs earlier under EW versus the control surface (Fig. 5).

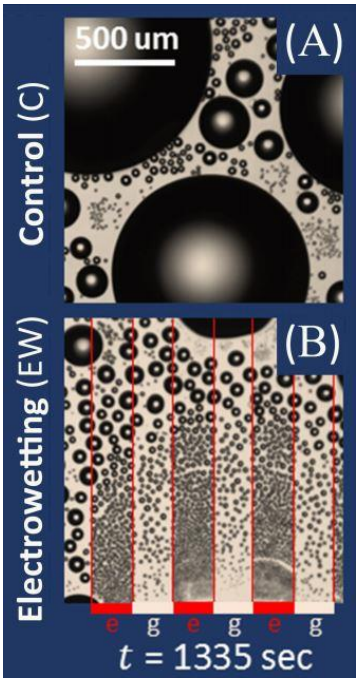

Fig. 5: The condensate drops shed earlier, pulled by gravity under AC-EW (B), compared to the control (A), due to the AC-EW-induced enhanced droplet growth as well as reduction of effective contact angle hysteresis. The drops continue to grow on the control surface (A), while gravity-induced shedding events set in at a smaller drop size on the EW-functionalized surface (B).

2.4. Results

To quantify the unique distribution of droplets under EW, we project the droplets in the breath figure onto unit cells of width equal to the pitch (l) of the electrode pattern and ranging from one electrode center to the adjacent electrode center. Within a unit cell, we calculate the variation of the droplet area fraction ($\bar{S}_x$) along the lateral (x–) direction. Here, $\bar{S}_x = \sum_i A_i/A_{uc}$, where A_i is the i^{th} droplet contact area along a line parallel to the electrode edges (y-direction), and A_{uc} is the unit cell area; $\langle \bar{S}_{\bar{x}} \rangle$ represents the average over all unit cells in the breath figure, and $\bar{x} = x/l$. The temporal evolution of $\langle \bar{S}_{\bar{x}} \rangle$ shows the gradual development of two similar peaks from the gap edges (Fig. 6(a)). The development of these local maxima describes the alignment of the condensate drops on both sides of the gap center (Fig. 3(b), EW(ii)). In contrast, the corresponding $\langle \bar{S}_{\bar{x}} \rangle$ distribution on the control surface remains uniform (Fig. 7).

At any time instant, the peak value $\langle \bar{S}_{\bar{x}} \rangle_p$ describes the maximum droplet coverage. Over time, as the droplets coalesce and grow (see Video), $\langle \bar{S}_{\bar{x}} \rangle_p$ gradually increases (red symbols in inset (I) in Fig. 6(a)), and concurrently, the locations of the two peaks gradually shift towards the gap center (symbols in Fig. 6(b)). As the average radius of the drops constituting a peak $\langle r \rangle_p$ exceeds a critical value $\langle r \rangle_p^* \sim 0.3 w_g$, the coalescence cascades set in. Consequently, a new peak in emerges at the gap center (purple symbols in inset (I) in Fig. 6(a)) while the side peaks start to decay; this marks the beginning (t_b^*) of the transition period. Within the transition period, the side peaks disappear and the peak at the gap center survives in the end (t_e^*) (Fig. 6(a) and inset (I), and Fig. 6(b)).

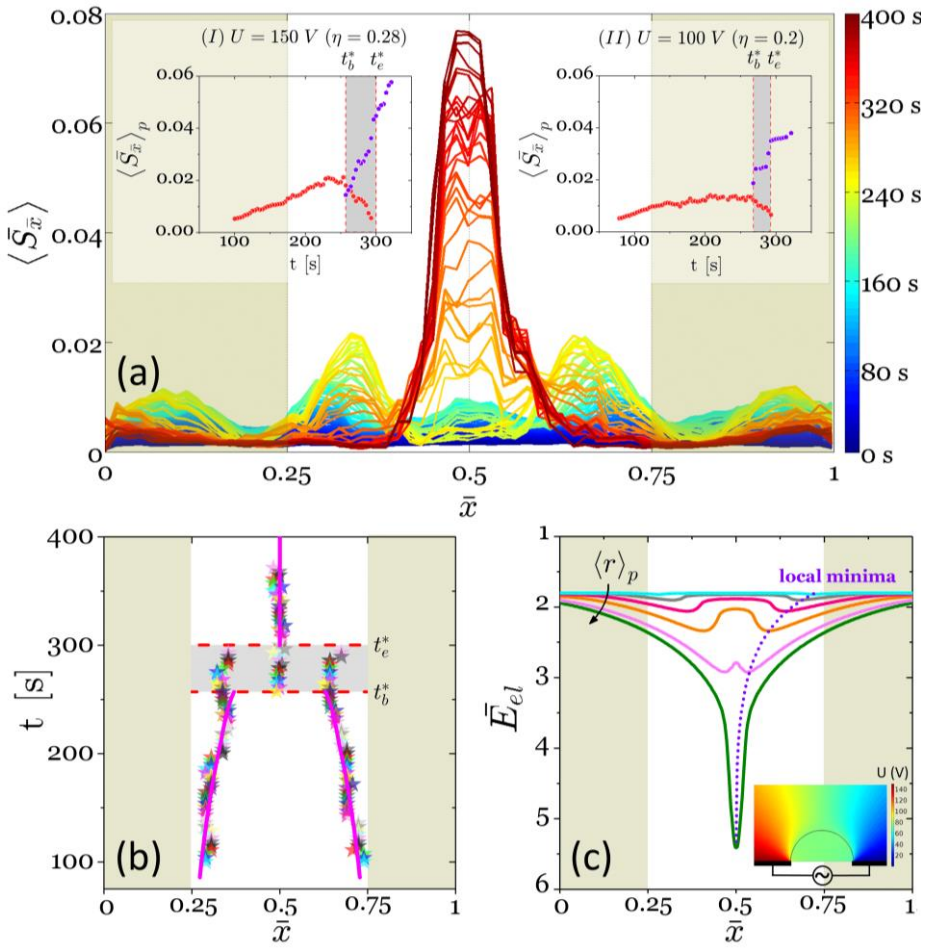

Fig. 6: (a) Color-coded temporal evolution of the average area fraction distribution of drops $\langle \bar{S}_{\bar{x}} \rangle$ along the nondimensionalized lateral coordinate ($\bar{x} = x/l$), over one pitch of the electrode pattern under EW ($U_{rms} = 150\,V$). The temporal variations of the peak values $\langle \bar{S}_{\bar{x}} \rangle_p$ in $\langle \bar{S}_{\bar{x}} \rangle$ for different voltages are shown in insets: (I) $U_{rms} = 150\,V$, (II) $U_{rms} = 100\,V$. The temporal variations of the peak locations in $\langle \bar{S}_{\bar{x}} \rangle$ are shown by star markers in (b). The transition period is shown by the gray area in the insets in (a) and in (b). (c) The nondimensionalized electrostatic energy $\bar{E}_{el}$ landscapes corresponding to representative values of the area-weighted average radius ($\langle r \rangle_p = 20;\ 40;\ 60;\ 80;\ 100;\ 110\ \mu m$) of the drops constituting the peak(s) in $\langle \bar{S}_{\bar{x}} \rangle$ before (with two minima) and after (with a single minimum) transition. The evolution in the electrostatic energy minima locations with increasing $\langle r \rangle_p$ is shown by the solid black line in (b). The inset shows the electric potential φ distribution for a condensate droplet under EW (schematic in Fig. 3(a)).

This single peak in $\langle \bar{S}_{\bar{x}} \rangle$ reflects the alignment of the bigger condensate drops at the gap center (Fig. 3(b), EW(iii)). Beyond t_e^*, these drops grow (Fig. 6(a) and inset (I)) while remaining aligned along the gap center (Fig. 6(b)). A similar breath figure evolution is observed for other values of the applied voltage, as shown by the $\langle \bar{S}_{\bar{x}} \rangle_p$ evolution at Urms = 100 V (inset (II) in Fig. 6(a)).

To understand the evolution of $\langle \bar{S}_{\bar{x}} \rangle$ under EW, we calculate the electrostatic energy E_{el} profile over the unit cell for a representative condensate droplet of variable size (schematic in Fig. 3(a)). For a droplet having radius $r = \langle r \rangle_p$, the electric potential φ corresponding to an x position is calculated by solving $\nabla \cdot [(\epsilon_0 \epsilon - i(\sigma/\omega))\nabla\varphi] = 0$ using a finite element method (inset in Fig. 6(c)). Here, ϵ_0 is the vacuum permittivity, ϵ is the material dielectric constant, σ is the material electrical conductivity, and ω is the circular frequency. For the present experimental conditions, the contribution of polarization current is significantly small compared to the conductive contribution. Hence, the system operates in the regime of ac-EW rather than "dielectrowetting" [21] (see SI in [20] for numerical computation details). Thereafter, the total electrostatic energy of the system is calculated as $E_{el} = -\int_v \frac{1}{2} \vec{E} \cdot \epsilon_0 \epsilon \vec{E} dv$, where $\vec{E} = -\nabla\varphi$ is the electric field, and v is the computation domain volume. Subsequently, the $E_{el}(x)$ landscape (nondimensionalized as $\bar{E}_{el} = |E_{el}|/4\pi\langle r \rangle_p^2 \gamma$; where γ is the water-air surface tension) is evaluated as a function of the drop position along the unit cell.

Before the onset of coalescence cascade, i.e., for $\langle r \rangle_p \leq \langle r \rangle_p^*$, $\bar{E}_{el}$ is symmetric about the gap center with minima (electrostatic potential wells) on either side of it (Fig. 6(c)). The locations of these two potential wells gradually shift towards the gap center with increasing $\langle r \rangle_p$ (dotted line in Fig. 6(c)). The temporal evolution of the peak locations in $\langle \bar{S}_{\bar{x}} \rangle$ (symbols) closely follows the electrostatic energy minima locations (solid black line) corresponding to increasing $\langle r \rangle_p$ (Fig. 6(b)). The drops

formed due to coalescence under EW thus migrate to the electrostatic energy minima corresponding to their sizes, culminating in the alignment of the drops on either side of the gap center. As $\langle r \rangle_p$ exceeds $\langle r \rangle_p^* \sim 0.3 w_g$, droplets under the side peaks with $r > \langle r \rangle_p^*$ migrate towards the corresponding electrostatic energy minima even closer to the gap center. Motion of these droplets initiates collisions between droplets on both sides of the gap center triggering the coalescence cascades (see appendix 3A) The resulting drops with diameters comparable to w_g ($r \gtrsim 0.6wg$), along with the adjacent electrodes, form two parallel plate capacitors in series, with the dielectric layer as spacers [22]. In this case, $\bar{E}_{el}$ is symmetric with a single minimum at the gap center (Fig. 6(c)). Consequently, these approximately monodisperse drops migrate to, and remain aligned along, the gap center (Fig. 6(b)). Such alignment results in a definite periodicity of the droplet pattern along the x direction, which is determined by the electrode pitch [Fig. 3(b), EW(iii)].

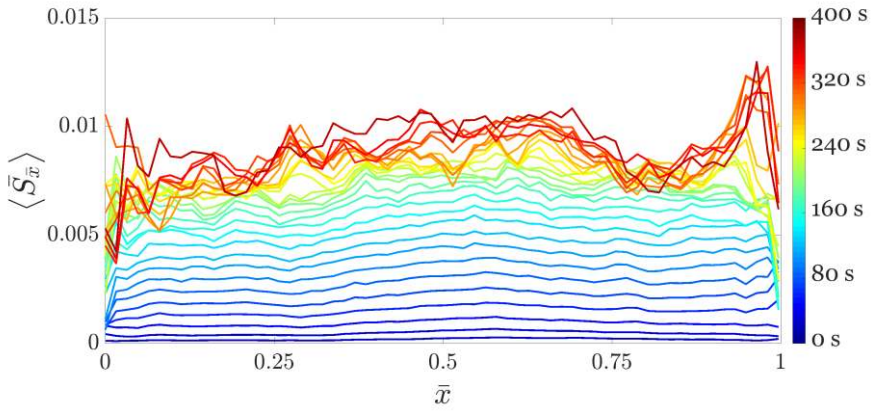

Fig. 7: Color-coded temporal evolution of the average area fraction distribution of drops $\langle \bar{S}_{\bar{x}} \rangle$ along the non-dimensionalized lateral co-ordinate ($\bar{x} = x/l$), over a distance equivalent to one pitch (l) of the electrode pattern, without EW. At any time instant, the $\langle \bar{S}_{\bar{x}} \rangle$ distribution along $\bar{x}$ remains almost uniform without the influence of EW, as can be expected for the randomly distributed drops on the control surface.

2.5. Conclusions

In summary, we have shown that the electrostatic energy landscape under ac-EW induces migration and coalescence of condensate droplets, leading to unique breath figure characteristics. The coalescing drops align at the corresponding electrostatic energy minima, instead of staying restricted to the center of mass of the parent drops as in classical breath figures. The resulting periodicity of the droplet pattern under EW can be further controlled by simply tuning the electrode geometry. We hope that this study will trigger a general theoretical analysis of drop condensation patterns in arbitrary energy landscapes.

Appendix 2A: Initiation of coalescence cascades by droplets greater than a critical size ($\langle r \rangle_p^*$)

Fig. 8 shows the evolution of the equilibrium location ($\bar{x}_{eq}$) of a representative condensate drop (having radius $r \sim \langle r \rangle_p$) with the enhancement in its size (i.e. with increasing value of $\langle r \rangle_p$) under EW. It shows such an evolution of a representative droplet over one half of the gap (width w_g). It must be remembered here that a condensate droplet in the breath figure under EW aligns itself along the location of the electrostatic energy minimum corresponding to its size (as already explained

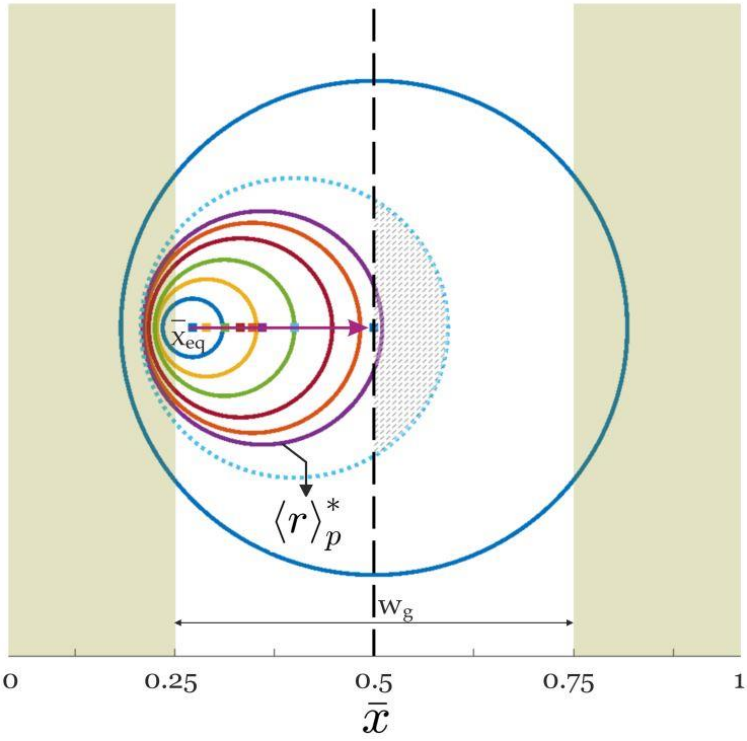

Fig. 8: Gradual evolution of the equilibrium location ($\bar{x}_{eq}$) of a representative condensate drop having radius $\sim \langle r \rangle_p$ under EW, with the enhancement in its size (as represented by increasing $\langle r \rangle_p$). $\bar{x}_{eq}$ is evaluated numerically by determining the location of the minimum from the electrostatic energy landscape across a unit cell corresponding to a sessile droplet having radius $\sim \langle r \rangle_p$.

with the help of Fig. 6). $\bar{x}_{eq}$ gradually shifts towards the gap-center with increasing $\langle r \rangle_p$ (see Fig. 8), as the location of the electrostatic energy minimum gradually shifts towards the gap-center. For $r \sim \langle r \rangle_p^* \sim 0.3 w_g$, the corresponding equilibrium location of the drop is such that the extent of the drop just exceeds the gap-center (see the droplet footprint, as marked by the solid purple circle, corresponding to $\langle r \rangle_p^*$ in Fig. 8).

For a drop having radius greater than $\langle r \rangle_p^*$, the corresponding equilibrium location under EW shifts further closer to the gap-center. Consequently, the corresponding extent/footprint of the droplet covers increasingly more substrate area on the other half of the gap (see the shaded area of the footprint of the droplet having radius greater than $\langle r \rangle_p^*$, as marked by the dotted cyan circle in Fig. 8). The migration of the droplet towards such an equilibrium location increases the chance of collision with droplets on the other side of the gap-center. It must be remembered here that there are simultaneous, similar growths of droplets over the other half of the gap (not shown in Fig. 8) which greatly aid such collisions between droplets from both sides of the gap-center. The larger droplet created due to such a coalescence event in turn migrates to the location of the corresponding electrostatic energy minimum which is even closer to the gap-center, and interacts with other droplets. This is how a cascade of coalescence events is triggered by droplets having radius greater than $\langle r \rangle_p^*$. At the end of the coalescence cascade, a large droplet having radius comparable to w_g is created which aligns along the location of the corresponding electrostatic energy minimum at the gap-center (see the droplet footprint marked by the solid blue circle in Fig. 8; also see Fig. 4). Moreover, since the coalescence cascades mostly involve the moderately larger droplets from both sides of the gap-center, there are no larger droplets left in the immediate vicinity of the final droplets created at the end of the coalescence cascades (see Fig. 4).

Appendix 2B: Imaging and image analysis methodologies

Time-lapse images of dropwise condensation are captured by a 4K digital camera (Point Grey, FL3-U3) fitted with a zoom lens system (Z125D-CH12, EHD). In order to achieve high quality and contrast in the images, proper backlight illumination is used (MB-BL305-RGB-24-Z, Metabright) (Fig. 1). Imaging with transmission light though the transparent condensing surface (containing transparent ITO electrode pattern) shows the projection of the droplets on the surface. In this setting, the projection of the outer contour of each droplet on the substrate is visualized; therefore, the spherical radius (r) of each droplet can be extracted from the images, and is used for further analysis (Fig. 9). The condensate droplet morphology on the hydrophobic surface is close to a hemisphere due to the Young's contact angle of $\theta_y \sim 110°$ (no EW), and Lippmann contact angle $\theta(U_{rms})$ very close to 90° under EW. As such, the contact radius of the droplet r_c is proportional to r as $r_c = r \sin\theta$ (Fig. 9). Hence, for both the cases r_c is very close to $r - r_c \cong r$ under EW, and $r_c \approx 0.94r$ without EW. Accordingly, for the analysis of

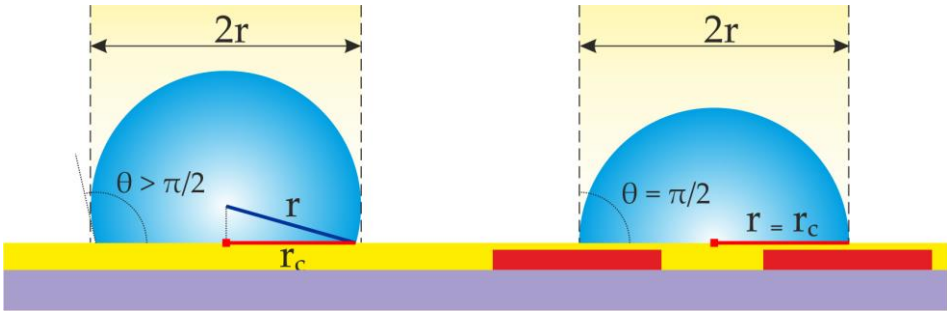

Fig. 9: Left: Schematic of a droplet on the hydrophobic surface with a Young's contact angle θ_y larger than $\pi/2$ ($\theta_y \sim 110°$). In this limit, the actual contact area of such a droplet can be fairly estimated by its projection area on the substrate. Right: Schematic of a droplet under EW. The apparent contact angle $\theta(U_{rms})$ is very close to 90° under EW, which results in a contact radius (r_c) almost equal to the spherical radius (r), appearing in the images. The schematics are not to scale.

droplet contact area both with and without EW we use the accessible spherical radius (r) as a fair approximation of the contact radius (r_c).

The images are analyzed using an in-house Matlab script to detect all the droplets in the breath figure. In the first step, the raw image at each time instant is converted to a grey scale image. The background image, which is recorded prior to the condensation experiments without any droplet on the surface, is subtracted from the grey scale image to avoid any possible surface defect; otherwise, the surface defect can be detected as a droplet. In the next step, the subtracted image is turned into a binary image by carefully selecting the proper threshold. To this end, we consider the histogram of the intensity, and use the peak value as the conversion threshold. Then we carefully treat the two types of holes which exist in the binary image. First, the holes which appear at the center of droplets due to the transmission of light though the droplet. These holes have a circular shape (the same shape as the light source). We carefully filter these holes based on their eccentricity, and fill these. Second, we consider the other type of holes which are formed in the binary image from connection of the boundaries of neighboring droplets. This imaging artefact happens mostly for a group of small droplets around a larger one, during the creation of the binary image. To separate these droplets from each other and detect these individually, we use watershed transform. Finally, each component is considered as an individual droplet, and is fitted to a circle. Subsequently, the radius as well as the spatial coordinates of the center of every single droplet in the image are defined. Eventually, the arrays of sizes and positions of all the droplets at each time instant, extracted following the aforementioned methodology, are used for the subsequent statistical analysis.

References

[1] D. Beysens, "The formation of dew," *Atmos. Res.*, vol. 39, no. 1–3, pp. 215–237, 1995.

[2] F. T. Malik, R. M. Clement, D. T. Gethin, W. Krawszik, and A. R. Parker, "Nature's moisture harvesters: a comparative review," *Bioinspir. Biomim.*, vol. 9, no. 3, p. 31002, Sep. 2014.

[3] D. Milani, A. Abbas, A. Vassallo, M. Chiesa, and D. Al Bakri, "Evaluation of using thermoelectric coolers in a dehumidification system to generate freshwater from ambient air," *Chem. Eng. Sci.*, vol. 66, no. 12, pp. 2491–2501, 2011.

[4] M.-H. Kim and C. W. Bullard, "Air-side performance of brazed aluminum heat exchangers under dehumidifying conditions," *Int. J. Refrig.*, vol. 25, no. 7, pp. 924–934, 2002.

[5] A. D. Khawaji, I. K. Kutubkhanah, and J.-M. Wie, "Advances in seawater desalination technologies," *Desalination*, vol. 221, no. 1–3, pp. 47–69, 2008.

[6] D. Beysens, "Dew nucleation and growth," *Comptes Rendus Phys.*, vol. 7, no. 9–10, pp. 1082–1100, 2006.

[7] J. W. Rose, "On the Mechanism of Dropwise Condensation," *Int. J. Heat Mass Transf.*, vol. 10, p. 755, 1967.

[8] D. Beysens and C. M. Knobler, "Growth of Breath Figures," *Phys. Rev. Lett.*, vol. 57, no. 12, pp. 1433–1436, 1986.

[9] J. L. Viovy, D. Beysens, and C. M. Knobler, "Scaling description for the growth of condensation patterns on surfaces," *Phys. Rev. A*, vol. 37, no. 12, pp. 4965–4970, 1988.

[10] D. Fritter, C. M. Knobler, and D. A. Beysens, "Experiments and simulation of the growth of droplets on a surface (breath figures)," *Phys. Rev. A*, vol. 43, no. 6, pp. 2858–2869, 1991.

[11] J. B. Boreyko and C. H. Chen, "Self-propelled dropwise condensate on superhydrophobic surfaces," *Phys. Rev. Lett.*, vol. 103, no. 18, pp. 2–5, 2009.

[12] N. Miljkovic, R. Enright, and E. N. Wang, "Effect of Droplet Morphology on Growth Dynamics and Heat Transfer during Condensation on Superhydrophobic Nanostructured Surfaces," *ACS Nano*, vol. 6, no. 2, pp. 1776–1785, Feb. 2012.

[13] N. Miljkovic *et al.*, "Jumping-Droplet-Enhanced Condensation on Scalable Superhydrophobic Nanostructured Surfaces," *Nano Lett.*, vol. 13, p. 179, 2013.

[14] N. Miljkovic, D. J. Preston, R. Enright, and E. N. Wang, "Electric-field-enhanced condensation on superhydrophobic nanostructured surfaces," *ACS Nano*, vol. 7, no. 12, pp. 11043–11054, 2013.

[15] R. D. Narhe and D. A. Beysens, "Nucleation and Growth on a Superhydrophobic Grooved Surface," *Phys. Rev. Lett.*, vol. 93, pp. 76101–76103, 2004.

[16] A. Ghosh, S. Beaini, B. J. Zhang, R. Ganguly, and C. M. Megaridis, "Enhancing dropwise condensation through bioinspired wettability patterning," *Langmuir*, vol. 30, no. 43, pp. 13103–13115, 2014.

[17] S. Anand, A. T. Paxson, R. Dhiman, J. D. Smith, and K. K. Varanasi, "Enhanced Condensation on Lubricant- Impregnated Nanotextured Surfaces," *ACS Nano*, vol. 6, no. 11, pp. 10122–10129, 2012.

[18] H. Tsuchiya *et al.*, "Liquid-Infused Smooth Surface for Improved Condensation Heat Transfer," *Langmuir*, vol. 33, no. 36, pp. 8950–8960, Sep. 2017.

[19] F. Mugele and J.-C. Baret, "Electrowetting: from basics to applications," *J. Phys. Condens. Matter*, vol. 17, no. 28, pp. R705–R774, 2005.

[20] D. Baratian, R. Dey, H. Hoek, D. Van Den Ende, and F. Mugele, "Breath Figures under Electrowetting : Electrically Controlled Evolution of Drop Condensation Patterns," *Phys. Rev. Lett.*, vol. 120, no. 21, p. 214502, 2018.

[21] G. McHale, C. V. Brown, M. I. Newton, G. G. Wells, and N. Sampara, "Dielectrowetting driven spreading of droplets," *Phys. Rev. Lett.*, vol. 107, no. 18, pp. 1–4, 2011.

[22] D. 't Mannetje *et al.*, "Trapping of drops by wetting defects.," *Nat. Commun.*, vol. 5, p. 3559, 2014.

3

Collective characteristics of breath figures under electrowetting: Self-similarity and size distribution

In the previous chapter, we showed how electrowetting alters the distribution of condensate drops by aligning the drops and by enhancing coalescence. Such EW-controlled migration and coalescence of condensate drops significantly alter the statistical characteristics of the ensemble of droplets. The evolution of the drop size distribution displays self-similar characteristics that significantly deviate from classical breath figures on homogeneous surfaces once the electrically induced coalescence cascades set in beyond a certain critical drop size. The resulting reduced surface coverage, coupled with earlier drop shedding under EW, suggest enhancement in the condensation performance which is the subject of next chapter.

This chapter has been adapted from the publication:
D. Baratian, R. Dey, H. Hoek, D. Van Den Ende, and F. Mugele, "Breath Figures under Electrowetting : Electrically Controlled Evolution of Drop Condensation Patterns," *Phys. Rev. Lett.*, vol. 120, no. 21, p. 214502, 2018.

3.1. Introduction

An intriguing feature of breath figures is that the pattern evolution of condensate droplets is self-similar in time, as established by scaling the droplet size distribution [1]–[5]. To improve the efficiency of the dropwise condensation process, it is essential to control the underlying breath figure characteristics. Here, we use an alternating (ac) electric field in an electrowetting (EW) configuration with patterned electrodes [6] to actively control the breath figure evolution on otherwise homogeneous hydrophobic surfaces. We demonstrate that EW significantly modifies the distribution of condensate drops using electrical forces and alters the statistical characteristics of the entire ensemble of droplets from those established for classical breath figures with randomly distributed drops. As described in the previous chapter, the breath figure evolution under EW is characterized by size-dependent alignment of the condensate drops at the minima in the corresponding electrostatic energy landscapes and enhanced coalescence. A scaling analysis shows that the size distribution of drops is self-similar in time with different characteristics in the initial and final growth phases. The unique transformation in the scaling plot is triggered by EW-induced coalescence cascades beyond a critical drop size. Such EW-mediated alignment and enhanced coalescence increases the average droplet radius, but reduces the surface coverage.

3.2. Results

As the electrostatic energy landscape under ac-EW induces drop alignment at the corresponding size-dependent energy minima (shown in previous chapter), it results in migration and coalescence of condensate droplets. Consequently, such a phenomenon leads to unique breath figure characteristics under EW.

3.2.1. Average size

One of the collective features of the breath figures which undergoes significant change under EW (with regards to the classical condensation without the effects of any electrostatic forces) is the average statistical size of the ensemble of

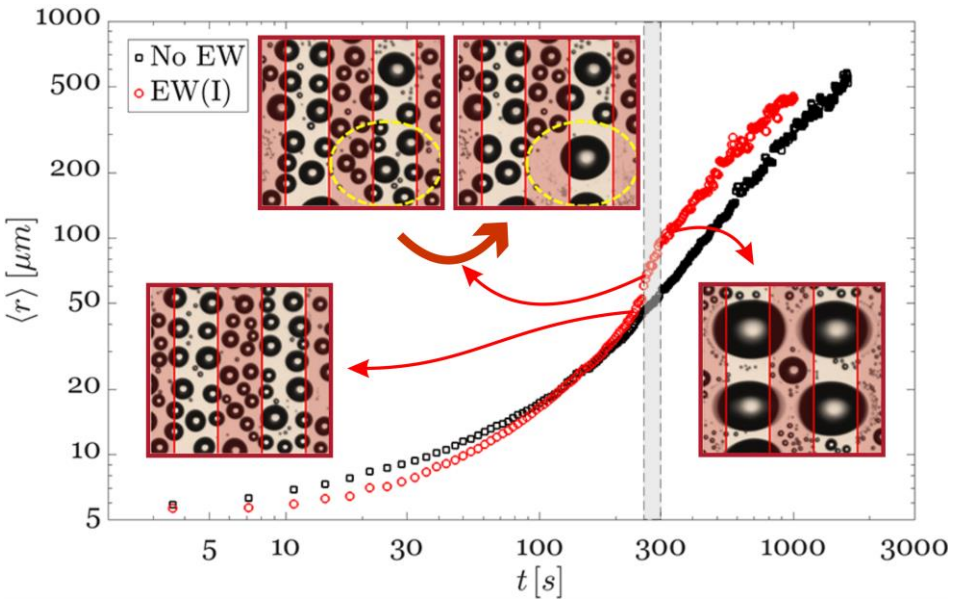

Fig. 1: Evolutions of the area-weighted mean radius $\langle r \rangle$ of the breath figure droplets without EW (control) and under EW (U_{rms} = 150 V) until the first shedding. The droplet patterns corresponding to different growth regimes of $\langle r \rangle$ under EW are shown as insets.

condensate droplets. EW-induced coalescence cascades result in a sharp increase of the area-weighted average radius of the droplets which is defined as:

$$\langle r \rangle = \frac{\sum r^3}{\sum r^2}$$

Fig. 1 shows the evolutions of the area-weighted mean radius ⟨r⟩ of the breath figure droplets without EW (control) and under EW (U_{rms} = 150 V) until the first shedding (black and red markers respectively). The larger droplets created due to the coalescence cascades, increase $\langle r \rangle$ compared to that for the control surface (Fig. 1). The droplet patterns corresponding to different growth regimes of ⟨r⟩ under EW are shown as insets.

Eventually, the gravity-driven drop shedding under ac-EW sets in at a smaller drop size as compared to the control surface (Fig. 1), due to the reduction of effective contact angle hysteresis under ac-EW [7] and the consequential enhancement of gravity-driven drop mobilization [8].

3.2.2. Self-similarity

The EW-mediated evolution of the droplet size distribution is also significantly different from that established for classical breath figures. The droplet size ($s \sim r^3$) distribution under EW is bimodal, exhibiting a power-law decay for smaller droplets and a bell-shaped distribution for larger droplets (Fig. 2 (a)). Here, $n_s(s,t)$ represents the number of droplets of volume s per unit droplet volume and surface area. As depicted in Fig. 2(b) and Fig. 3(b), the temporal variation of n_s is selfsimilar, obeying the scaling relation [1]–[3], [9]:

$$n_s(t) = s^{-\theta} \cdot f\left(\frac{s}{S}\right) \qquad \text{Eq. (1)}$$

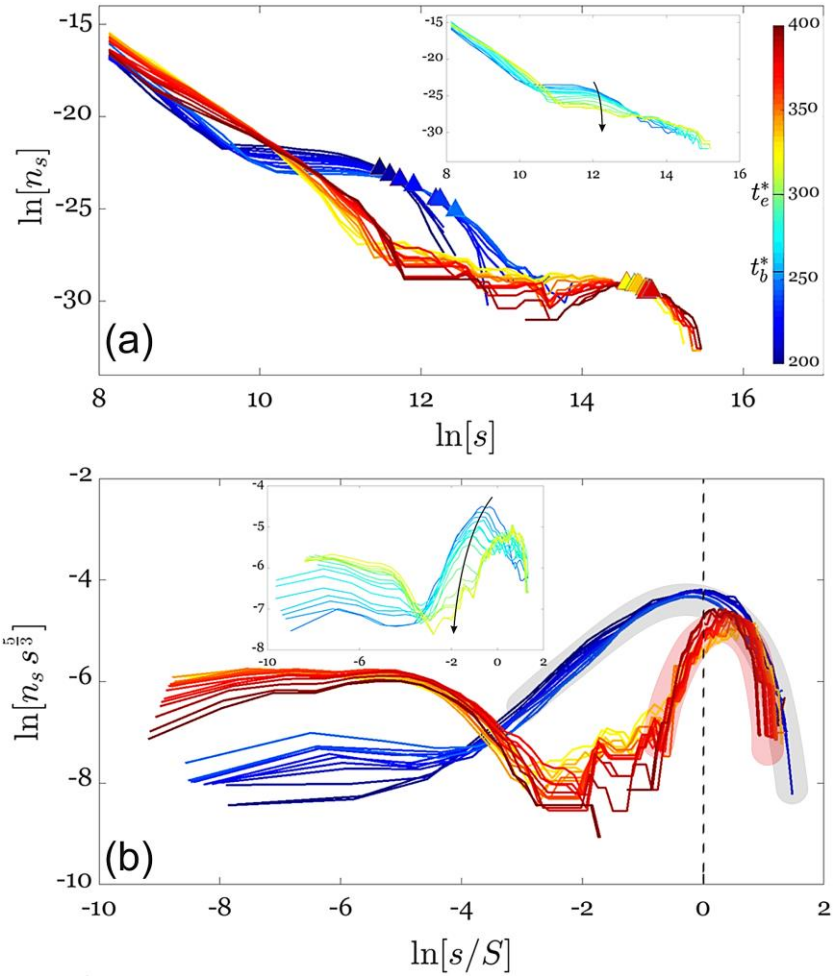

Fig. 2: (a) Self-similar evolution of the droplet size (s) distribution (n_s) in the breath figure under EW (U_{rms} = 150 V) before and after the transition period. The time evolution is color coded with times before and after transition, colored in shades of blue and red, respectively. The triangular markers show the ns estimates for average drop sizes constituting the peaks in $\langle \bar{S}_{\bar{x}} \rangle$ [Fig. 9(a)]. (b) Corresponding scaling plots of ns obtained using Eq. (1) before and after the transition. The ns evolution within the transition period, and the corresponding scaling plots, are shown in the insets in (a) and (b), respectively.

Here, $S(t) \sim \langle r \rangle^3$, and the exponent $\Theta = 1 + d/D$ depends on the dimensionality of the drops ($D = 3$) and the condensing surface ($d = 2$). For $t < t_b^*$, the coalescence-dominated evolution of the bellshaped distributions for the larger drops is collapsed by the similarity transformation (Eq. (1)) on considering $\Theta = 5/3$ (gray shaded region of the scaling plots for $t < t_b^*$ in Fig. 2(b)). It must be noted that the smaller drops ($ln[s/S] < -4$) follow a different scaling that is dependent on the nucleation and the small-scale growth mechanisms [5], [9]. However, for characterizing the breath figures under EW (Fig. 6(a) in chapter 2), it is sufficient to describe the evolution of the bell-shaped part of the droplet size distribution, since the corresponding droplets align within the gaps. This is substantiated by the fact that the n_s estimates corresponding to $s_p \sim \left(\langle r \rangle_p\right)^3$ are close to the peak of the bell-shaped distribution (triangular markers in Fig. 2(a)).

Naturally, the evolution of $n_s(s,t)$ under EW loses its self-similarity in the transition period due to the EW-induced coalescence cascades (inset in Fig. 2(b)), unlike the droplet size distribution for the control surface, which remains self-similar throughout the coalescence dominated growth regime (Fig. 3). However, for $t \geq t_b^*$, the evolution of n_s for the larger droplets again exhibits self-similarity, albeit with a significantly different functional form compared to that for $t < t_b^*$ (Fig. 2(b)) and for the control surface (Fig. 3).

The almost uniform sizes of the large droplets created due to the coalescence cascades manifest in the narrower bell-shaped distribution for $t \geq t_e^*$ (compare the blue versus red scaling plots in Fig. 2(b)). Furthermore, due to the large separation of sizes between the dominant monodisperse droplets and the small background droplets (Fig. 3(b), EW(iii) in chapter 2), the corresponding bell-shaped distributions are no longer peaked at S, contrary to that for $t < t_b^*$ and for the control surface (Fig. 2(b); Fig. 3). Interestingly, the alignment of the growing monodisperse drops at the

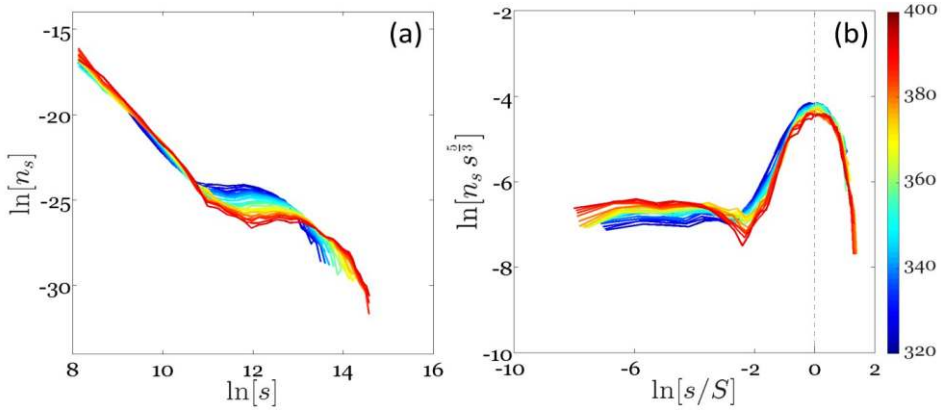

Fig. 3: (a) Self-similarity in the evolution of the droplet size distribution (n_s) for the breath figures without EW (i.e. droplets growing on the control surface) during the coalescence-dominated growth regime. Here, the evolution over time is color coded. (b) Scaling plots of n_s obtained using Eq. 1. The evolution of the bell-shaped distribution of the larger droplets remains self-similar throughout the coalescence-dominated growth regime when there is no EW impacts. Moreover, the size distribution of the larger droplets exhibits self-similarity with the same functional form (collapsed on the master curve) throughout the coalescence dominated growth regime without EW.

electrostatic energy minima, which always remains at the gap center, makes the corresponding size distribution analogous to that for condensation on a line ($d = 1$) [12]. Such evolution of the droplet size distribution is unique to the EW-induced anisotropy in the system.

3.2.3. Surface coverage

The significant reduction in n_s for the relatively larger droplets, due to the coalescence cascades (Fig. 2(b)), results in enhanced "release" of substrate surface area. Consequently, between the EW-mediated condensation and the control case, there is considerable difference in surface coverage (Fig. 4). In DWC, surface coverage (Γ) is defined as the ratio of total drop contact area to the condensing surface area. From the images, we calculate:

$$\Gamma = \sum \pi r^2 / A_{FOV}$$

where A_{FOV} is the area of the field of view.

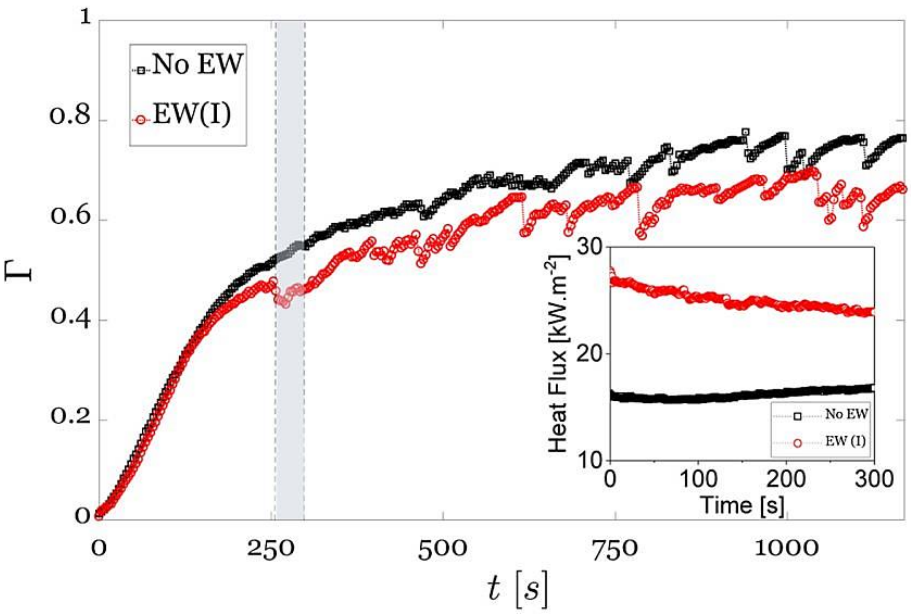

Fig. 4: Evolutions of the breath figure surface coverage (Γ) without EW (control in black markers) and under EW (U_{rms} = 150 V in red markers). Inset shows the enhanced heat flux under EW. Heat transfer data are collected in a separate set of experiments; see chapter 4 for the details.

During classical condensation, Γ initially rises monotonically with increasing the size of droplets, and then fluctuates due to simultaneous growth and coalescence of large droplets with each other (after coalescence, a merged droplet has less contact area compared to the sum of contact areas of each initial droplet). Γ also decreases when a droplet sheds down and sweeps the surface (collects other droplets) in its path. Eventually, the surface coverage saturates at the level of ~0.75 in this dataset (see black markers in Fig. 4).

The temporal evolution of Γ for condensation under EW starts with a monotonic increase due to growth of small droplets (similar to the one for the control surface). With the onset of transition period, the EW-induced coalescence cascades lead to significant reduction of Γ (see the transition – gray – time window in Fig. 4), and later reaches a saturation level of ~0.6 in the steady state condition.

We observe ~10%–12% reduction in the steady state surface coverage under EW, with respect to the control surface (Fig. 4). The reduced Γ coupled with the enhanced gravity driven shedding of condensate drops, due to the AC-EW induced increased droplet growth and reduced hysteresis. This reduced surface coverage plays a role in enhanced heat transfer that we have measured later (inset in Fig. 4).

The heat transfer measurements in this specific EW actuation scenario, show a striking 50%–60% increase in net heat flux for dropwise condensation under EW (inset in Fig. 4). It must be noted that thinner inorganic dielectric layers (e.g., SiO_2 or Al_2O_3) are available for EW [10], [11] to significantly minimize the thermal resistance compared to the presently used polymer layers. The extensive study of EW effects on heat transfer of dropwise condensation will be followed in the next chapter.

3.3. Conclusions

We have shown that EW induces migration and coalescence of condensate droplets. This leads to unique breath figure characteristics. EW alters the size-distribution of droplet ensemble. While the breath figure patterns under EW manifests universal self-similarity before the transition period (similar to the classical condensation), the pattern of drop ensemble after the transition (i.e. after EW-induced migration and coalescence of condensate droplets) shows significantly different functional form in comparison. The average radius of droplets also undergoes a rapid increase due to coalescence cascades. We have shown that the modification of the breath figure characteristics under EW leads to lower surface coverage which is of great interest for boosting the phase transition rate, and therefore suggests more heat transfer rates would be feasible for thermal applications. The extensive study on heat transfer under EW is discussed in details in chapter 4. We anticipate that these effects will be useful for optimizing applications involving dropwise condensation, like heat exchangers and breath figure templated self-assembly [12].

References

[1] F. Family and P. Meakin, "Scaling of the droplet-size distribution in vapor-deposited thin films," *Phys. Rev. Lett.*, vol. 61, no. 4, p. 428—431, Jul. 1988.

[2] F. Family and P. Meakin, "Scaling of the droplet-size distribution in vapor-deposited thin films," *Phys. Rev. Lett.*, vol. 62, no. 14, p. 1699, 1989.

[3] P. Meakin, "Dropwise condensation: the deposition growth and coalescence of fluid droplets," *Phys. Scr.*, vol. T44, pp. 31–41, 1992.

[4] R. D. Narhe, M. D. Khandkar, K. P. Adhi, A. V. Limaye, S. R. Sainkar, and S. B. Ogale, "Difference in the dynamic scaling behavior of droplet size distribution for coalescence under pulsed and continuous vapor delivery," *Phys. Rev. Lett.*, vol. 86, no. 8, pp. 1570–1573, 2001.

[5] J. Blaschke, T. Lapp, B. Hof, and J. Vollmer, "Breath figures: Nucleation, growth, coalescence, and the size distribution of droplets," *Phys. Rev. Lett.*, vol. 109, no. 6, pp. 3–6, 2012.

[6] F. Mugele and J.-C. Baret, "Electrowetting: from basics to applications," *J. Phys. Condens. Matter*, vol. 17, no. 28, pp. R705–R774, 2005.

[7] F. Li and F. Mugele, "How to make sticky surfaces slippery: Contact angle hysteresis in electrowetting with alternating voltage," *Appl. Phys. Lett.*, vol. 92, no. 24, pp. 1–4, 2008.

[8] T. D. J. C. M. Mannetje, C. U. Murade, D. Van Den Ende, and F. Mugele, "Electrically assisted drop sliding on inclined planes," *Appl. Phys. Lett.*, vol. 98, no. 1, pp. 3–5, 2011.

[9] G. I. Barenblatt, G. I. Barenblatt, and B. G. Isaakovich, *Scaling, self-similarity, and intermediate asymptotics: dimensional analysis and intermediate asymptotics*, vol. 14. Cambridge University Press, 1996.

[10] S. Berry, J. Kedzierski, and B. Abedian, "Low voltage electrowetting using thin fluoroploymer films," *J. Colloid Interface Sci.*, vol. 303, no. 2, p. 517—524, Nov. 2006.

[11] H. Yang, S. Hong, B. Koo, D. Lee, and Y.-B. Kim, "High-performance reverse electrowetting energy harvesting using atomic-layer-deposited dielectric film," *Nano energy*, vol. 31, pp. 450–455, 2017.

[12] Z. Lin, *Evaporative self-assembly of ordered complex structures*. World Scientific, 2012.

4

EW-enhanced heat transfer of dropwise condensation on functionalized surfaces

Dropwise condensation under alternating electrowetting (AC-EW) manifests significant changes in thermal characteristics and shedding dynamics compared to the classical condensation. We show the first direct heat transfer measurements for condensation of water droplets on functionalized surfaces with embedded electrodes, while applying alternating electric fields. In absence of Non-Condensable Gases (NCG's) such as air, we measure enhanced heat transfer up to 74% with respect to the control case. The measured heat flows show dependency to applied voltage level as well as to the AC frequency. Besides the heat flow measurements, we analyze the behavior of condensate droplets on the surface visually from recorded images, showing how the droplets grow, merge, and eventually shed down under gravity. We demonstrate also the shedding dynamics of condensate droplets depend on the magnitude of applied EW voltage as well as the AC frequency. We report that the shedding of condensate droplets not only starts earlier at smaller average drop sizes compared to the classical dropwise condensation, but also takes place more frequently due to EW-mediated suppression of resistive pinning forces. Considering the average shedding size and frequency under different EW scenarios, we calculate the accumulated condensation rate as an indication of released latent heat of condensation, which turns out to be in good correlation

with the heat transfer measurements. Indeed, by EW-boosted shedding, the surface is swept more frequent by shedding droplets, which leads to more bare surface becoming available for enhanced re-nucleation per unit time. Hence the higher heat flow measured under EW is consistent with the change in shedding characteristics of condensate droplets. Our results shed new light on active controlling of condensation process to increase the efficiency of heat transfer, compared to the present passive methods.

This chapter is under preparation for submission:
D. Baratian, K. Khalil, R. Dey, H. Hoek, K. Varanasi, and F. Mugele, "Electrowetting-enhanced heat transfer of dropwise condensation on functionalized surfaces using electrowetting", (2020)

4.1. Introduction

In recent years, we see usage of various technologies in large scale around the globe which rely on condensation of vapor into liquid. Heat exchangers in power plants [1], water harvesting systems [2], and desalination systems [3] are examples of such technologies. In heat transfer applications, dropwise condensation (DWC) is widely used to increase the heat transfer rates by proper surface treatment to turn the condensate in the form of droplets instead of liquid films. In DWC, continuous shedding events causes sweeping of the condensate droplets from the surface, therefore, over time, more bare surface is exposed to the vapor repeatedly for renewed nucleation which is followed by growth and shedding of successor embryo droplets. Hence the shedding dynamics of condensate droplets play an important role in efficiency of condensation and consequently the rate of heat transfer of vapor-to-liquid phase change [4]–[6]. Several studies have been devoted to enhance mobility and shedding of condensate drops through developing biomimetic surfaces [7] such as nanostructured superhydrophobic surfaces [8]–[14], wettability-

patterned surfaces [15], and liquid infused textured surfaces [16]–[18], Intrinsically all these approaches towards enhancing droplet mobility are passive, relying solely on the topographical and/or chemical patterning of the condensing surface. As an alternative, previously we have shown that by using alternating electric fields in an electrowetting configuration (AC-EW), we can actively control the mobility of condensate drops on a hydrophobic surface with embedded structured electrodes. Considering the evolution and statistics of the condensate droplet pattern, we demonstrated that the growth of the condensate drops under EW is characterized by their migration to the size-dependent locations of the minima in the corresponding electrostatic energy landscapes which is facilitated by EW-enhanced coalescence [19]. We also showed the increase in gravity-driven shedding of condensate drops under AC-EW [20]. Although the pattern evolution of condensate has been well studies, there are still open questions which remain unexplored. Considering EW effects on the pattern of droplets and their shedding characteristics, the intriguing question is: what would be the effect of EW on the condensation performance? How does the shedding rate change under EW? Is EW a lever to boost the condensation heat transfer? To answer these questions, we measured the heat flow of condensation under different EW scenario's and also monitored the shedding characteristics of condensate droplets.

In this chapter, we report the first direct heat flow measurements, showing the enhanced heat transfer of dropwise condensation under AC electrowetting, and in absence of non-condensable gases (NCG's) compared to classic scenarios. We show the effect of EW voltage as well as AC frequency on the condensation heat transfer. The dynamics of condensate droplets undergo significant changes under EW which are manifested in altered shedding radius and frequency of shedding. We believe this study facilitates the effective implementation of EW for technological applications involving dropwise condensation.

4.2. Experimental setup

The condensation experiments are conducted on microfabricated samples in a vacuum chamber. The sample consist of a 2-inch Silicon wafer (heat conductivity of 1.3 $Wcm^{-1}K^{-1}$) on which an insulation layer of ~100 nm is formed by thermal oxidation. This layer provides a background isolation layer which is resistance enough for patterning the electrodes and at the same time thin enough to pass the heat through the Silicon wafer. A pair of interdigitated electrodes is patterned out of Aluminum (see Fig.1(b)). The width and spacing between the electrodes are equal $w = g =$ 50 um. To isolate the electrodes from direct contact with the condensate, a conformal thin layer of Parylene-C (thickness $d = 2$ μm) is deposited by a chemical vapor polymerization process in order to create a dielectric layer on top of the electrodes which provides sufficient resistance against a short circuit between the electrodes through the conductive liquid on top. To make the surface hydrophobic, and to increase the mobility of condensate droplets by reducing the contact angle hysteresis on the substrates a thin layer of durable hydrophobic material is deposited on top of the surface. The details of this hydrophobic coating and the deposition process has been explained in [21]. An AC electric potential is applied between the two interdigitated electrodes using a function generator together with an amplifier (Trek PZD700A).

Fig.1 shows a schematic of the experimental setup (see the details of the experimental setup in [22]). The sample is mounted on one end facet of a cylindrical copper block using liquid metal (Ga) to avoid interface heat resistance and create a uniform bonding layer. The copper block is inserted into a vacuum chamber. The cylinder block has Teflon insulation around it to prevent heat loss, and allow for a 1-dimensional heat transfer assumption. The other end of the block is cooled with a

liquid spraying system which in turn sets the surface temperature of the sample at 15 ℃.

Three thermocouples which are inserted along the axis of the cylinder (see $T_{TC1}/T_{TC2}/T_{TC3}$ in the schematic of Fig.1.a) provide the readout temperature to

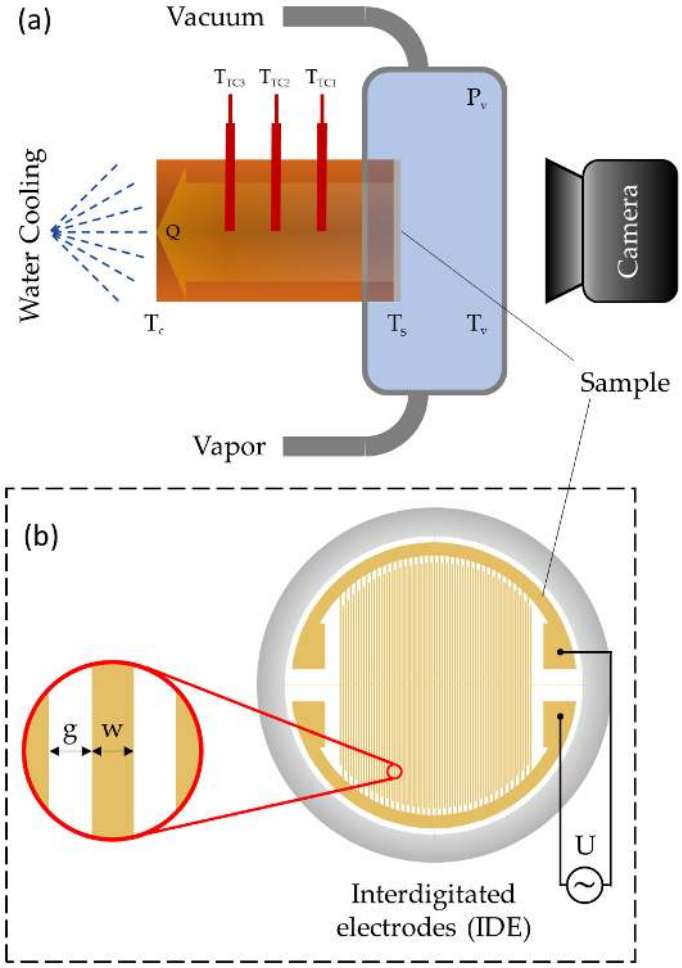

Fig.1: (a): schematic of the experimental setup (not to scale) (b): the pattern of Aluminum electrodes (interdigitated) over a SiO_2 layer thermally grown on a Silicon wafer. The electrode width and spacing is 50 um. The sample is then covered by a conformal layer of Parylene-C (2 um) and then a thin layer of hydrophobic coating is deposited on top.

calculate the temperature gradient at each time instant, and consequently the heat flow passing through the cylinder is calculated through a LabVIEW program with necessary input of thickness and thermal resistance of sample together with its coatings.

Upon applying vacuum, the non-condensable gases in the chamber are replaced with ultrapure saturated steam which is provided from a tube connected to a milli-Q water container (kept in a high temperature bath at $T = 373\ K$). The dew point approaches the saturation temperature of the vapor which scales with the saturation pressure in the chamber ($T_{dew} \sim P_r$). When the surface temperature (of 15 ℃), is below the dew point, condensation takes place, and upon further decreasing of the chamber pressure, condensation speeds up. At the point in which the chamber reaches to the set pressure of ~20 kPa (vapor at the saturation temperature of 60℃), the vacuum valve is closed to keep the chamber pressure constant. This moment stamps $t = 0$ in the plots. The condensation rate which remains more or less stable afterwards, is monitored and logged during the condensation process. When the water in the liquid reservoir is evaporated, the chamber inlet valve for vapor is closed and consequently the heat flow drops down rapidly (see the heat flow measurement in the insets of Fig.5).

The assembly of droplets on the surface is imaged with a digital camera (Nikon D5300) and a zoom lens. We use a Matlab script to analyze the videos and extract the size of the shedding droplets at each shedding events.

4.3. Results

Fig.2 shows the time-lapse images of condensate droplets on the surface under EW of 150V, showed for a time-window of 15 s. Each image captures an area of 13.5 mm × 7.6 mm on the surface. The strip electrodes can be recognized in light color ($w = 50\,\mu m$) on top of the dark background which indicates the gap area between the electrodes ($g = 50\,\mu m$). When the size of droplets is in the order of electrode/gap width, their migration under EW to the location with minimum electrostatic energy leads to their vertical alignment along the gap centers [19]. Such a forced migration results in enhanced coalescence of droplets under EW. The size and pattern of droplets changes over time as the condensation goes on. In a typical condensation process, the droplet growth and coalescence result in formation of larger droplets over time, however EW-induced coalescence of neighboring droplets forms larger droplets in shorter time. Eventually the droplet sheds down the surface by its body force. The very first question is: In which conditions the droplet undergoes shedding?

In essence, a droplet on a vertical surface starts to roll down under gravity when its size reaches to a certain critical value called as shedding radius (R_{sh}) at which the gravity forces exerting on the drop volume ($f_g \propto R^3$) overcome the resistive hysteresis forces acting on the contact lines ($f_{hys} \propto R$) [23].

$$f_g \sim f_{hys} \;\rightarrow\; \rho\left(\frac{2}{3}\pi R^3\right) g \sim (2R)\sigma\{Cos(\theta_r) - Cos(\theta_a)\} \;\rightarrow\; R_{sh} \approx \sqrt{\frac{3}{\pi}}\lambda_c \cdot (\Delta Cos\theta)^{1/2}$$

where ρ and σ are the density and surface tension of water respectively. $\lambda_c = \sqrt{\frac{\sigma}{\rho g}}$ is the capillary length. θ_r and θ_r are the advancing and receding contact angles of water on the condensing surface, therefore $\Delta Cos\theta$ gives a quantitative estimate of the

contact angle hysteresis (CAH) which originates from pinning forces due to heterogeneity of surface, pulling on the triple contact line. We have shown previously that that AC-EW effectively suppresses contact angles hysteresis [23]. The physics behind this CAH reduction is the continuous depinning of contact line from random surface heterogeneities induced by oscillatory electrostatic forces exerted on the contact line which is a result of oscillatory waves of liquid-vapor interface under alternating electric fields [24]–[26]. For sessile droplets in air ambient, CAH progressively decreases with increasing voltage, down to a saturation point beyond which CAH remain almost constant. Shedding takes place when the droplet is large enough for gravity to pull the drop down against the resistive pinning forces. EW-induced suppression of CAH results in enhanced mobilization of droplets, hence in case of dropwise condensation, the required body force is less, therefore the critical shedding radius, R_{sh} reduces under EW.

A number of shedding events can be observed in the image series of Fig.2. Within the indicated time window in this figure ($t = 93\,s$ till $t = 106\,s$) several shedding events take place. Each shedding droplet starts to slide downs as soon as it becomes large enough, and in its path merges (and collects) other smaller droplets, hence sweeps the surface. In our experiments, the size of each shedding droplet (highlighted with red contour in Fig.2) is extracted from the image and the number of shedding events is tracked over time.

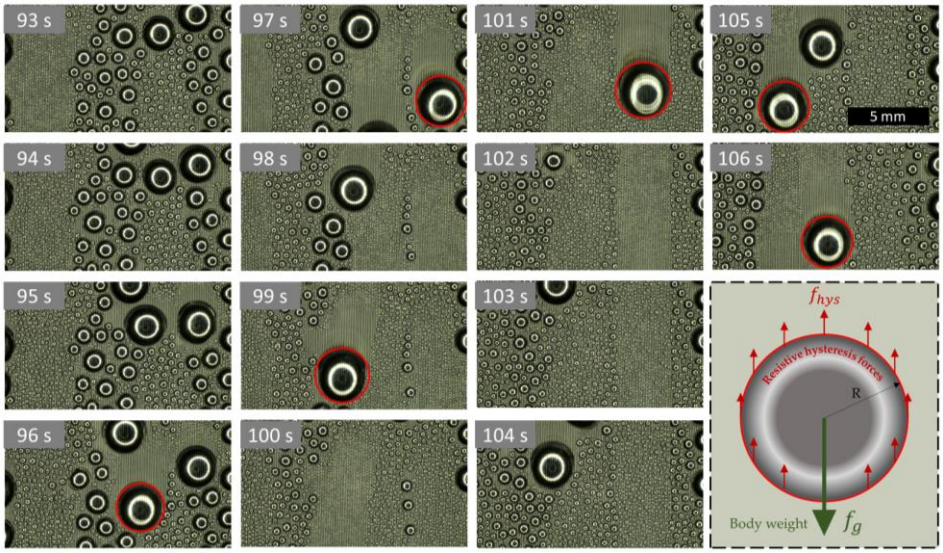

Fig.2: Time-lapse images of condensate droplets on the surface under AC-EW of 150V/50Hz during a time window of 13 s. The field of view indicates an area of 13.5 mm × 7.6 mm. Droplets grow by direct condensation on droplet surface as well as the EW-induced coalescence of neighboring droplets, up to a sufficiently large size in which they are pulled down by gravity. The shedding droplets are highlighted with red contour. The shedding radius and frequency are extracted from the image series. The schematic of a shedding droplet is depicted in the inset. It shows the competing gravity force against the resistive hysteresis forces to pull down the droplets on the vertical surface.

The shedding characteristics of condensate droplets, can be controlled with AC-EW. We have reported previously that for condensation in ambient pressure, the shedding properties including the critical drop size as well as number of shedding per unit time changes under EW, [20]. However, measuring the heat transfer of condensation remained a missing part of the puzzle. In this study, by conducting condensation experiments in absence of NCG's, we want to see whether the same physics are valid regarding EW effects on shedding dynamics in the first place. Then, it would be the matter of high interest to know the effect of EW on

thermal efficiency of condensation by directly measuring the heat transfer under different EW scenarios.

For our experiments in the pressure chamber, the NCG's are evacuated. Our results of monitoring the shedding properties show that EW significantly changes the dynamics of condensation process on the described functional surfaces, compared to the baseline (BL) scenario in which condensation takes place in the same conditions, however without electric fields. Fig.3 is a representation for characteristics of shedding events during condensation for two scenarios. Each and every shedding event (shedding droplet) is represented with a marker. In the baseline scenario ($U = 0\,V$), within a time-window of $200\,s$, we observe few shedding events in which the sizes of shedding droplets are relatively large (see

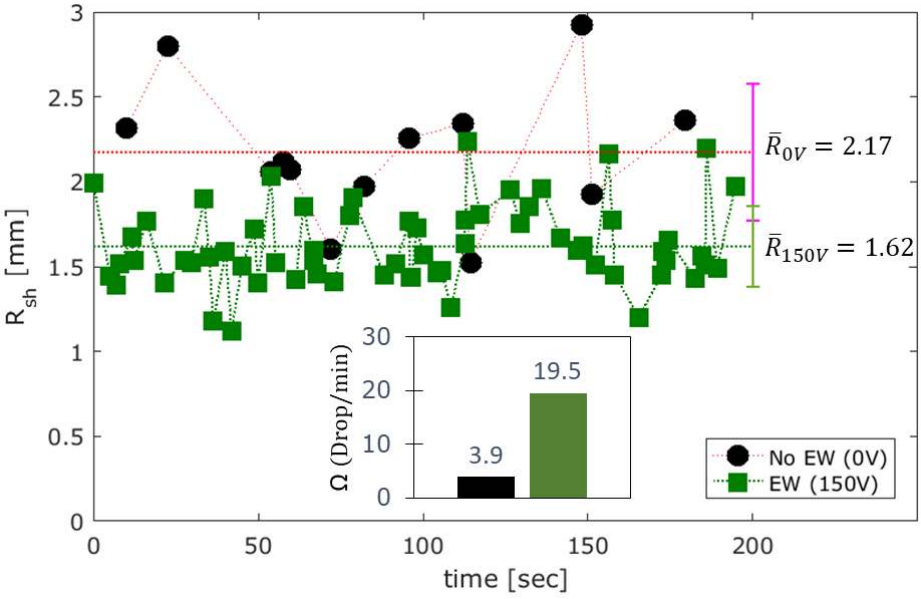

Fig.3: The radius of shedding condensate droplets with and without EW effects (0 V vs. 150V). Each marker represents a shedding event (droplet). While the shedding frequency (defined as the number of shedding droplets per unit time, and shown in the inset) is much higher under EW ($U = 150\,V\,@50\,Hz$), the average shedding radius is ~25% smaller compared to the baseline scenario ($U = 0\,V$).

black circles in Fig.3 representing each individual shedding droplet). We indicate the average shedding radius by $\bar{R} = \frac{1}{N}\sum_{i=1}^{N} R_i$ where N is the number of shedding droplets (events) and R_i is the corresponding radius of each and every shedding droplet. For the BL scenario, $\bar{R}_{0V} = 2.17\ mm$. However, for condensation under EW ($U_{rms} = 150\ V$), the results are completely different. The number of shedding events boosts up (see green squares in Fig.3 representing shedding droplets for condensation under AC-EW of 150V/50Hz). The average shedding radius decreases; $\bar{R}_{150V} = 1.62\ mm$. The shedding frequency which is defined as $\Omega = N/\Delta t$ shows 5 times higher value than the BL (no EW) case, while the average shedding size is decreased by ~25%. From this information, we can estimate the accumulated shedding volume $\dot{V} \sim [\bar{R}]^3 \cdot \Omega$ for both the scenarios. The estimations show that under EW, $\dot{V}$ is almost 2 times larger which is indeed an indication that higher heat rates would be expected from heat flow measurements.

We conduct the experiments under different EW actuations to study the sensitivity of shedding characteristics to the magnitude of electrical voltage (strength of electric fields). On top of that, we varied the AC frequency of EW, defining the rate in which electric fields alternate. Fig.4(a-b) shows the voltage dependency of shedding radius and shedding frequency respectively.

The average radii of shedding droplets are shown in Fig.4(a) for condensation under EW of 50, 100, 130, and 150 V (blue squares) as well as for no-EW scenario (black circle). The results show that the average shedding radius decrease with increasing the EW voltage. In Fig.4(b) we observe that the shedding frequency under EW boosts up e.g. quadruple number of shedding at highest voltage compared to the BL (black circle). In general, Ω increases with the electrical voltage magnitude.

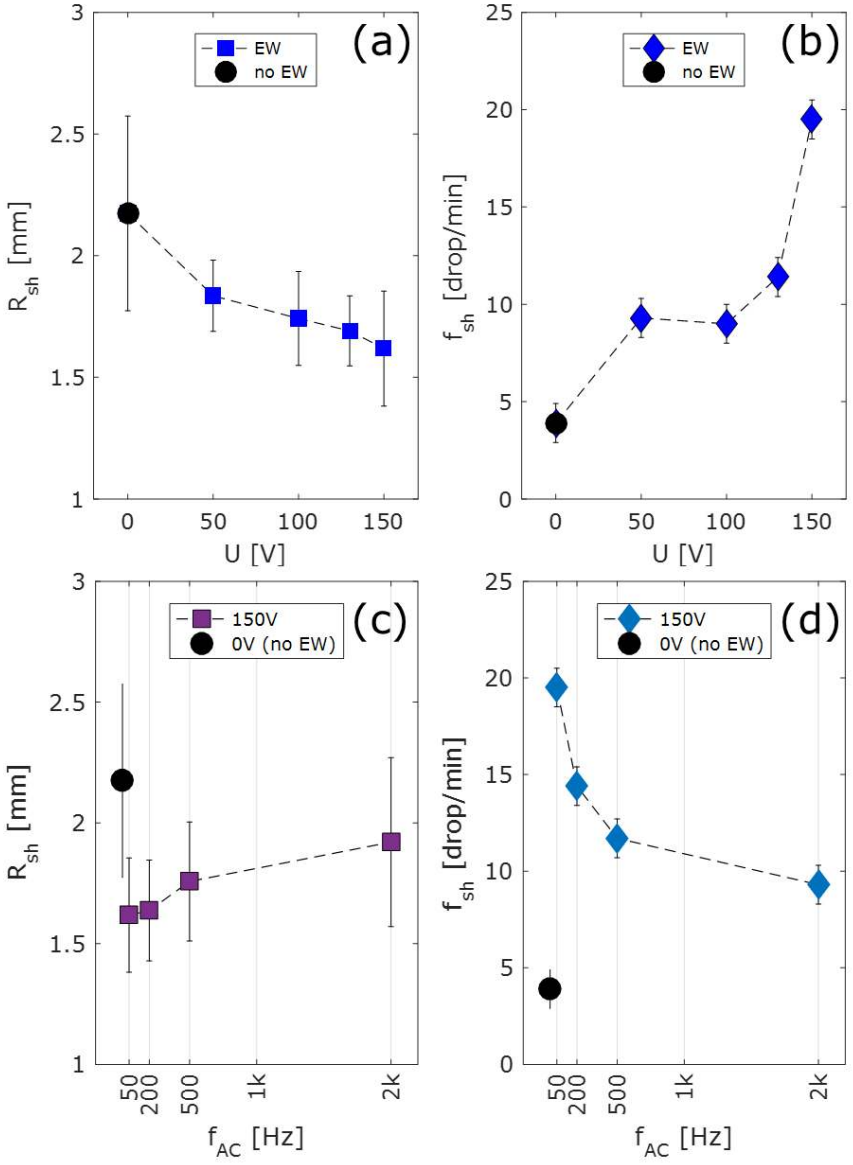

Fig.4: Shedding characteristics (radius and frequency) of condensate droplets as a function of EW voltage (a-b), and as a function of frequency of applied voltage (c-d). The dependencies are shown for EW scenarios of 50, 100, 130, and 150 V compared to the baseline scenario (0V). The dependency of shedding properties is shown for EW of 150 V at different AC frequencies of 50, 200, 500, and 2 kHz.

Fig.4(c) summarizes the results for the scenarios in which we keep the voltage level constant (at 50V) and vary the AC frequency as the other control parameter in applying an alternating electric potential. We observe that the frequency of applied voltage (f_{AC}) influences the shedding characteristics of condensate droplets. Fig.4(c) shows that, in the first place, the shedding size under EW, decreases significantly compared to the BL scenario. Note that $\bar{R}_{sh}$ scales with the AC frequency (within experimental range of 50 Hz up to 2kHz). The shedding frequency decrease to less than half with increasing the f_{AC} (see Fig.4(d)). Here, the hypothesis is that the frequency of applied AC voltage has an impact on the surface waves which are transferred towards the drop's contact line, and caused periodic movement of contact lines from the surface in specific oscillation range. At lower frequencies i.e. closer to the first couple of principal frequencies associated with millimeter-size droplets, the oscillation range is significantly larger, hence depinning of the contact line from surface heterogeneities is facilitated. Therefore, with increasing the AC frequency, EW-induced CAH suppression becomes less effective, and in between the EW experiments, the $\bar{R}_{sh}$ increases slightly with increasing the frequency.

In heat transfer applications, the efficiency of condensation process is identified by the rate of heat which is released as the result of vapor to liquid phase change, and transferred through the condensing surface. Fig.5 summarizes the results of the first direct heat transfer measurements of condensation under EW, in absence of NCG's. Fig.5(a) shows the net heat flux of condensation, conducted through the copper block, as a function of applied EW voltage. Compared to "no EW" scenario (black circle), we measure enhanced heat flux under EW. The heat flow increases with the magnitude of EW voltage. At 150V the measured heat flux of $\sim 25\ kW/m^2$ manifests $\sim 67\%$ increase in the condensation heat rate with respect to the control case.

The temporal variation of heat flux over time has been shown in the inset of Fig.5(a). Up on reaching to the set pressure in the chamber and closing of the vacuum valve (at $t = 0\ s$) the condensation process is more or less stable and consequently the heat flux remains at the corresponding level, till to the point that the vapor inlet is closed, and as a result the heat flow decreases rapidly (see the inset).

Besides the magnitude of applied EW voltage, we detect the influence of AC frequency on the heat flux. As it is depicted in Fig.5(b), the measured heat flux under EW of constant 150 V varies corresponding to different AC frequencies. Condensation heat flow decreases from $\sim 25\ kW/m^2$ at 50 Hz, down to $\sim 20\ kW/m^2$ at 2 kHz. The variation of heat flux over time for each experiment is also shown in the insets of Fig.5(b).

In essence, the change in the heat flow (q) that we measured, is the latent heat of condensation which is released in vapor-to-liquid phase change process, and is conducted from the substrate though the copper block. Hence, q is proportional to the rate of condensate formation. In steady state condition, the rate of condensation mass transfer scales with the rate of accumulated shedding volume: $q \cong \dot{m} \cdot h_{fg} \approx \rho \cdot \dot{V} \cdot h_{fg}$. Here, $\dot{m}$ is the mass flow of phase transition and h_{fg} is the latent heat of condensation for water. Hence, the volumetric accumulation of condensate would give an indication of the expected heat transfer in the experiments. From visual analysis of condensate droplets, we can estimate the total volumetric condensation rate during the time window of image recordings, by calculating the average volume of shedding droplets multiplied by the shedding frequency:

$$\dot{V} \cong \frac{2\pi}{3}(\bar{R}_{sh})^3 \cdot f_{sh}$$

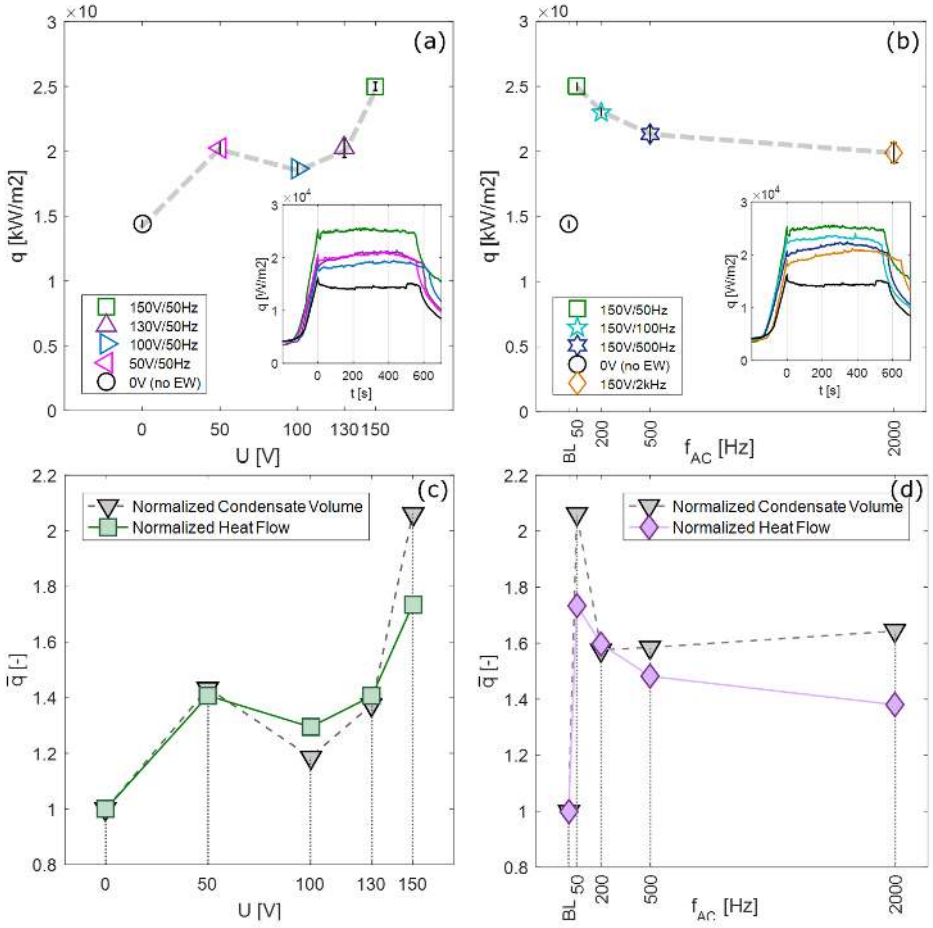

Fig.5: (a) Measured heat flux of condensation of steam on hydrophobic surface as a function of applied EW voltage magnitude: 0, 50, 100, 130, and 150 V. (b) Heat flux of condensation as a function of AC frequency: 50, 200, 500, and 2000 Hz. In both plots, the heat flow without EW (baseline scenario) is shown (back circle). The temporal variations of heat flux are depicted in the insets. (c-d) Normalized heat flux to the BL values (squares), over-stacked to normalized volumetric condensation rates which are calculated based on the average shedding radii and frequencies (triangles). The direct heat transfer measurements are in agreement with the estimations based on shedding volume calculation from analysis of the image series.

Fig.5(c) shows the volumetric condensation rate as a function of applied EW voltage, and normalized by the BL value (gray triangles). On top of this plot, the normalized heat flow from direct thermal measurements have been shown (green squares). We see that indeed, the condensation rates, estimated from the images, are in good correlation with the heat transfer measurements. For the maximum heat flow at 150V scenario, the calculated condensation rate shows a bit of overestimation compared to the direct thermal measurements. The estimated increase in condensation rate is 106% larger than BL, whereas the heat transfer measurements shows an enhancement of 74% in heat flow. Fig.5(d) shows the over-stacked plots for f_{AC} dependency. Here we see the data points of both plots at low AC frequencies, show a better agreement. At 2kHz, the estimation of condensation rate suggests a normalized value of 1.64 which is 19% more than the ration from heat transfer measurements (i.e. 1.38).

4.4. Discussion

From an applied perspective, the important KPI (Key Performance Indicator) associated with a new technology for improving the condensation applications, is the enhancement in heat transfer which correlates with the total volumetric condensation rate. In absence of NCG's, the mass flow of condensation ($\dot{m}$) is driven by the temperature gradient between the vapor (T_v) and the drop interface (T_{int}) in the direction of mass flow: $\dot{m} \sim \Delta T = T_v - T_{int}$. For a fixed surface temperature (T_{surf}) in a steady state condensation process, when the droplet grows in size, the internal thermal resistance across the droplet (between drop-substrate contact area and drop's free interface) becomes larger, hence the interface temperature increases for larger droplets ($T_{int} \gg T_{surf}$) and therefore the mass flow slows down. It has been reported in the literature that most of the heat transfer in condensation process takes place through the formation of embryo's and small droplets [27]. The larger droplets not only absorb less mass flux on their free surface, but also act like a thermal resistance against the heat flux and limit the bare surface area needed for re-nucleation. Hence, in EW-mediated condensation, more frequent sweeping of the surface more by smaller droplets, prevents formation of very large blocking droplets, and provides more bare surface for re-nucleation of embryo's, thus results in higher heat transfer rates.

4.5. Conclusions

We have shown enhanced condensation heat transfer under EW using functionalized surfaces with embedded interdigitated electrodes, and in absence of NCG's. These first direct measurements of heat transfer indicate heat flow dependency to the EW voltage magnitude as well as to the AC frequency. The thermal performance corresponding to higher voltage level and lower AC frequency (150V & 50Hz) shows 74% enhancement compared to the control case with no electric fields. Visual study of the assembly of condensate droplets confirms the change in shedding dynamics of condensate droplets under EW. We studied the sensitivity of heat flux and shedding properties to the EW parameters, and showed reduction in shedding radius, increase in shedding frequency, and enhancement in heat transfer rates with increasing the EW voltage and decreasing the AC frequency. EW-enhanced mobility of the condensate droplets through reduction in effective contact angle hysteresis as well as the enhanced coalescence manifests in smaller shedding droplets, hence faster and more frequent shedding events compared to the classical condensation on passive surfaces. EW-altered shedding characteristics results in more efficient sweeping of the surface, hence lower condensate coverage and leaves more bare area for re-nucleation. Therefore, heat flow of condensation increases under such improved shedding dynamics. In general, in absence of NCG's, the EW effect is manifested in i) higher measured heat flow, and ii) higher volumetric condensation rate, coming from increased shedding frequency of smaller shedding droplets. Both these manifestations are in more or less agreement with each other. We believe our results shed new light on active improvement of condensation process using EW in potential applications like electronic heat management, power plants, or water harvesting systems.

References

[1] M.-H. Kim and C. W. Bullard, "Air-side performance of brazed aluminum heat exchangers under dehumidifying conditions," *Int. J. Refrig.*, vol. 25, no. 7, pp. 924–934, 2002.

[2] D. Milani, A. Abbas, A. Vassallo, M. Chiesa, and D. Al Bakri, "Evaluation of using thermoelectric coolers in a dehumidification system to generate freshwater from ambient air," *Chem. Eng. Sci.*, vol. 66, no. 12, pp. 2491–2501, 2011.

[3] A. D. Khawaji, I. K. Kutubkhanah, and J.-M. Wie, "Advances in seawater desalination technologies," *Desalination*, vol. 221, no. 1–3, pp. 47–69, 2008.

[4] J. W. Rose, "Dropwise condensation theory and experiment: A review," *Proc. Inst. Mech. Eng. Part A J. Power Energy*, vol. 216, no. 2, pp. 115–128, 2002.

[5] X. Ma, J. W. Rose, D. Xu, J. Lin, and B. Wang, "Advances in dropwise condensation heat transfer: Chinese research," *Chem. Eng. J.*, vol. 78, no. 2–3, pp. 87–93, 2000.

[6] J. W. Rose, "Condensation heat transfer," *Heat Mass Transf.*, vol. 76, no. 2, pp. 143–152, 1999.

[7] K.-C. Park *et al.*, "Condensation on slippery asymmetric bumps," *Nature*, vol. 531, p. 78, Feb. 2016.

[8] J. B. Boreyko and C. H. Chen, "Self-propelled dropwise condensate on superhydrophobic surfaces," *Phys. Rev. Lett.*, vol. 103, no. 18, pp. 2–5, 2009.

[9] X. Qu *et al.*, "Self-propelled sweeping removal of dropwise condensate," *Appl. Phys. Lett.*, vol. 106, no. 22, pp. 1–5, 2015.

[10] F. Liu, J. B. Boreyko, X. Qu, and C. Chen, "Self-Propelled Jumping Condensate : Fundamental Mechanisms and Vapor-Chamber Applications," *9th Int. Conf. Boil. Condens. Heat Transf.*, no. i, 2015.

[11] J. B. Boreyko, R. R. Hansen, K. R. Murphy, S. Nath, S. T. Retterer, and C. P. Collier, "Controlling condensation and frost growth with chemical micropatterns," *Sci. Rep.*, vol. 6, no. 1, p. 19131, 2016.

[12] R. Enright, N. Miljkovic, A. Al-Obeidi, C. V Thompson, and E. N. Wang, "Condensation on superhydrophobic surfaces: the role of local energy barriers and structure length scale," *Langmuir*, vol. 28, 2012.

[13] N. Miljkovic, D. J. Preston, R. Enright, and E. N. Wang, "Electric-field-enhanced condensation on superhydrophobic nanostructured surfaces," *ACS Nano*, vol. 7, no. 12, pp. 11043–11054, 2013.

[14] N. Miljkovic *et al.*, "Jumping-Droplet-Enhanced Condensation on Scalable Superhydrophobic Nanostructured Surfaces," *Nano Lett.*, vol. 13, no. 1, pp. 179–187, 2012.

[15] A. Ghosh, S. Beaini, B. J. Zhang, R. Ganguly, and C. M. Megaridis, "Enhancing dropwise condensation through bioinspired wettability patterning," *Langmuir*, vol. 30, no. 43, pp. 13103–13115, 2014.

[16] S. Anand, A. T. Paxson, R. Dhiman, J. D. Smith, and K. K. Varanasi, "Enhanced Condensation on Lubricant- Impregnated Nanotextured Surfaces," *ACS Nano*, vol. 6, no. 11, pp. 10122–10129, 2012.

[17] P. Kim, T. Wong, J. Alvarenga, M. J. Kreder, W. E. Adorno-martinez, and K. I. M. E. T. Al, "Liquid-Infused Nanostructured Surfaces with Extreme Anti-Ice and Anti-Frost Performance," *ACS Nano*, vol. 6, no. 8, pp. 6569–6577, 2012.

[18] H. Tsuchiya *et al.*, "Liquid-Infused Smooth Surface for Improved Condensation Heat Transfer," *Langmuir*, vol. 33, no. 36, pp. 8950–8960, Sep. 2017.

[19] D. Baratian, R. Dey, H. Hoek, D. Van Den Ende, and F. Mugele, "Breath Figures under Electrowetting : Electrically Controlled Evolution of Drop Condensation Patterns," *Phys. Rev. Lett.*, vol. 120, no. 21, p. 214502, 2018.

[20] R. Dey, J. Gilbers, D. Baratian, H. Hoek, D. Van Den Ende, and F. Mugele, "Controlling shedding characteristics of condensate drops using electrowetting," *Appl. Phys. Lett.*, vol. 113, no. 24, pp. 0–5, 2018.

[21] A. T. Paxson, J. L. Yagüe, K. K. Gleason, and K. K. Varanasi, "Stable dropwise condensation for enhancing heat transfer via the initiated chemical vapor deposition (iCVD) of grafted polymer films," *Adv. Mater.*, vol. 26, no. 3, pp. 418–423, 2014.

[22] A. T. Paxson, "Condensation heat transfer on nanoengineered surfaces." Massachusetts Institute of Technology, 2011.

[23] P.-G. de Gennes, F. Brochard-Wyart, and D. Quéré, *Capillarity and Wetting Phenomena: Drops, Bubbles, Pearls, Waves*. 2004.

[24] F. Li and F. Mugele, "How to make sticky surfaces slippery: Contact angle hysteresis in electrowetting with alternating voltage," *Appl. Phys. Lett.*, vol.

92, no. 24, pp. 2008–2010, 2008.

[25] T. D. J. C. M. Mannetje, C. U. Murade, D. Van Den Ende, and F. Mugele, "Electrically assisted drop sliding on inclined planes," *Appl. Phys. Lett.*, vol. 98, no. 1, pp. 3–5, 2011.

[26] O. Manor, "Diminution of Contact Angle Hysteresis under the Influence of an Oscillating Force," *Langmuir*, vol. 30, no. 23, pp. 6841–6845, 2014.

[27] V. P. Carey, *Liquid-vapor Phase-change Phenomena: An Introduction to the Thermophysics of Vaporization and Condensation Processes in Heat Transfert Equipment*. Hemisphere publishing corporation, 1992.

5

On the shape of a droplet in a wedge

The equilibrium morphology of liquid drops exposed to geometric constraints can be rather complex. Even for simple geometries, analytical solutions are scarce. Here, we investigate the equilibrium shape and position of liquid drops confined in the wedge between two solid surfaces at an angle α. Using electrowetting, we control the contact angle and thereby manipulate the shape and the equilibrium position of aqueous drops in ambient oil. In the absence of contact angle hysteresis and buoyancy, we find that the equilibrium shape is given by a truncated sphere, at a position that is determined by the drop volume and the contact angle. At this position, the net normal force between drop and the surfaces vanishes. The effect of buoyancy gives rise to substantial deviations from this equilibrium configuration which we discuss here as well. We eventually show how the geometric constraint and electrowetting can be used to position droplets inside a wedge in a controlled way, without mechanical actuation.

This chapter has been adapted from the publication:
D. Baratian, A. Cavalli, D. van den Ende, and F. Mugele, "On the shape of a droplet in a wedge: new insight from electrowetting," *Soft Matter*, vol. 11, no. 39, pp. 7717–7721, 2015.

5.1. Introduction

Liquid bridges play an important role in our everyday life. On the beach we benefit from their stability when we build sand castles [1], while in other situations liquid bridges can be annoying, for instance when they stick our hairs together after taking a shower [2]. These bridges exert attractive or repulsive forces on the contacting surfaces, which depend on the wettability of the substrates and affect the structural properties of a system. Studying the morphology of droplets and liquid bridges in complex geometries is thus relevant in many fields, such as droplet microfluidics [3]–[5], fog harvesting and dropwise condensation [6], and oil recovery [7].

Electrowetting provides us with a unique tool to control the wetting properties of a capillary system, and as such it has been applied extensively to analyze the interplay of wettability and complex geometries [8], [9]. We have previously shown the electrowetting-induced displacement of a drop confined between a plain and a sphere, and described how the energy landscape of the drop is affected by hysteretic forces [10]. Electrowetting has also been employed to show wetting transitions for drops on fibers, which will take a "clamshell" or "barrel" configuration depending on the wettability of the fiber and the buoyancy of the system [11].

Here, we consider a drop in a wedge, representing a minimal example of a complex geometry that is encountered very often, and as such has been studied extensively [12]–[17]. Surprisingly, in most of these studies only the dynamics of drop migration [17], [18] or the motion of contact lines is investigated experimentally, which highly depend on the hysteretic properties of the surfaces

involved [14]–[16]. However, studies of equilibrium liquid morphologies are mostly limited to analytical, mathematical or numerical approaches [12], [13].

In this chapter we use electrowetting to experimentally probe the equilibrium configurations for a droplet inside a wedge. We observe that the shape of the droplet is well described by a truncated sphere, which allows us to find a simple relation between the wettability of the wedge and the position of the drop. A force balance analysis shows that a truncated sphere droplet does not exert any force on the sidewalls of the wedge, an uncommon situation for constrained droplets. We also analyze the effect of buoyancy in the system, and the deformation of the droplet due to small, finite Bond numbers.

5.2. Methods and materials

The experimental setup is depicted in Fig.1(a-b). It consists of two substrates which are fixed at a certain angle α by means of a scaffold. The substrates are glass plates, on which transparent electrodes of Indium Tin Oxide (ITO) are deposited. A layer of Parylene-C is then added by a chemical vapor polymerization process, in order to form a dielectric layer on top of the electrode.

The thickness of the insulating layer provides sufficient resistance against electrical breakdown in the electrowetting process. A Parylene layer of 2 μm in thickness is suitable for our applied AC voltage in the range of 0– 100 V RMS. To reduce the contact angle hysteresis on the substrates and to make the surface more hydrophobic, a thin layer of Teflon AF (DuPont, USA) is deposited through a dip-coating process along with a baking protocol. The surface shows a contact angle of $\theta_Y = 163°$ for our water/oil system. The contact angle hysteresis is as low as 1 degree (see Appendix 5A).

The substrates are immersed into a quartz cuvette in order to perform the experiments in an oil environment. We use water droplets (conductivity of 5 mS/cm - KCl solution) inside Bromohexadecane (Merck Millipore, USA) with a density of ϱ = 0.998 g/cm^3 for density matching experiments. Hexane (ϱ = 0.66 g/cm^3 Sigma-Aldrich, Germany) is used to test the effect of density mismatch on the shape of the drop. The voltage between the electrodes is applied at 1 KHz using a function generator (Agilent 33220A) together with a voltage amplifier (Trek PZD700A). The

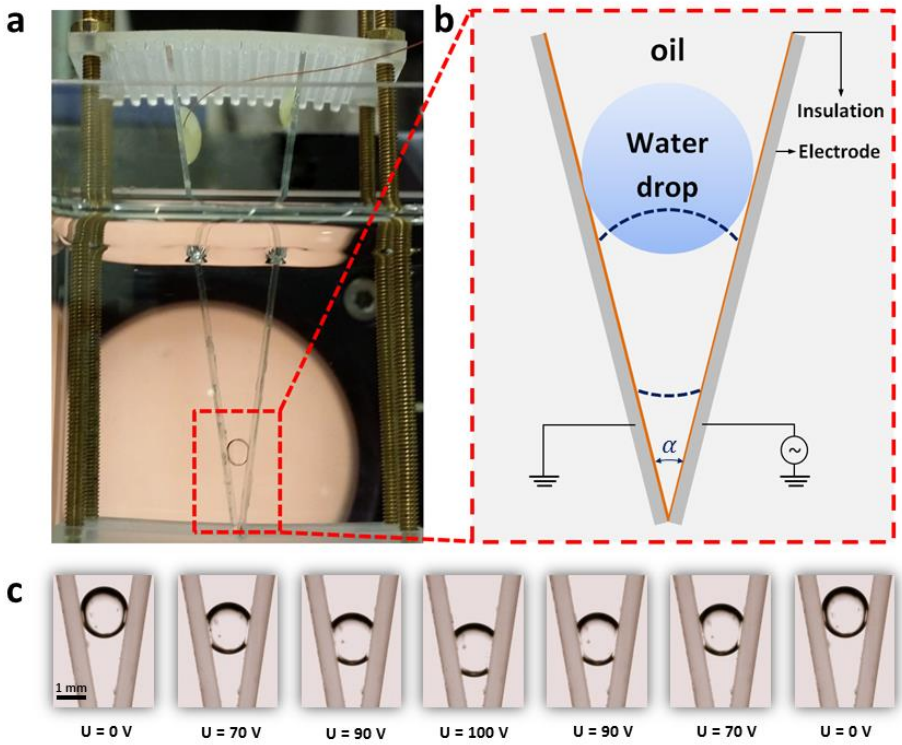

Fig.1**:** (a) Experimental setup. The substrates are fixed at an angle using a scaffold, while immersed in a cuvette filled with oil. (b) Cross-sectional schematics of the drop configuration in a wedge with an opening angle of α. (c) Series of images of the drop, showing its position in the wedge at different voltages.

droplets in the wedge are imaged by uEye camera. We use an in-house image analysis Matlab script to extract the profile of the droplets.

5.3. Experimental results

We start by considering a water droplet in Bromohexadecane. The density matching of the two liquids results in a very small Bond number ($\simeq 10^{-3}$), and makes the effect of gravity negligible.

Fig.1(c) shows selected snapshots from a typical experiment, in which a water droplet of 4 μL in volume is released inside the wedge. Upon applying voltage between the electrodes, the contact angle decreases, and the droplet moves toward the apex of the wedge. When the voltage is decreased to zero, the drop moves back towards its initial position.

We observe that, for different values of the applied voltage, the profile of the droplet resembles a section of a circle, which implies that the overall shape of the droplet is a truncated sphere. This observation is corroborated by Fig.2(b-d), which show circular fits to the profile of the droplet, for contact angles of 140°, 151°, and 162°.

In Fig.2(a) we plot the distance x_0 of the center of the droplet from the wedge apex as a function of the contact angle θ. For each recorded frame, the value of θ is obtained from the intersection of the wedge walls with the circular fits, while x_0 is the position of the center of the fitting circle. The data shown are collected over several cycles (at least 5), during which the voltage is slowly ramped up and down. We see that the displacement of the droplet is reliably reproduced over multiple cycles. We perform the experiment for a wide range of wedge angles α (see caption of Fig.2), observing that for smaller α the droplet displacement is larger.

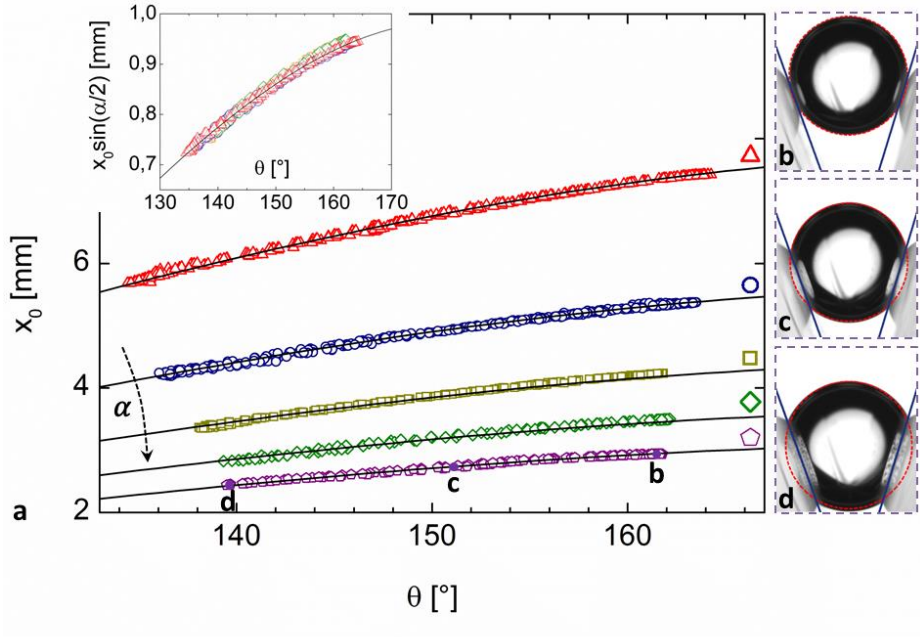

Fig.2: (a) The distance of the center of the drop from the wedge apex x_0 is plotted as a function of the contact angle θ. Data is shown for a water droplet of 4 μL in volume, and for five wedges with opening angles of 15° (red triangles), 20° (blue circles), 26° (dark yellow squares), 32° (green diamonds), and 37° (purple pentagons). A comparison between our model predictions (solid black lines) and experimental results (scattered) is shown. Each data set is extracted from several voltage cycles (ramp up to 100 V and down to 0 V for at least 5 times). Inset: Collapsed data on the master curve. (b), (c), (d): Circular fit (red lines) of the side profile of drop at three different positions in the wedge ($\theta \simeq 140°$, 151°, 162°).

The almost perfect fits of Fig.2(b-d) were achieved by eliminating all hysteretic and dynamic effects, i.e. by slowly approaching the desired voltage with loops of decreasing amplitude. If the voltage is monotonically changed, minor deformations in the shape of the moving droplet can be observed.

We also consider the effect of gravity in the form of a small, but finite Bond number ($\simeq 0.14$) on the shape of the droplet. To this end we perform experiments in which the ambient liquid is replaced by hexane. The shape of the droplet in this case is depicted in Fig.3(d-e). It is clear that the droplet is now elongated, with a higher curvature at the bottom interface.

5.4. Geometric analysis and force balance

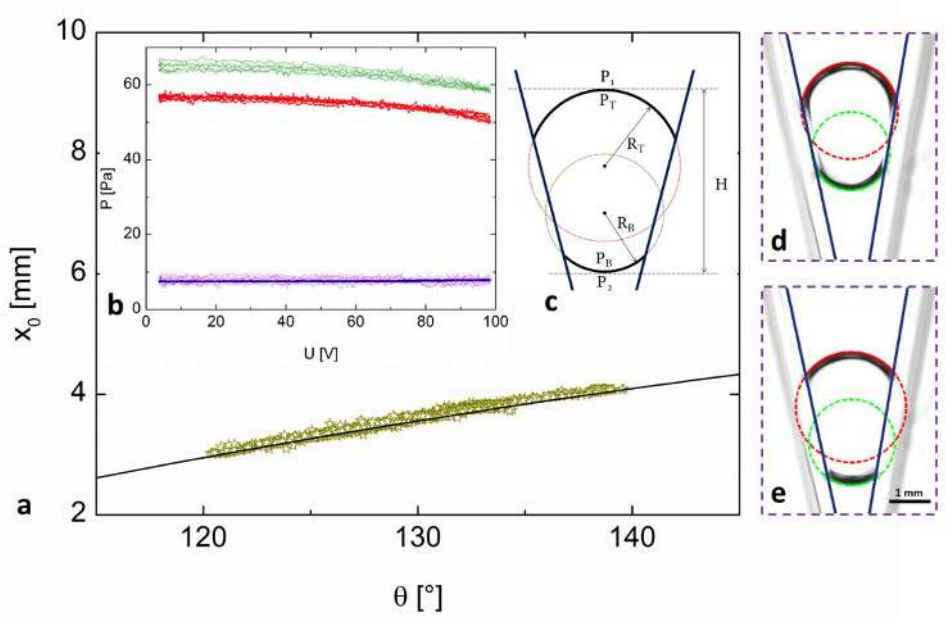

Fig.3: (a) Droplet position in a wedge ($\boldsymbol{\alpha = 22°}$) for Bo $\simeq \mathbf{0.14}$. The position of the center of the droplet is plotted versus the contact angle (dark yellow stars). (b) Pressure balance in the droplet. The difference between the Laplace pressure at the bottom interface (light green curve at the top) and the top interface (red curve in the middle) is shown in light purple (bottom scattering curve), and matches closely the hydrostatic pressure difference across the drop (bottom solid blue curve). (c) Sketch of the pressure balance in the droplet in case of density mismatch. (d) and (e) Fitting circles to the droplet profile for the top (red) and bottom (green) interfaces at 0 and 100 V, respectively.

We will first consider the density matching scenario, in which the capillary length λ_c of the system is much larger than the radius of the droplet $R \ll \lambda_c = (\sigma/g\Delta\rho)^{1/2}$: we therefore neglect the effect of gravity. If we assume a truncated spherical shape for the droplet, we can predict its radius and position inside the wedge.

We assume that the walls are identical, smooth substrates without hysteresis. The droplet will then obtain the same contact angle θ_Y with each solid surface, as prescribed by Young's relation $\cos\theta_Y = (\sigma_{so} - \sigma_{sw})/\sigma$, where σ_{so}, σ_{sw}, and σ are the solid-oil, solid-water, and water-oil interfacial tensions, respectively.

Fig.4 depicts a cross-sectional view of the droplet inside the wedge geometry. Here, α is the wedge opening angle, O is the center of the truncated sphere with radius R, and θ is the contact angle.

The volume V_{drop} of the droplet confined between the wedge walls can be calculated as: $\frac{1}{2}V_{drop} = V_{hs} - V_{cap}$, where $V_{hs} = \frac{2}{3}\pi R^3$ is the volume of a hemisphere and $V_{cap} = \frac{1}{3}\pi R^3(2 - 3\cos\varphi + \cos^3\varphi)$ the volume of the excluded spherical cap.

Since $\varphi + \theta = \pi$, so $\cos\varphi = -\cos\theta$, and we obtain $V_{drop} = \frac{2}{3}\pi R^3(\cos^3\theta - 3\cos\theta)$.

Because $V_{drop} = constant$, the radius R is a function of θ:

$$\boldsymbol{R(\theta) = \left(\frac{3V_{drop}}{2\pi\cos\theta\,(\cos^2\theta - 3)}\right)^{1/3}} \qquad \text{Eq. (1)}$$

We use x_0 to denote the distance between the wedge apex and the center of the truncated sphere. Since $\overline{OM} = R\cos\varphi = -R\cos\theta = x_0\sin(\alpha/2)$ we have:

$$\boldsymbol{x_0 = R(\theta)\frac{-\cos\theta}{\sin\ \alpha/2} = \left(\frac{3\cos^3\theta}{2\pi\cos\theta\,(3-\cos^2\theta)}\right)^{1/3}\frac{V_{drop}{}^{1/3}}{\sin\ \alpha/2}} \qquad \text{Eq. (2)}$$

As a consequence of Eq. (2), because the spherical morphology is only possible if the drop distance from the apex is larger than the radius of the droplet ($x_0/R \geq 1$), the condition $\frac{x_0}{R} = \frac{-\cos\theta}{\sin\ \alpha/2} \geq 1$ or $\theta \geq \theta_{min} = (\pi + \alpha)/2$ has to be satisfied. When the contact angle θ becomes smaller than θ_{min} the liquid fills the corner and forms a spherical cap in the wedge. This is consistent with the conditions reported by Brinkmann et. al. [13] for droplets in constrained geometries. They also discuss that a further reduction in the contact angle below $\theta_s = (\pi - \alpha)/2$ results in the liquid spreading along the wedge [19]. Distinct corner filling conditions have already been studied experimentally [16], [20]. However, investigating these liquid morphologies is beyond the scope of this paper, as the substrates are prone to damage by electrowetting due to the high electric field at their contact points.

Eq. (2) shows that the position of the drop inside the wedge is then uniquely defined by three parameters; the wedge angle α, the volume of the drop V_{drop}, and the contact angle θ.

The inset in Fig.4 shows the profile and position of a drop of 4 µL inside a wedge with opening angle α = 25° and the contact angle θ is set to 180°, 140°, and 110°. It can be seen that, for a smaller contact angle, the radius of the droplet increases, while the geometric center moves closer to the apex of the wedge.

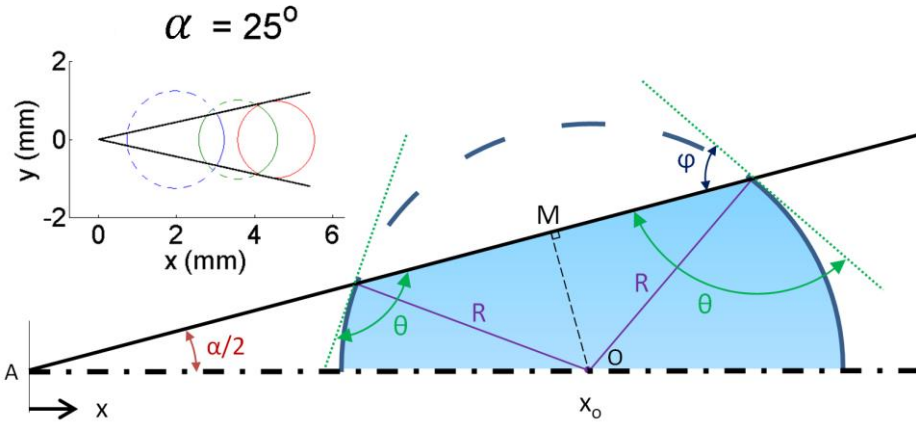

Fig.4: Cross-sectional schematic of drop inside a wedge geometry. Only half of the symmetric system is shown. The drop, in the form of a truncated sphere of radius R, is located at a distance of x_0 from the wedge apex. Inset: Different morphologies of a drop of 4 μL volume inside a wedge of 25° opening angle θ_a=180° (red), θ_b=140° (green), and θ_c=110° (blue).

The black curves in Fig.2(a) represent the position predicted from Eq. (2), for different values of α. We observe a very close agreement with the experimental data, further corroborating our truncated sphere hypothesis Eq. (2) can also be rewritten as $x_0 {V_{drop}}^{-1/3} \sin\frac{\alpha}{2} = (3\cos^3\theta/2\pi\cos\theta\,(3-\cos^2\theta))^{1/3}$, and all the data collapse to a single curve when we plot $x_0 {V_{drop}}^{-1/3} \sin\frac{\alpha}{2}$ versus θ, as shown in the inset of Fig.2(a).

We can now address the question of whether the truncated sphere described by Eq. (1) and Eq. (2) is an equilibrium morphology for the droplet. The answer consists of two separate parts: whether the shape of the droplet is in equilibrium, and whether the forces acting on its center of mass balance each other. Concerning the first point, we note that, as the curvature of the oil/water interface is constant for a sphere, the internal pressure of the droplet is homogeneous. This means that no

flow takes place inside the droplet, and therefore no deformation can occur in its profile. The shape of the droplet is thus an equilibrium one.

To evaluate the second point, we now consider the balance of the forces acting on the droplet. As the cross section of a sphere and a plane is a circle, the droplet contact line on the substrate will be a circle of radius $\tilde{R}$; hence the contact area is $\pi\tilde{R}^2$ and the contour length is $2\pi\tilde{R}$.

The force on each single wedge substrates due to the presence of the drop is then given by:

$$\underline{\boldsymbol{F}_w} = \left(2\pi\tilde{\boldsymbol{R}}\sigma \sin\boldsymbol{\theta} - \pi\tilde{\boldsymbol{R}}^2(\boldsymbol{P}_{inside} - \boldsymbol{P}_\infty)\right)\underline{\hat{\boldsymbol{n}}} \qquad \text{Eq. (3)}$$

where $\underline{\hat{n}}$ is the normal to the substrate pointing inwards the droplet, σ is the oil-water surface tension, P_{inside} is the pressure inside the droplet and P_∞ is the background pressure, as shown in Fig.5.

At equilibrium, the shape of a liquid droplet is defined by the well-known Young-Laplace equation $P_{inside} - P_\infty = \Delta P = \sigma\kappa$ which relates the mean curvature of the free interface κ and the surface tension σ to the pressure difference ΔP across the oil-water interface. Since the drop has a truncated spherical shape with radius R, the curvature of the free surface is constant and given by: $\kappa = 2/R$. Thus $P_{inside} - P_\infty = 2\sigma/R$.

Considering the relation $\tilde{R} = R\sin\varphi = R\sin\theta$, and taking into account the force and pressure argument in Eq. (3), we conclude that the force exerted on the wedge wall due to the presence of the droplet is equal to zero i.e. the force exerted by the droplet, $\pi\tilde{R}^2 P_{inside} - 2\pi\tilde{R}\sigma\sin\theta$ is equal to the force due to the ambient liquid, $\pi\tilde{R}^2 P_\infty$, acting on the backside of the substrate. This observation is quite interesting, especially in comparison to the widely encountered situation of sandwiched

droplets between parallel plates. In that case the droplet exerts an attractive or repulsive force on the plates. The only exception is when the distance between the plates and their wettability are such that the droplet assumes the shape of a truncated sphere. However, by tilting one of the plates, the droplet can maintain a spherical shape by moving sideways, so that for any contact angle larger than θ_{min} the droplet does not exert any force on the plates, regardless of the wedge opening and the volume of the drop.

As a consequence of Eq. (3), the net force of each wedge substrate on the droplet is $\pi\tilde{R}^2 P_\infty$. Hence the total force exerted on the droplet is given by:

$$\underline{\boldsymbol{F}}_{\boldsymbol{drop}} = \int_{S_1} -\boldsymbol{P}_\infty \underline{\boldsymbol{e}}_{\boldsymbol{n}} \boldsymbol{dS} + \int_{S_2} -\boldsymbol{P}_{\boldsymbol{inside}} \underline{\boldsymbol{e}}_{\boldsymbol{n}} \boldsymbol{dS} + \int_{\partial S_2} \boldsymbol{\sigma} \sin\boldsymbol{\theta}\, \underline{\boldsymbol{e}}_{\boldsymbol{n}} \boldsymbol{dl} \qquad \text{Eq. (4)}$$

where $\underline{e}_n$ is a unit vector perpendicular to the drop interface, pointing outwards. At the contact area with the wedge walls, $\underline{e}_n = -\underline{\hat{n}}$. If we cut out the substrates and substitute the equivalent force exerted from the wedge walls to the drop, we find the droplet in an isopressure field (inset of Fig.5) which results in a net zero force on the truncated spherical droplet.

$$\underline{\boldsymbol{F}}_{\boldsymbol{drop}} = -\boldsymbol{P}_\infty \int_{S_1} \underline{\boldsymbol{e}}_{\boldsymbol{n}} \boldsymbol{dS} - \boldsymbol{P}_\infty \int_{S_2} \underline{\boldsymbol{e}}_{\boldsymbol{n}} \boldsymbol{dS} = -\boldsymbol{P}_\infty \int_{S} \underline{\boldsymbol{e}}_{\boldsymbol{n}} \boldsymbol{dS} = \boldsymbol{0} \qquad \text{Eq. (5)}$$

Our geometric analysis thus shows that a truncated sphere is a viable geometry for the droplet, consistent with the geometric and volume constraint. Our force balance argument shows that no force acts on the center of mass of the droplet. We therefore conclude that the truncated sphere is an equilibrium configuration for the system.

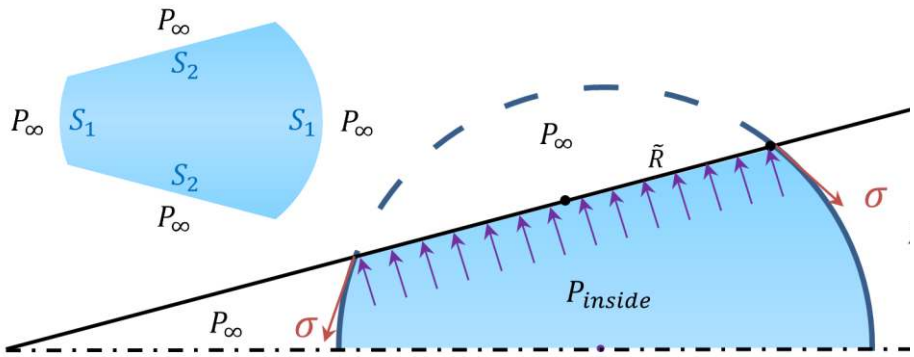

Fig.5: Schematic of the forces exerted on the drop's contact area to the substrate. The red arrows show the surface tension contribution while the purple arrows represent the sum of forces associated with pressures inside and outside the droplet. Inset: The truncated spherical drop in an isopressure field when the substrate contribution is replaced with the equivalent values.

This analysis shows that a spherical section is a solution of the Young-Laplace equation. However, there is no proof that such solution is unique [21], [22]. Our experimental results are rather interesting in this light, as we directly observe the truncated sphere shape. Moreover, the position of the droplet matches closely the prediction of Eq. (2). These observations show that, when contact angle hysteresis is negligible and the density of the droplet matches with the surrounding oil, the truncated sphere describes the equilibrium state of a droplet in a wedge very well.

Finally, we analyze the shape of the droplet when buoyancy is not negligible. Fig.3(d-e) clearly show the different curvature of the top and bottom parts of the oil/water interface, with a higher Laplace pressure at the bottom to balance the hydrostatic component. This balance can be expressed as

$$\boldsymbol{\Delta\rho g H = \sigma\kappa_{bottom} - \sigma\kappa_{top} = \sigma\left(\frac{1}{R_T} + \frac{1}{R^T{}_{out}}\right) - \sigma\left(\frac{1}{R_B} + \frac{1}{R^B{}_{out}}\right)} \quad \text{Eq. (6)}$$

where H is the height of the droplet and R_T and R_B are top and bottom radii of curvature extracted from the profile of the droplet. ${R^T}_{out}$ and ${R^B}_{out}$ are the out-of-plane radii of curvature along the other symmetry plane of the droplet, calculated at the top and bottom interfaces of the droplet, respectively. We experimentally observe that the projection of the sphere on this plane can approximately be fitted by a single circle. This means that ${R^T}_{out} = {R^B}_{out} = R_{out}$, and the out-of-plane curvature does not significantly contribute to the pressure balance, which can be rewritten as: $\Delta\rho g H = \sigma\left(\frac{1}{R_T} - \frac{1}{R_B}\right)$. In Fig.3(b) we plot the different pressure terms from Eq. (6) extracted from our experiment. The purple line shows the difference between the Laplace pressure at the top (red) and bottom (green) of the droplet. We see that this value matches closely the hydrostatic pressure contribution (in blue), meaning a complete pressure balance in the drop.

If we fit the whole interface with a *single* circular profile, we can again use Eq. (2) to predict the expected position of the droplet. Fig.3(a) shows the position x_0 of the center of the droplet vs the contact angle θ (yellow markers). Both quantities are calculated from the circular fit to the droplet profile, as in Fig.2. The black line in Fig.3(a) shows the model prediction. While the fit of the shape of the droplet to a single sphere is not as good as in Fig.2, we see that its position is still well captured. Therefore, such a small deviation from the truncated sphere shape do not significantly affect the position of the droplet in the wedge. This observation, combined with the pressure balance from Eq. (6), provides a thorough description of the droplet even for small, finite Bond numbers.

5.5. Conclusions

We used electrowetting to analyze the equilibrium shape and position of a droplet inside a wedge under different wettability conditions. Our experiments are in very good agreement with a simple analytic model, showing that the equilibrium shape of the droplet is a section of a sphere. While we cannot rule out the existence of other equilibrium configurations, we show that the spherical section model is descriptive and predictive over a wide range of contact angles and wedge openings. An interesting consequence is that we obtain a simple correlation between the position of the droplet inside the wedge and the contact angle of the system.

A finite buoyancy induces deformations in the equilibrium shape of the droplet, which we quantify. However, for small Bond numbers, the position of the droplet is still well captured by a truncated sphere description.

The precise and continuous control over the position of the droplet inside the wedge which we demonstrate suggests interesting applications in microfluidics. Compared to other designs that employ wedge geometries to move droplets, the "electrowetting in a wedge" approach is completely independent from mechanical actuation [8]. A natural application could arise from devices that already employ tapered micro-channel for other purposes, such as "on-demand drop generation" [4].

Appendix 5A: Contact angle hysteresis measurements

We conduct Advancing Receding Contact Angle (ARCA) measurements in order to extract the contact angle hysteresis (CAH) for water droplets on the substrate inside the oil environment. The advancing and receding contact angles are measured using sessile drop mode in OCA 20 (Dataphysics Inc.). The ARCA measurements are conducted at four different voltages within the same range as of the wedge experiments.

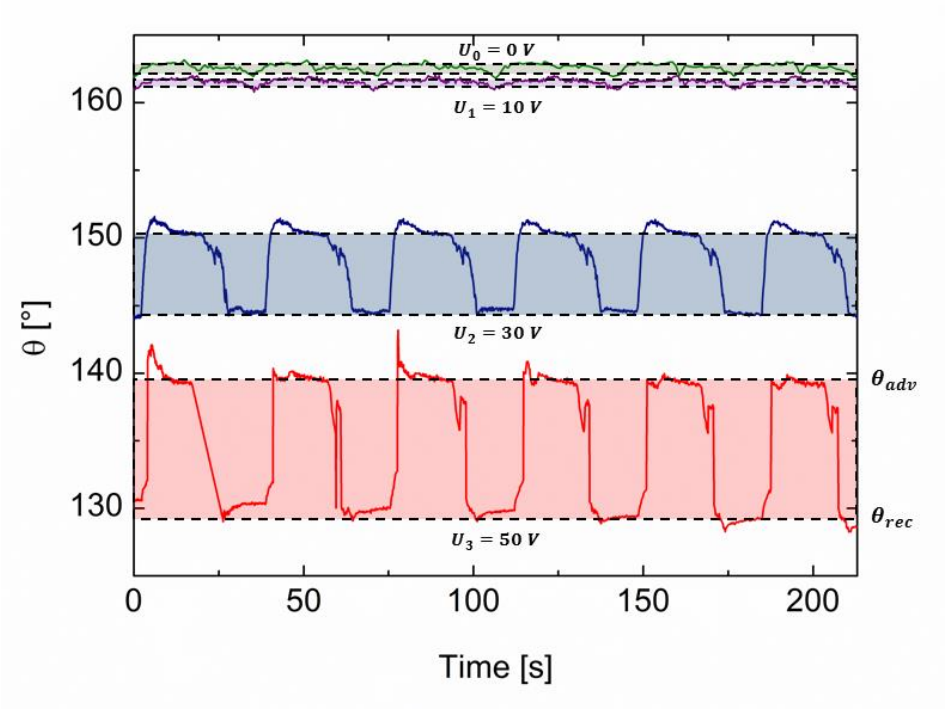

Fig.6: ARCA Measurements on the substrates. Contact angles are measured for a water droplet on the Teflon coated ITO substrates at 0 V (green), 10 V (purple), 30 V (blue), and 50 V (red) as a few effective voltages in the experiments, corresponding to approximately 1°, 0.5°, 6°, and 10° CAH respectively.

As depicted in the ARCA plot, at zero voltage, the Young angle is 163°, and we observe a small CAH as low as 1 degree (green curve). However, as we apply and then increase the voltage further, we observe a systematic increase of the CAH. This effect is likely to be related the properties of the lubrication film between the droplet and the substrate. As the Maxwell stress increases with higher voltages, the lubricant oil layer becomes unstable, and that can lead to larger contact angle hysteresis, increasing with electrowetting number. The study of the dynamics of the lubrication layer is a part of the content from the next chapter.

References

[1] A. Kudrolli, "Granular matter: Sticky sand," *Nat Mater*, vol. 7, no. 3, pp. 174–175, Mar. 2008.

[2] J. Bico, B. Roman, L. Moulin, and A. Boudaoud, "Adhesion: Elastocapillary coalescence in wet hair," *Nature*, vol. 432, no. 7018, pp. 690–690, 2004.

[3] S.-Y. Teh, R. Lin, L.-H. Hung, and A. P. Lee, "Droplet microfluidics," *Lab Chip*, vol. 8, no. 2, p. 198, 2008.

[4] R. Dangla, S. C. Kayi, and C. N. Baroud, "Droplet microfluidics driven by gradients of confinement," *Proc. Natl. Acad. Sci.*, vol. 110, no. 3, pp. 853–858, 2013.

[5] M. J. Jebrail, M. S. Bartsch, and K. D. Patel, "Digital microfluidics: a versatile tool for applications in chemistry, biology and medicine," *Lab Chip*, vol. 12, no. 14, p. 2452, 2012.

[6] C. Dorrer and J. Rühe, "Condensation and wetting transitions on microstructured ultrahydrophobic surfaces," *Langmuir*, vol. 23, no. 7, pp. 3820–3824, 2007.

[7] C. Luo and X. Heng, "Separation of oil from a water/oil mixed drop using two nonparallel plates," *Langmuir*, vol. 30, no. 33, pp. 10002–10010, 2014.

[8] A. Klingner and F. Mugele, "Electrowetting-induced morphological transitions of fluid microstructures," *J. Appl. Phys.*, vol. 95, no. 5, pp. 2918–2920, 2004.

[9] H. B. Eral *et al.*, "Drops on functional fibers: from barrels to clamshells and back," *Soft Matter*, vol. 7, no. 11, pp. 5138–5143, 2011.

[10] R. De Ruiter, C. Semprebon, M. Van Gorcum, M. H. G. Duits, M. Brinkmann, and F. Mugele, "Stability limits of capillary bridges: How contact angle hysteresis affects morphology transitions of liquid microstructures," *Phys. Rev. Lett.*, vol. 114, no. 23, pp. 1–5, 2015.

[11] Y. Zheng *et al.*, "Directional water collection on wetted spider silk," *Nature*, vol. 463, no. 7281, pp. 640–643, Feb. 2010.

[12] P. Concus and R. Finn, "Discontinuous behavior of liquids between parallel and tilted plates," *Phys. Fluids*, vol. 10, no. 1, pp. 39–43, Jan. 1998.

[13] M. Brinkmann and R. Blossey, "Blobs, channels and 'cigars': Morphologies of liquids at a step," *Eur. Phys. J. E*, vol. 14, no. 1, pp. 79–89, 2004.

[14] M. Prakash, D. Quere, and J. W. M. Bush, "Surface Tension Transport of Prey by Feeding Shorebirds: The Capillary Ratchet," *Science (80-.).*, vol. 320, no. 5878, pp. 931–934, May 2008.

[15] J. W. M. Bush, F. Peaudecerf, M. Prakash, and D. Quéré, "On a tweezer for droplets," *Adv. Colloid Interface Sci.*, vol. 161, no. 1–2, pp. 10–14, 2010.

[16] C. Luo, X. Heng, and M. Xiang, "Behavior of a Liquid Drop between Two Nonparallel Plates," *Langmuir*, Jun. 2014.

[17] J. Hong, J. K. Park, B. Koo, K. H. Kang, and Y. K. Suh, "Drop transport between two non-parallel plates via AC electrowetting-driven oscillation," *Sensors Actuators, B Chem.*, vol. 188, pp. 637–643, 2013.

[18] E. Reyssat, "Drops and bubbles in wedges," *J. Fluid Mech.*, vol. 748, pp. 641–662, 2014.

[19] P. Concus and R. Finn, "ON THE BEHAVIOR OF A CAPILLARY SURFACE IN A WEDGE," *Proc. Natl. Acad. Sci.*, vol. 63, no. 2, pp. 292–299, Jun. 1969.

[20] C. Luo, M. Xiang, and X. Heng, "A stable intermediate wetting state after a water drop contacts the bottom of a microchannel or is placed on a single corner," *Langmuir*, vol. 28, no. 25, pp. 9554–9561, 2012.

[21] P. Concus, R. Finn, and J. McCuan, "Liquid bridges, edge blobs, and Scherk-type capillary surfaces," *Indiana Univ. Math. J.*, vol. 50, no. 1, pp. 411–442, 2001.

[22] J. McCuan, *Pac. J. Math.*, vol. 180, p. 291, 1997.

6

Slippery when wet: mobility regimes of confined drops in electrowetting

The motion of confined droplets in immiscible liquid-liquid systems strongly depends on the intrinsic relative wettability of the liquids on the confining solid material and on the typical speed, which can induce the formation of a lubricating layer of the continuous phase. In electrowetting (EW), which routinely makes use of aqueous drops in ambient non-polar fluids that wet the wall material, electric stresses enter the force balance in addition to capillary and viscous forces and confinement effects. Here, we study the mobility of droplets upon EW actuation in a wedge-shaped channel, and the subsequent relaxation when the EW actuation is removed. We find that the droplets display two different mobility regimes: a fast regime, corresponding to gliding on a thin film of the ambient fluid, and a slow regime, where the film is replaced by direct contact between the droplet and the channel walls. Using a combination of experiments and numerical simulations, we show that the cross-over between these regimes arises from the interplay between the small-scale dynamics of the thin film of ambient fluid and the large-scale motion of the droplet. Our results shed light on the complex

dynamics of droplets in non-uniform channels driven by electric actuation, and can thus help the rational design of devices based on EW-driven droplet transport.

This chapter has been adapted from the publication:
D. Baratian, É. Ruiz-Gutiérrez, F. Mugele, and R. Ledesma-Aguilar, "Slippery when wet: mobility regimes of confined drops in electrowetting," *Soft Matter*, vol. 15, no. 35, pp. 7063–7070, 2019.

Note: The L-B numerical simulations in the paper (as well as in this chapter) have been done by our co-authors in Northumbria University (U.K.), and is out of scope of this thesis.

6.1. Introduction

When a voltage is applied between a droplet of a conducting liquid and a solid electrode, the droplet is observed to spread on the solid. This process, called electrowetting, has received increasing attention in the last decade [1]. This is because, on the one hand, the electrically-driven motion of a droplet on a solid is a model system to understand the interplay between electric, viscous, capillary and wetting forces in fluid dynamics [2]. On the other hand, the ability to control a liquid using electric actuation has enabled or improved many applications [2], [3], including adjustable liquid lenses [4], electronic displays [5] and droplet microfluidics [6]–[8]. Most of these applications make use of a second immiscible non-polar liquid that prevents evaporation and typically facilitates droplet actuation by acting as a lubricant [1].

During electrowetting on a flat surface, a droplet in a completely wetting ambient fluid transitions from a state of no or low initial contact with the solid to a state of partial wetting. The dynamics of this process depends on the competition between the driving electric force, the restoring capillary force, and the dissipative forces arising from the flow within the droplet, the flow within the ambient fluid, and the motion of the three-phase contact line. For sufficiently high spreading speeds, the defending ambient fluid can be entrapped between the droplet and the solid to form a thin film. That film, however, can become unstable and break up into small droplets that remain adhered to the solid [9] leading to an increased contact angle hysteresis and friction [10]. Hence, during electrowetting, a droplet can be found in one of three distinct dynamical regimes: gliding over a thin film of the ambient fluid, advancing over droplets of the ambient fluid, or displacing the ambient fluid completely.

The effect of these dynamical regimes is particularly important for the transport of droplets in channel geometries [8]. First, the mobility of the droplet can be affected by the overall structure of the flow. Second, the static electrowetting configurations of the droplet after transport may depend on whether film break-up has occurred. Third, the relaxation of the droplet upon a variation of the applied electric potential, or its complete removal, is likely to depend on the previous actuation history, leading to hysteresis [11].

Here, we study the transport of a water droplet immersed in an ambient oil phase as it undergoes a cycle of electrowetting and dewetting within a channel. To induce lateral transport in a preferred direction we use a wedge-shaped channel [12]–[18], where the droplet displays inwards motion upon electrowetting, and outwards motion when the voltage is removed [19] (dewetting). Experimentally, we study the translation of the droplet upon application and removal of different voltages. During electrowetting, droplets glide on a thin film of the ambient oil phase but suddenly slow down as the droplet touches the surface. During dewetting, droplets initially move slowly, before they detach from the solid and speed up. Numerical simulations based on a newly developed lattice-Boltzmann algorithm [20] reveal that the transition during inwards and outwards motion is in fact controlled by different mechanisms. For inwards motion, where the droplet is driven by electrowetting, the cross-over corresponds to the onset of instability of the entrapped oil film, where the critical speed depends on the applied electrowetting potential, but also on the channel geometry. For outwards motion, corresponding to spontaneous dewetting, the cross-over is controlled by the interplay between the intrinsic timescale of the receding contact line and the timescale of the large-scale motion of the drop.

6.2. Experimental setup

Fig.1 shows the experimental setup used for electrowetting-driven droplet transport in a wedge geometry [19]. Two solid walls are fixed at an angle β relative to the vertical by means of a scaffold. The walls consist of glass plates, on which transparent electrodes of Indium Tin Oxide (ITO) are deposited. A conformal thin layer of Parylene-C, of thickness $d = 2$ μm and dielectric constant $\varepsilon_d = 3.1$, is then added by a chemical vapor polymerization process. This has the purpose of creating a dielectric layer on top of the electrode that provides sufficient resistance against electrical breakdown (up to 100 V_{RMS}). To reduce the contact angle hysteresis on the substrates and to make the surface hydrophobic, a thin layer of thickness ≈ 100 nm of Teflon AF 1600 (DuPont, USA) is deposited through a dip-coating process and subsequently annealed at 180 °C for 90 min.

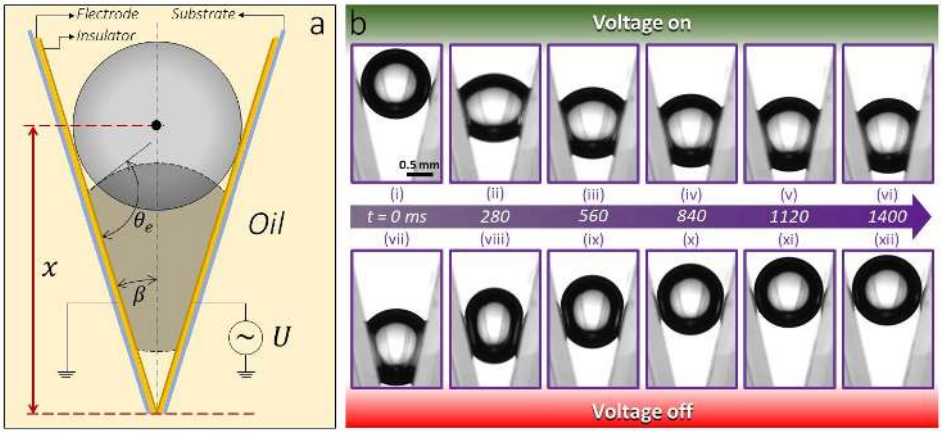

Fig.1: Droplet transport in a wedge channel driven by electrowetting (a) schematics of the static drop profile with/without applied voltage (dashed/solid contour). the position of the droplet, $x(t)$, is defined as the distance between the center of the droplet from the apex of the wedge. (b) time-lapse images of a drop of volume $V = 12$ μl in a wedge of opening angle $\beta = 12.5°$ driven by an applied voltage $U = 100$ v (top row) and dewetting upon removal of the applied voltage (bottom row).

The wedge channel is immersed in a quartz cuvette allowing to perform the experiments in an ambient oil environment. We use water droplets (conductivity of 5 mS cm^{-1} - KCl solution) in ambient Bromohexadecane (Merck Millipore, USA) with a density of $\rho_{oil} = 0.998\ \mathrm{g\ cm^{-3}}$, closely matching the density of the salt solution. The oil-water interfacial tension is $\gamma = 43\ \mathrm{mN\ m^{-1}}$. Therefore, the small difference in density of the two liquids results in a very small Bond number ($Bo = (\rho_{\mathrm{oil}} - \rho_{\mathrm{H_2O}})gR^2/\gamma \simeq 10^{-4}$) for a typical drop size $R = O(1\ \mathrm{mm})$. This minimizes the effect of gravity. Hence, in equilibrium, the free surface of the droplet takes a spherical shape, and intersects the solid with a contact angle θ_{Y} close to 180°. (Note that contact angles close below 10° and above 170° are extremely difficult to measure optically. Absolute values extracted from video snapshots can vary by several degrees depending on illumination settings and exact alignment of the viewing direction, which is difficult in the present wedge geometry. For a detailed discussion see e.g. Ref. [21].)

To induce electrowetting, an AC voltage with a frequency of 1 kHz is applied between the two planar electrodes forming the wedge using a function generator (Agilent 33220A) together with a voltage amplifier (Trek PZD700A). Throughout the present experiments, drop motion is induced by switching on an off the applied voltage with a step function in time. The droplets in the wedge are imaged with a video camera (uEye). A second camera is used to monitor the drop-substrate area through the transparent substrates. We use an in-house image analysis script (written in Matlab) to extract the profile of the droplets and their position relative to the walls of the channel.

6.3. Results

Fig.1(a) shows time-lapse images of the motion of a droplet of volume $V = 12$ µl in a wedge of opening angle $\beta = 12.5°$ during a cycle consisting of electrowetting actuation followed by spontaneous dewetting. Initially, the droplet is positioned between the two solid plates forming the wedge. Its equilibrium shape corresponds to a sphere, with an apparent contact angle $\theta_Y \approx 180°$. Applying a voltage, $U = 100$ V, leads to an abrupt reduction of the apparent contact angle to a new equilibrium value $\theta_e \approx 123°$, as expected from the Young-Lippmann equation (1),

$$\cos\theta_e = \cos\theta_Y + \eta \qquad \text{Eq. (1)}$$

where $\eta = \varepsilon_0\varepsilon_d U^2/2d\gamma$ is the electrowetting number and ε_0 is the permittivity of free space. As a consequence of the reduced contact angle, the drop moves towards the apex of the wedge, until it reaches a new equilibrium configuration, which corresponds to a truncated sphere with a voltage-dependent apparent contact angle $\theta_e(\eta)$. The final configuration is thus completely determined by θ_e, the drop volume V, and the opening angle β of the wedge [19]. The sphere is characterized by its radius $R_e = [6V/\pi(\cos 3\theta_e - 9\cos\theta_e)]^{1/3}$ and its equilibrium position $x_e = -\cos\theta_e\ R_e/\sin\beta = V^{\frac{1}{3}} f(\theta_e)/\sin\beta$. Removing the applied voltage leads to a sudden increase in the contact angle and a spontaneous translation away from the apex towards the wider region of the wedge (Fig.1(b)(vii-xii)).

6.3.1. Droplet relaxations

From the time-lapse images in Fig.1, it is clear that the morphology of the droplet during inwards and outwards displacements is very different. Upon moving inward, Fig.1(b)(i-vi), the apparent contact angle quickly decreases close to the equilibrium value θ_e corresponding to the applied voltage U as the drop gradually relaxes towards its final position. Throughout this process, there seems to be a finite contact area between the drop and the substrate. Upon dewetting, on the other hand, Fig.1(b)(vii-xii), there is a strong asymmetry between the advancing and the receding side; the contact angle stays close to $\theta_e(U)$ on the receding side (although U has been removed) and $\theta_e \approx \theta_Y$ on the advancing side. To quantify the droplet dynamics, we plot the instantaneous position of the drop center $x(t)$ with respect to the apex of the wedge channel. Fig.2(a) and Fig.2(b) show typical $x(t)$ curves for inward and outward translation. At first sight, the motion appears to follow an exponential relaxation from the initial position x_0 to the final position x_e. However, plotting the relative position $\tilde{x} = (x(t) - x_e)/(x_0 - x_e)$ on a semi-logarithmic scale

reveals that the motion is characterized by two distinct exponential relaxation processes. The inward motion is characterized by a fast (first) relaxation with a time constant τ_1, followed by a slower second relaxation regime with a time constant $\tau_2 > \tau_1$ after some cross-over time t^*. During the outward relaxation, however, the system displays a rather peculiar behavior: first there is a slow and later a faster relaxation with time constants τ_3 and τ_4 where $\tau_3 > \tau_4$.

This phenomenology was observed for the entire parameter range studied with various droplet volumes (4-12 µl), wedge angles (4.5°-12.5°), and applied voltages (60-100 V). Overall, the strength of the driving force, either during electrowetting or spontaneous dewetting, can be characterized by measuring the total lateral displacement of the droplet, $x_0 - x_e$ (note that x_0 and x_e always refer to the initial and final equilibrium droplet positions, regardless of the direction of motion). As shown in Fig.3(a), for fixed volume and wedge angle, the time constants

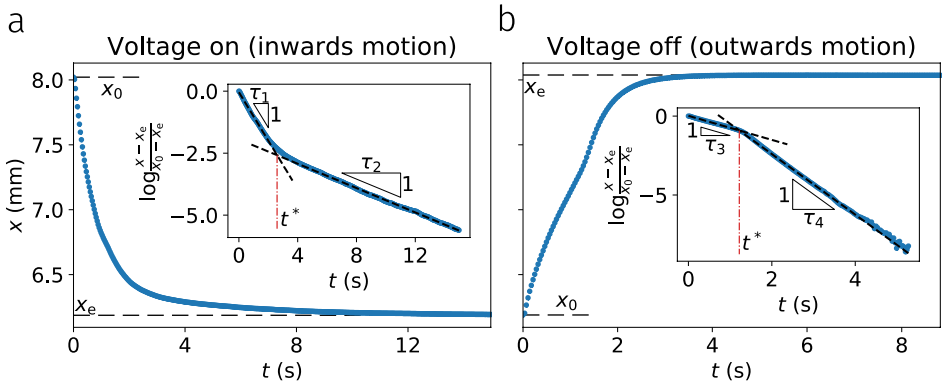

Fig.2: Time evolution of drop position during inwards (a) and outwards (b) motion. The data represents the position of a drop of $V = 8$ µL in a wedge with an opening angle of $\beta = 9°$ under application/removal of a voltage $U = 100$ V. The initial and final positions during each step of the cycle are indicated by the dashed lines. Insets: semi-log plots of the normalized displacement from the equilibrium position. Two distinct relaxation regimes for the droplet can be identified during each step, indicated by the triangles; the corresponding cross-over time, t^*, is indicated by the vertical dot-dashed lines.

of inwards motion, τ_1 and τ_2, remain approximately constant with varying driving force. This situation changes for outwards motion, where both relaxation constants τ_3 and τ_4 decrease with increasing deviation from equilibrium (see Fig.3(b)).

6.3.2. Force analysis

To understand this behavior, we consider the driving and dissipative forces acting on the droplet in more detail. Starting with the driving forces, we first consider the Helmholtz free surface energy of the drop, F, as a function of its position, x,

$$F(x; \cos\theta_e) = \gamma(A - A_{sl}\cos\theta_e). \quad (2)$$

Here, A is the free surface area of the drop (i.e. the oil-water interfacial area) and A_{sl} is the drop-substrate interfacial area. The dependence $F(x)$ can be found by constrained numerical minimization, or modeled by analytical approximation, as discussed by Ruiz-Gutiérrez *et al.* [22] For a given contact angle, F has a minimum at a position x_e, where the droplet shape is a truncated sphere with contact angle θ_e. Upon displacing the drop inward or outward from x_e, the surface energy increases, as shown in Fig.4(a). In the experiments, θ_e decreases by increasing the applied voltage, leading to a reduction of the surface energy and a corresponding decrease in the equilibrium position, x_e. Because the change in equilibrium contact angle occurs in a relatively short timescale, the droplet switches from one energy landscape, $F(x_0; \cos\theta_Y)$, to another, $F(x_0; \cos\theta_e(U))$, where $x_0 > x_e$ (see vertical

arrows in Fig.4(a)). Hence, the droplet moves inwards driven by the restoring capillary force, which corresponds to the local gradient of the curve $F(x;\cos\theta_e)$. Similarly to the situation of EW-induced drop jumping [23] the amount of energy stored in the non-equilibrium configuration of the drop is very different for the on-switching as compared to the off-switching process. Because of the asymmetry of $F(x)$, the relaxation following the on-switch process is much more gradual with an almost constant gradient, $-dF/dx$, whereas the outward relaxation upon switching

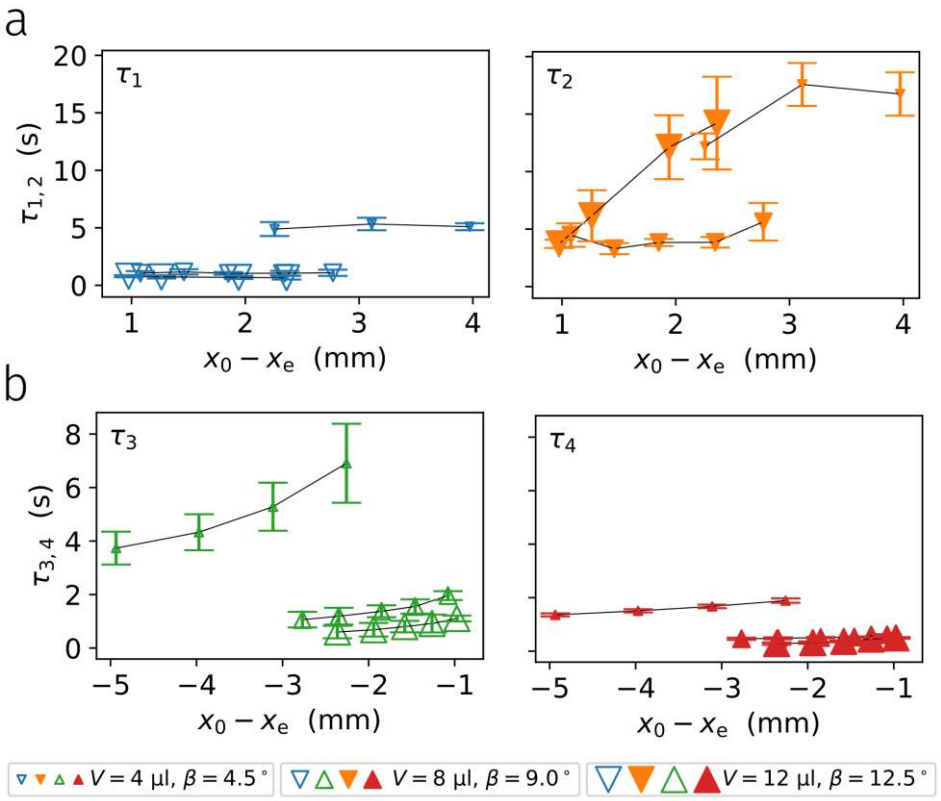

Fig.3: Relaxation time constants vs. droplet displacement for variable drop size and wedge angle, increasing with increasing symbol size (see legend). (a) Inward relaxation (voltage on); open and closed symbols correspond the relaxation times, τ_1 and τ_2. (b) Outward relaxation (voltage off – with voltage-dependent initial position x0); open and closed symbols correspond the relaxation times, τ_3 and τ_4.

off the voltage involves much steeper energy gradients due to the geometry of the wedge. This is consistent with the weak dependence of the relaxation time on the applied voltage observed in Fig.3(a) (on-switch) and the much more pronounced voltage-dependence of the off-switching process in Fig.3(b). In particular, the strong curvature of the topmost energy curve in Fig.4(a) (zero voltage) for small x implies a very strong driving force upon releasing drops that were initially pulled deep into the wedge by a high voltage.

To model the opposing dissipation forces upon drop relaxation in a wedge close to equilibrium, Ruiz-Gutiérrez *et al.* [22] considered the friction caused by the flow within the bulk of the droplet, the flow within the vicinity of the contact line, and the motion of the contact line itself. For small wedge angles, they obtained a scaling relation $\tau \propto \mu V^{1/3}/\gamma\beta^2$. Fig.4(b) shows the measured relaxation times from Fig.3 rescaled by the characteristic time, $\mu V^{1/3}/\gamma\beta^2$, as a function of the displacement from the droplet's equilibrium position (also rescaled by the length $V^{1/3}/\beta$ following refs. [19] and [22]). Rescaling to these non-dimensional parameters collapses the data for variable volumes and wedge angles (except for the largest volume and wedge angle for τ_2), suggesting that the theory of refs. [19] and [22] captures the overall scaling of the driving and dissipative forces. However, unlike the experiments in ref. [22], there is clearly no single and universal curve that describes both inward and outward relaxation. In particular, the single friction force of ref. [22] does not capture the succession of fast and slow relaxation processes as shown in Fig.2 and Fig.3.

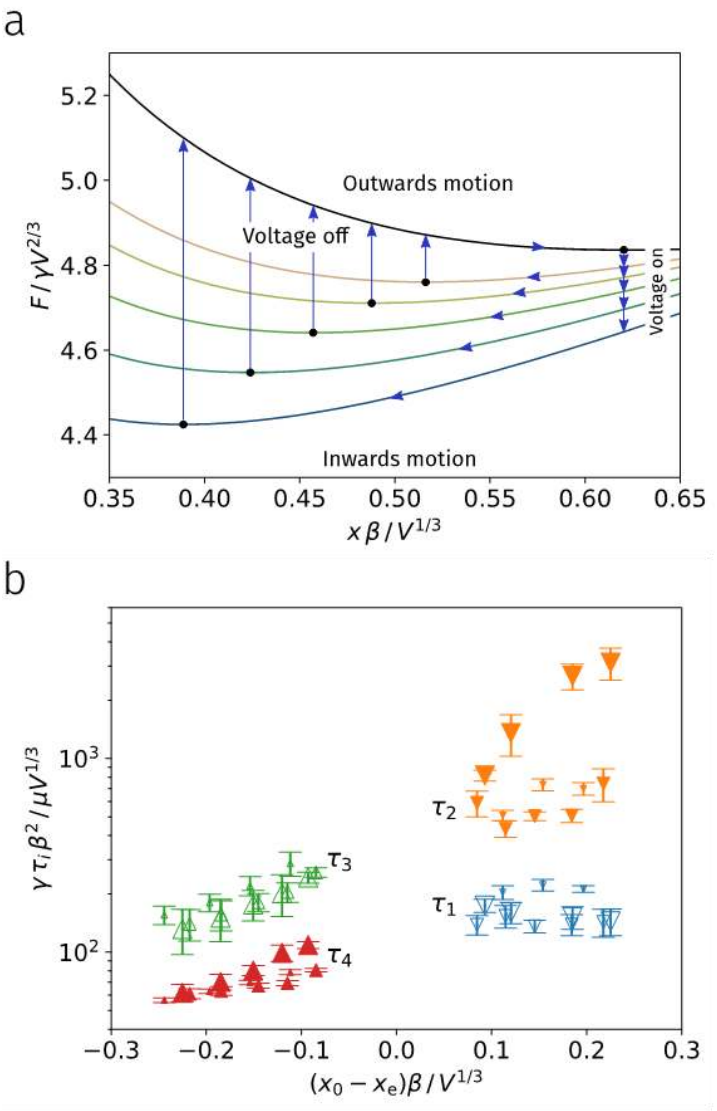

Fig.4: (a) Surface energy of droplets perturbed from their equilibrium position for different equilibrium contact angles. From bottom to top, the curves correspond to θ_e = 125°, 130°, 135°, 140°, 145° and 180°. During sudden electrowetting actuation, the apparent contact angle is reduced to $\theta_e(U)$; a droplet follows the path indicated by the arrows to find a new equilibrium position in the energy landscape, which is closer to the apex of the wedge for lower θ_e (filled circles) (b) Reduced relaxation times as a function of the initial displacement from equilibrium. The symbols correspond to the same experimental parameters reported in Fig.3.

6.3.3. Lubrication film

To understand these differences, we note that there is initially little contact between the droplet and the substrate as the voltage is applied (see first snapshot in Fig.1(b)); hence, this suggests that the faster initial motion with τ_1 originates from the entrapment of a film of the ambient oil, which allows the droplet to glide past the solid. As the droplet moves inside the wedge, the sudden change to a slower motion suggests the onset of contact between the droplet and the wall, and consequently, the formation of a contact line that slows down the interface. On the other hand, for outwards displacements the droplet is initially in contact with the walls, and its motion is limited by the presence of a contact line. The subsequent abrupt decrease in the relaxation time indicates a detachment from the solid and a re-entrant entrapment of a lubricating oil film.

In practice, the transition between film entrapment and dynamic wetting, however, can be more complex, as studied by Staicu and Mugele [9] in the context of electrowetting-induced drop spreading in ambient oil on a flat surface. As the droplet is forced to advance on the surface, ambient oil is dynamically entrapped under the droplet to form an electrowetting-induced Landau-Levich film. The thickness of this film grows as $h \sim (\mu_a v/\gamma)^{2/3}/r^{4/3}$, where v is the speed of the leading edge of the drop, and r is the apparent base radius of the droplet. Because of the Maxwell stress acting on the oil-water interface, however, the film is unstable, and breaks up into small droplets that remain adhered to the solid. This is indeed also observed in the present experiments. Fig.5(a) shows time-lapse images of a 12-µl droplet during electrowetting actuation at a voltage $U = 100$ V. The images show a view from the direction perpendicular to the mid-plane of the wedge. The yellow boxes indicate the blow-up regions presented in Fig.5(b-g). Before the potential difference is applied, the droplet shows no obvious contact with the wall (Fig.5(b)).

Upon electrowetting actuation, the droplet is forced against the wall and entraps a film of oil that eventually ruptures to form droplets (see Fig.5(c)). The oil droplets are left adhered to the wall and close the trailing droplet's edge (Fig.5(d)). As the droplet advances, the newly formed droplets create an advancing front which trails

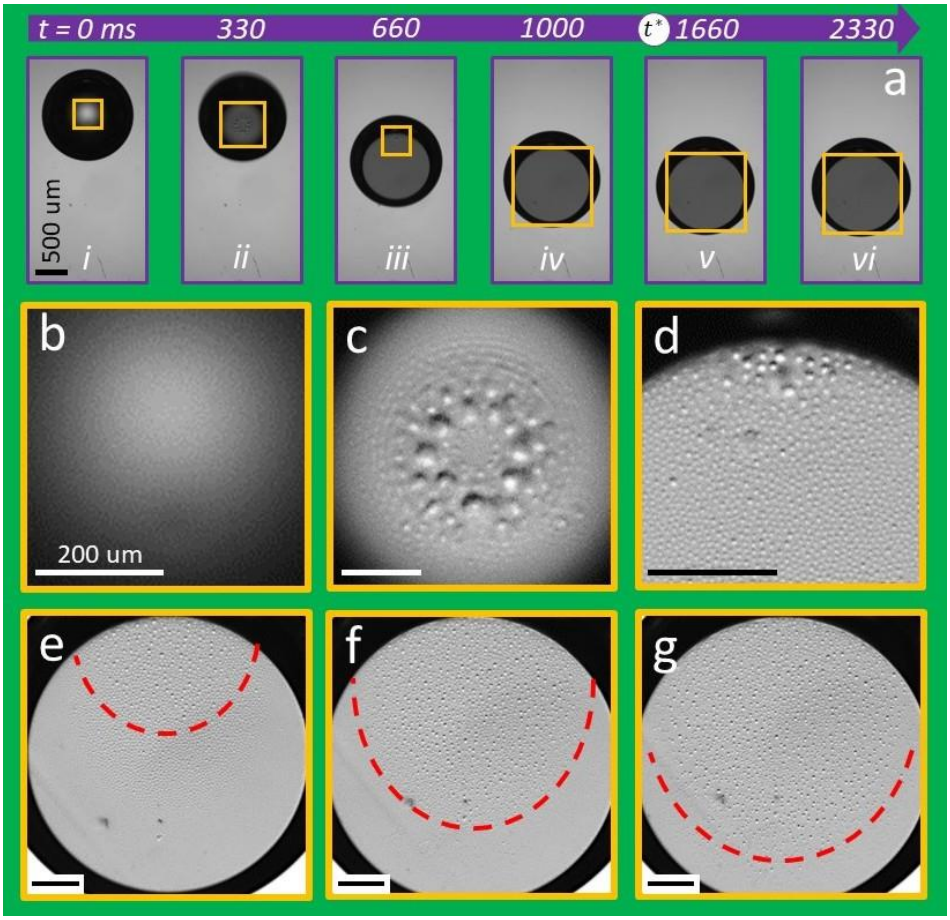

Fig.5: Side view images of droplet (V = 12 µl) during its translation in the wedge (β = 12.5°) under electrowetting (a.(i)-(viii)). (b)-(g) are zoomed-in images of (a) depicted with yellow frames. (b) drop at its initial position. (c) formation of oil droplets and instability waveforms around it upon applying electrowetting. (d) Residual large oil droplets which were formed in (c), adjacent to newly-formed smaller droplets. (e)-(f)-(g) growth of the lubricant oil instability, and expansion of the area covered by the dewetted oil droplets beneath the droplet. The scale bar in (a) is 500 μm and in (b)-(g) is 200 μm.

behind the leading droplet's edge (red dashed line in Fig.5(e-f)). Finally, as the droplet reaches an equilibrium position, the front catches up with the leading edge of the droplet (Fig.5(g)). In the experiments, the initial speed of inwards motion increases with droplet size. This is because larger droplets always sit further away from the apex of the wedge before electrowetting actuation, and thus are subject to a lower initial overall friction. As anticipated, removing the applied voltage leads to a spontaneous entrapment of the oil film at the advancing edge of the droplet, which eventually results in the full detachment of the droplet from the wall and the final relaxation to equilibrium (not shown). Hence, the observed cross-over between high and low mobility regimes in the transport of droplets is related to the transition between film entrapment, breakup, and dynamic wetting (where no droplets are present).

6.3.4. Numerical simulations

To better understand the cross-over between these regimes, Ruiz-Gutiérrez *et al* carried out numerical simulations to study the stability of a thin liquid film lying between the advancing edge of a droplet and a solid wall, where the droplet is subject to an electrostatic attraction to the wall. They used a two-dimensional diffuse-interface model to solve the coupled hydrodynamics and electrostatics equations, which we integrated using a lattice-Boltzmann algorithm [20]. The electrolytic solution is modeled as a perfect conductor whereas the oil phase is modeled as a perfect dielectric. The viscosity of the dielectric (oil) phase is set to 4 times the viscosity of the conducting (aqueous) channel of moving walls confining both fluids. The thin dielectric layer separating the liquids from the electrodes is modeled as a solid layer of uniform electric permittivity. The frame of reference is fixed to the leading edge of the droplet, which is kept at the midpoint of the channel, by adjusting the flow rate at the ends of the simulation box.

Fig.6(a) shows four representative examples of the configuration of the liquid-liquid interface as its speed, v, is varied. For sufficiently large v, a stable oil film of constant thickness, h, is entrapped between the droplet and the solid wall. Decreasing the interface speed leads to a reduction of the thickness of the film, which develops perturbations that grow as they travel downstream. These perturbations have a destabilizing effect on the film, which eventually breaks up into small drops as the conducting fluid reaches the solid and creates a contact line [9], [20]. Once a contact line is formed, there is a range of interface speeds where the contact line lags behind the rest of the interface, leading to the deposition of droplets. Finally, at sufficiently low speeds, the speed of the contact line matches that of the rest of the interface, and the motion proceeds as dynamic wetting.

The same transition from film-entrapment to dynamic wetting as the front speed is reduced occurs for different values of the applied potential, albeit at a critical speed, v^*, that increases with U. Fig.6(b) shows the corresponding "phase diagram", which we report in terms of the capillary number, $\mathrm{Ca} = \mu v/\gamma$, and the electrowetting number, η. The trajectory depicted in the figure can be used to understand the evolution of the film during the inwards motion of the droplet observed in the experiments. Initially, when the voltage is switched on, the droplet moves at a relatively high speed. Hence, a Landau-Levich film is entrapped, leading to a relatively high mobility. The droplet, however, progressively slows down as it moves into the wedge, and so the film becomes thinner, until the onset of film breakup is crossed. The resulting formation of droplets leads to a higher friction force due to the presence of multiple contact lines, slowing the droplet further.

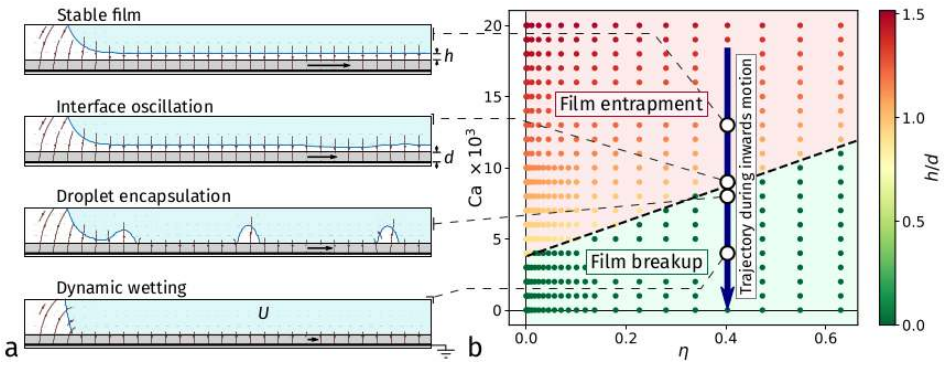

Fig.6: Lattice-Boltzmann simulations. (a) Spreading of a conducting fluid (light blue) by electrowetting on a solid dielectric (grey) of thickness d. At low speeds, a stable film oil of thickness h is entrapped between the droplet and the solid. As the speed is reduced the film develops oscillations driven by the electric field, which eventually develop as droplets. For sufficiently low speeds the film completely disappears and a stable contact line advances on the solid. The vertical axis has been expanded 2 × for visibility. The electric field is represented by the streamlines. (b) Film-entrapment and film breakup regimes as a function of the capillary and electrowetting numbers. The configurations reported in (a) are indicated by the empty circles.

Fig.7(a) shows experimental measurements of the speed of the droplet at the crossover time, $\dot{x}(t^*)$, as a function of the electrowetting number. The data show an increasing critical speed with increasing η, as expected from the simulations. The data also show a decrease in the critical speed for the smallest droplet volume and wedge angle considered in the experiments. This effect can be explained in terms of the geometry of the system: a smaller droplet has to travel a relatively longer distance into the wedge in order to create the equivalent thin-film area underneath it. This effect is amplified by at low β, where the deformation to the droplet shape caused by an equivalent displacement is also weaker. Hence, smaller droplets are

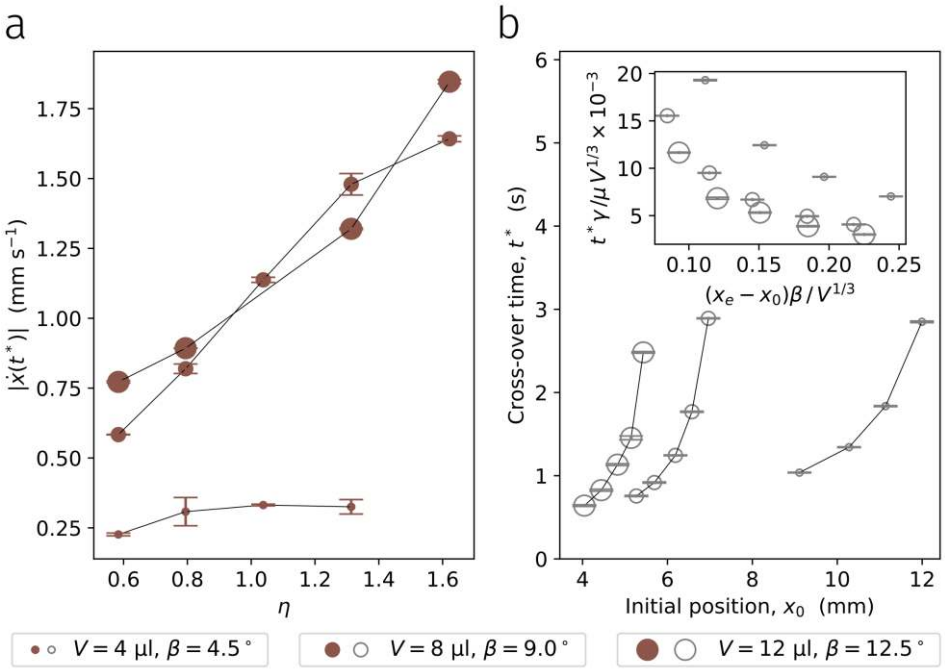

Fig.7: Cross-over during inwards and outwards motion. (a) Interface speed at the cross-over time as a function of the electrowetting number. (b) Cross-over time during outwards motion as a function of the initial position of the droplet. Inset: Data collapse in terms of the timescale of motion of the contact line and the dimensionless deformation of the interface shape.

able to travel longer distances into narrow wedges before the ambient film destabilizes, leading to lower critical speeds.

The numerical simulations also offer insights into the mechanism governing the change in mobility during outwards motion. Upon removal of the applied voltage, the droplet is pushed outwards due to the large-scale deformation of the interface. Hence, it advances at a speed that always exceeds the critical speed needed to form a Landau-Levich film. During this process, the contact lines recede as the film is formed, until the drop detaches from the solid. Fig.7(b) shows the cross-over time, t^*, as a function of the initial position of the droplet, x_0, which we use as a measure of the initial deformation of the interface. For the three data sets, t^*decreases with decreasing x_0, at a rate that depends on the droplet volume. We expect that the cross-over time is affected by the timescale of motion of the contact line, t_{cl}, but also by the timescale of translation due to the deformation of the interface. The timescale of motion of the contact line can be written as $t_{\mathrm{cl}} \sim R/v_{\mathrm{cap}}$, where $R \sim V^{1/3}$ is the base radius of the droplet and $v_{\mathrm{cap}} = \gamma/\mu$ is the capillary speed; hence, $t_{\mathrm{cl}} \sim \mu V^{\frac{1}{3}}/\gamma$. On the other hand, the deformation of the interface can be characterized by the dimensionless parameter $(x_{\mathrm{e}} - x_0)\beta/V^{1/3}$, which measures deviations of the droplet radius from equilibrium. In terms of these variables, we expect that the cross-over time obeys $t^* \sim t_{\mathrm{cl}} f(\Delta r)$ where f is a function determined by the details of the flow pattern. The rescaled data is presented in the inset of Fig.7(b); the data show a reasonable collapse, albeit with deviations for the smaller droplet volume considered, for which we observe longer cross-over times. A possible reason for this deviation is the presence of entrapped oil droplets between the larger droplets and the solid, which increase their mobility and lead to shorter cross-over times.

6.4. Conclusions

We have studied the transport of water droplets surrounded by an ambient oil phase in a channel geometry driven by electrowetting, and the subsequent relaxation process once the electrowetting actuation is removed. Experimentally, we have used a wedge geometry as a means to study the directed transport of the droplet. Upon electrowetting actuation, the droplet undergoes a translation towards the apex of the wedge, following two subsequent exponential relaxations of different characteristic timescales. At first, the droplet has a relatively high mobility, indicating that it glides over a lubricating oil film. This is followed by a low-mobility regime, indicating that the film ruptures to form contact lines that slow the droplet down. Once a droplet equilibrates to the configuration imposed by electrowetting, removing the applied voltage leads to outwards motion, where the droplet also follows two subsequent exponential translations to its original equilibrium position. Initially, the drop has a relatively low mobility due to the presence of a dewetting front. This is followed by a regime of higher mobility, indicating the detachment of the liquid-liquid interface from the channel walls. In all cases, however, the dependence of the corresponding characteristic timescale on droplet volume and wedge angle is in agreement with the theory of Ruiz-Gutiérrez *et al* [22].

We have studied the onset of film breakup during inwards motion in terms of the stability of the entrapped thin film. Using lattice-Boltzmann simulations, we have identified a similar mechanism to the electrowetting-driven destabilization of a Landau-Levich film studied by Staicu and Mugele [9]. However, in the present case of a droplet in confinement, the speed of the interface is not only set by the interplay between the driving electrowetting potential and the resistance of the Landau-Levich film, but also by the constraints imposed by the channel.

A similar situation arises during the relaxation of the droplet upon removal of the electrowetting potential. On the one hand, the timescale of dewetting from the walls is controlled by the speed of the contact line and the initial length scale covered by the drop. On the other, the translation of the droplet is affected by the channel geometry on the droplet's volume. Hence, we propose a scaling of the cross-over time to droplet detachment, which captures the experimental data well.

Hence, the mobility of droplets during electrowetting-dewetting in channel geometries is controlled by the interplay between the intrinsic timescales arising from the fluid flow at small scales, e.g., film entrapment and contact-line motion, and the timescale of the large-scale flow, which depends on the details of the channel geometry. Here we have studied the relatively simple geometry of a wedge channel as a model example. However, we expect that similar competing mechanisms controlling drop mobilities across length scales are present in more complicated channel geometries used, for example, in microfluidic platforms or in oil-recovery technologies.

Appendix 6A: Reconfiguration of droplet under EW

In the inwards motion of droplet, upon applying the electrical potential, the contact angle decreases abruptly which leads to the movement of the droplet towards the apex of the wedge. The time evolution of the curvature corresponding to the upper and lower interfaces at each and every time instant, are very similar to each other during this translation (see the variation of radii of fits to the upper and lower interfaces). There is a fast increase just after the voltage is applied due to spreading of droplet over the wedge walls, and then the radii decay together to a value corresponding to drop's radius in its new equilibrium configuration. It implies that the pressure inside the droplet is equilibrated quickly, but not the contact angles. Fig-S.1 shows that the contact angle at the bottom is slightly larger compared to the top one throughout the translation. The contact angle at the top and bottom interface represent the advancing and receding contact angles respectively as the droplet approaches the apex of the wedge. Both the angles decrease upon applying voltage and eventually reach the Young-Lippmann angle of $\theta_{EW} = 123°$ at 100 V rms. However, the lower (advancing) contact angle takes more time to decay to this asymptotic value. The spherical shape of droplet when it equilibrates after the translation has been manifested by fits to the top and bottom interfaces (green and red circles respectively). We see that; indeed, both the fitting circles are overlapping, meaning that the droplet has the same curvature at top and bottom and both the interfaces are parts of a single sphere.

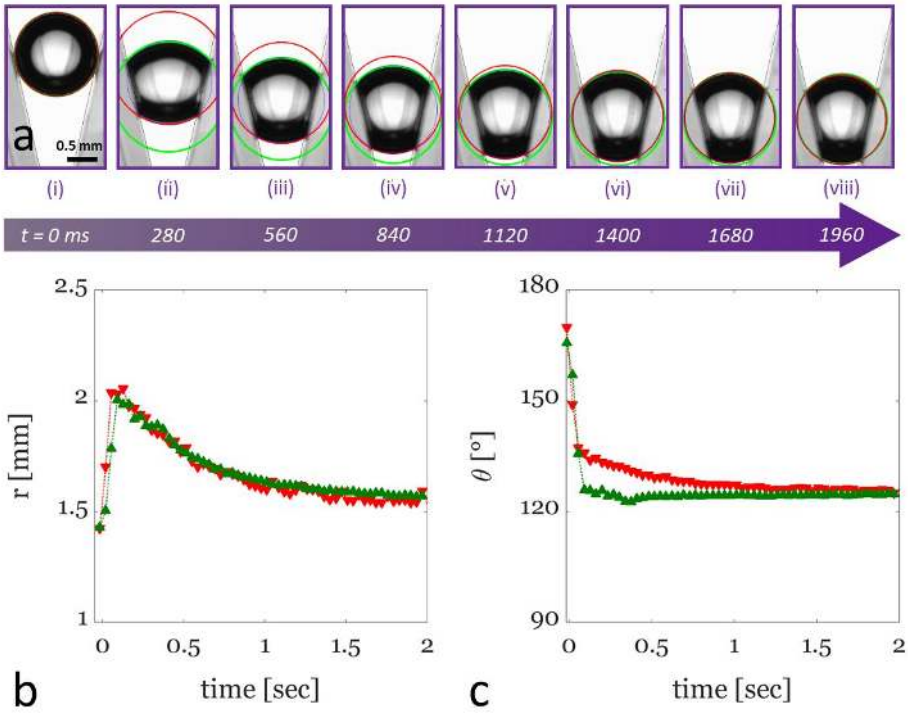

Fig-S.1: (a) time-lapse images of the drop of V=12 μL in a wedge of opening angle $\boldsymbol{\alpha = 25°}$ within a time window of $\sim\mathbf{2}$ sec starting from EW actuation of U=100 V rms (from left to tight). The series shows drop configuration in the wedge as it translates towards the wedge apex. The red (green) circles shows the fit to the drop's top (bottom) interface at each and every time instants. The time evolution of radii of the fitting circles as well as the top and bottom contact angles are shown in (d) and (e) respectively.

Appendix 6B: Position of droplet with regards to the wedge apex

In the equilibrium configuration, the position of the droplet is defined as the distance between the center of the sphere from the apex. For out of equilibrium configurations in which the droplet is not a truncated sphere anymore, we consider the intersection of the droplet with the bisector plane of the wedge which is a circle in xz plane. Then we define the position of droplet as the distance of the center of this circle from the apex.

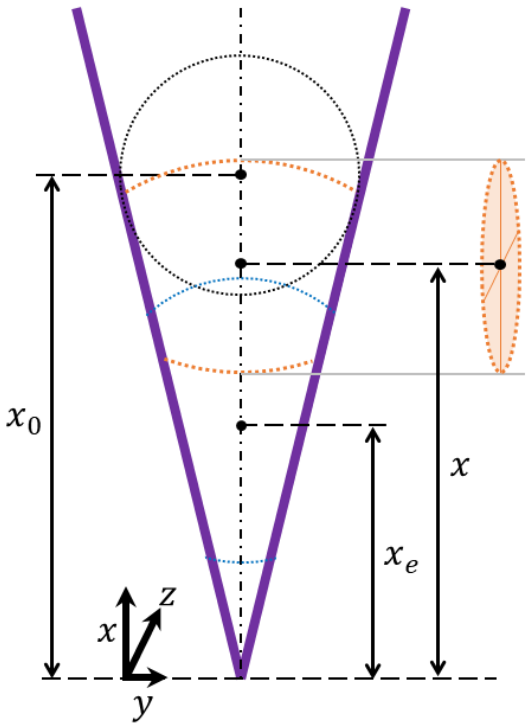

Fig-S.2: The position of the droplet is defined as the distance of its center from the wedge apex. The solid lines show the contour of the droplet in initial and final equilibrium configuration while the dashed line represents the out-of-equilibrium profile of the droplet.

Appendix 6C: Voltage dependent translation of droplet under EW

Fig-S.3 shows the position of droplet under EW for multiple voltage levels. The droplet is 8 μL in volume and the wedge opening angle is 18°. While the drop's initial position in inwards motions (terminal position in outwards motion) is the same for all the cases, the terminal (initial) position depends on the applied electrical potential.

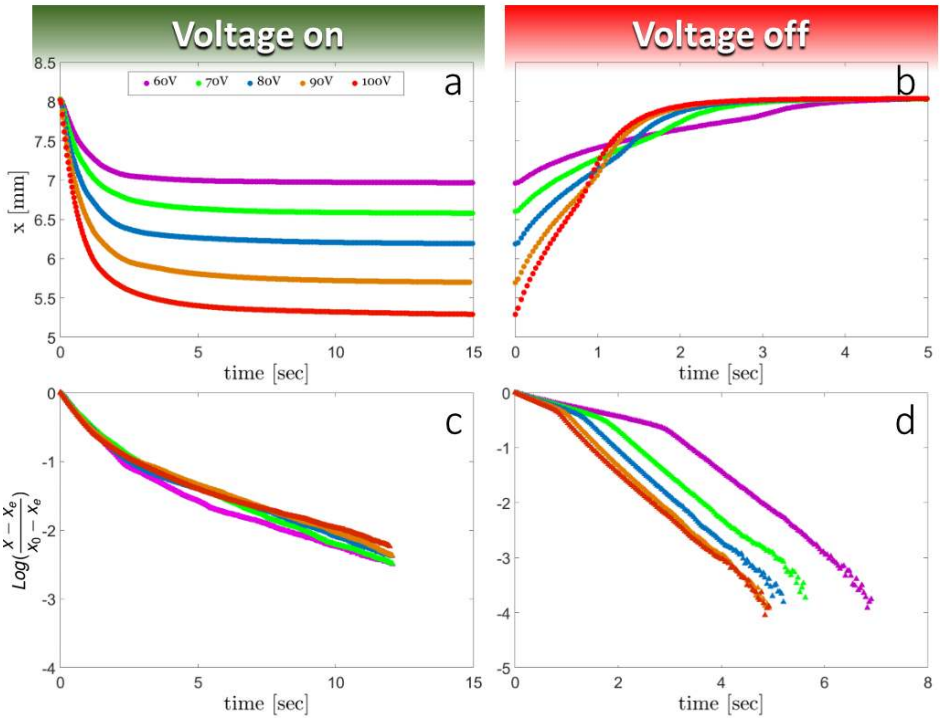

Fig-S.3: Translation of a droplet (V = 8 µL) in a wedge (α = 18°) under EW at multiple voltage levels from 60,70, 80, 90, and 100 V rms. (a) the inwards translation upon applying the voltage (b) the outwards translation upon removing the voltage. (c) and (d) are the representation of data in logarithmic scale for inwards and outwards translations respectively. The semi-log plots depict more clearly the two relaxation regimes for each case.

Appendix 6D: The LBM algorithm (this work is done outside this thesis)

The lattice-Boltzmann method integrates the hydrodynamic equations of motion by solving the discretized Boltzmann equation from Kinetic Theory. Our method makes use of three particle distribution functions to solve the hydrodynamic equations coupled with the electrostatics forces. Here, we use the D2Q9 model, i.e., 2-dimensional simulations with a 9-velocity vector set.

The hydrodynamic behavior is modelled by the Navier-Stokes equation, in the incompressible limit,

$$(\partial_t + \mathbf{v}\cdot\nabla)\mathbf{v} = -\nabla p + \rho\nu\nabla^2\mathbf{v} + \mathbf{f}, \tag{S1}$$

where ρ is the density, $\mathbf{v}$ is the velocity field, p is the pressure, ν is the kinematic viscosity and $\mathbf{f}$ are body forces which include the capillary and electric forces. Eq. (SS1) is solved by the first lattice-Boltzmann equation $f_q(\mathbf{x}+\mathbf{c}_q, t+1) = f_q(\mathbf{x},t) + \sum_{r=0}^{Q-1}\Lambda_{qr}[f - f^{\mathrm{eq}}](\mathbf{x},t)$ where $\mathbf{x}$ is the discretized position, $\{\mathbf{c}_q\}_{q=0}^{Q-1}$ is the set of velocities, and t is the discretized time variable. The momentum density of the fluid mixture is obtained by calculating the first moment of the distribution function, i.e., $\rho\mathbf{v} = \sum_{q=0}^{Q-1}\mathbf{c}_q f_q$ and the equilibrium distribution function is such that satisfies the relations: $\sum_{q=0}^{Q-1} f_q^{eq} = \rho$, $\sum_{q=0}^{Q-1}\mathbf{c}_q f_q^{eq} = \rho\mathbf{v}$ and $\sum_{q=0}^{Q-1}\mathbf{c}_q\mathbf{c}_q f_q^{eq} = \boldsymbol{\Pi} + \rho\mathbf{v}\mathbf{v}$ where $\boldsymbol{\Pi}$ is the pressure tensor such that $-\nabla\cdot\boldsymbol{\Pi} = -\nabla p + \mathbf{f}$ [24]. We use a multi-relaxation time (MRT) collision operator for stability while setting a large viscosity ratio of the conducting and dielectric phases, ν_{c} and ν_{d}, respectively (see [25] for further details).

The boundary conditions are specified following ref. [26], this is a bounce-back algorithm in which the velocity of the boundaries are prescribed. At the solid walls, the no-slip boundary condition is enforced fixing the velocity $v_{\mathrm{wall}}\hat{\mathbf{x}}$. The

driving velocity of the flow at the openings is prescribed using a parabolic profile of the vertical coordinate y, $\mathbf{v}_{\text{open}} = \left[v_{\text{wall}} - v_0\, y\left(L_y - y\right)\right]\hat{\mathbf{x}}$, where v_0 is adjusted to keep the fluid-fluid interface at a fixed position at the centre axis of the channel.

To allow motion of the contact lines after the no-slip boundary condition, we include diffusive phenomena by solving the Cahn-Hilliard equation,

$$(\partial_t + \mathbf{v}\cdot\nabla)\phi = M\nabla^2\phi, \tag{S2}$$

where $\phi = \phi(\mathbf{x}, t)$ is the phase field, i.e., a quantity that distinguishes the conducting ($\phi > 0$) from the dielectric ($\phi < 0$) phases, M is the mobility, and ϑ is the chemical potential of the fluid mixture. Eq. (SS2) is solved by using a second lattice-Boltzmann equation, $g_q\left(\mathbf{x} + \mathbf{c}_q, t+1\right) = g_q^{\text{eq}}(\mathbf{x}, t)$. We identify the field phase variable with the zeroth moment, $\phi = \sum_{q=0}^{Q-1} g_q$. The corresponding equilibrium distribution function constrained by the identities: $\sum_{q=0}^{Q-1} g_q^{eq} = \phi$, $\sum_{q=0}^{Q-1} \mathbf{c}_q g_q^{eq} = \phi\mathbf{v}$ and $\sum_{q=0}^{Q-1} \mathbf{c}_q \mathbf{c}_q g_q^{eq} = M\vartheta\mathbf{I} + \phi\mathbf{v}\mathbf{v}$.

The electrostatic forces are obtained after solving Laplace's equation for the electric potential, ψ, in the dielectric phase

$$\nabla^2\psi = 0, \tag{S3}$$

and setting it to the constant $\psi = U$ in the conducting phase.

We used a diffusive process in a similar fashion to relax the electric potential into Eq.(SS3), this can be done by proposing the third lattice-Boltzmann equation, $h_q\left(\mathbf{x} + \mathbf{c}_q, t+1\right) = h_q^{\text{eq}}(x, t)$. The equilibrium distribution function is defined such that, $\sum_{q=0}^{Q-1} h_q^{eq} = \psi$. The boundary conditions are identical to the evaporation dynamics of ref. [27], setting a value for the potential at each electrode as an open boundary.

The thermodynamic behavior of the fluids is set by defining the Helmholtz free energy of the fluid mixture, in the diffuse interface approximation,

$$F[\phi,\psi] \coloneqq \int \left[\frac{3\gamma}{\sqrt{8}\ell}\left(\frac{\phi^4}{4}-\frac{\phi^2}{2}+\frac{\ell^2}{2}|\nabla\phi|^2\right)-\frac{\epsilon}{2}|\nabla\psi|^2\right]\mathrm{d}\Omega+\int \chi\phi\,\mathrm{d}S, \tag{S4}$$

where γ is the surface tension, ℓ is a constant related to the interface thickness, and χ is called the wetting potential that can be tuned to change the wettability of the phases, and ϵ is the electric permittivity of the dielectric phase, $\mathrm{d}\Omega$ represents a differential element of volume and $\mathrm{d}S$ of surface. The chemical potential is given by $\vartheta \coloneqq \delta F/\delta\phi$, and the electric charge density, $\varrho \coloneqq -\delta F/\delta\psi$. From these, the capillary and electric forces are expressed as$\mathbf{f} \coloneqq -\phi\nabla\vartheta - \varrho\nabla\psi$. The simulation is contained in a box of size $L_x \times L_y$. All parameters are summarized in Table.1.

Table.1: Simulation parameters.

L_x	400	L_y	60
ν_c	1/12	ν_d	1/3
ρ	1	ϵ	1/3
ℓ	5	γ	8×10^{-3}
d	4	M	1

References

[1] F. Mugele and J. Heikenfeld, *Electrowetting: Fundamental Principles and Practical Applications*. John Wiley & Sons, 2018.

[2] F. Mugele and J.-C. Baret, "Electrowetting: from basics to applications," *J. Phys. Condens. Matter*, vol. 17, no. 28, pp. R705–R774, 2005.

[3] R. Shamai, D. Andelman, B. Berge, and R. Hayes, "Water, electricity, and between on electrowetting and its applications," *Soft Matter*, vol. 4, no. 1, pp. 38–45, 2007.

[4] B. Berge and J. Peseux, "Variable focal lens controlled by an external voltage: An application of electrowetting," *Eur. Phys. J. E*, vol. 3, no. 2, pp. 159–163, 2000.

[5] R. A. Hayes and B. J. Feenstra, "Video-speed electronic paper based on electrowetting," *Nature*, vol. 425, pp. 383–385, 2003.

[6] M. G. Pollack, R. B. Fair, and A. D. Shenderov, "Electrowetting-based actuation of liquid droplets for microfluidic applications," *Appl. Phys. Lett.*, vol. 77, no. 11, pp. 1725–1726, 2000.

[7] M. G. Pollack, A. D. Shenderov, and R. B. Fair, "Electrowetting-based actuation of droplets for integrated microfluidics," *Lab Chip*, vol. 2, no. 2, pp. 96–101, 2002.

[8] R. de Ruiter, A. M. Pit, V. M. de Oliveira, M. H. G. Duits, D. van den Ende, and F. Mugele, "Electrostatic potential wells for on-demand drop manipulation in microchannels," *Lab Chip*, vol. 14, no. 5, p. 883, 2014.

[9] A. Staicu and F. Mugele, "Electrowetting-induced oil film entrapment and instability," *Phys. Rev. Lett.*, vol. 97, no. 16, pp. 1–4, 2006.

[10] J. Gao, N. Mendel, R. Dey, D. Baratian, and F. Mugele, "Contact angle hysteresis and oil film lubrication in electrowetting with two immiscible liquids," *Appl. Phys. Lett.*, vol. 112, no. 20, p. 203703, May 2018.

[11] R. De Ruiter, C. Semprebon, M. Van Gorcum, M. H. G. Duits, M. Brinkmann, and F. Mugele, "Stability limits of capillary bridges: How contact angle hysteresis affects morphology transitions of liquid microstructures," *Phys. Rev. Lett.*, vol. 114, no. 23, pp. 1–5, 2015.

[12] R. Dangla, S. C. Kayi, and C. N. Baroud, "Droplet microfluidics driven by

gradients of confinement," *Proc. Natl. Acad. Sci.*, vol. 110, no. 3, pp. 853–858, 2013.

[13] J. BICO and D. QUÉRÉ, "Self-propelling slugs," *J. Fluid Mech.*, vol. 467, Sep. 2002.

[14] C. Luo, X. Heng, and M. Xiang, "Behavior of a Liquid Drop between Two Nonparallel Plates," *Langmuir*, vol. 30, no. 28, pp. 8373–8380, Jul. 2014.

[15] E. Reyssat, "Drops and bubbles in wedges," *J. Fluid Mech.*, vol. 748, pp. 641–662, Jun. 2014.

[16] J. Hong, J. K. Park, B. Koo, K. H. Kang, and Y. K. Suh, "Drop transport between two non-parallel plates via AC electrowetting-driven oscillation," *Sensors Actuators, B Chem.*, vol. 188, pp. 637–643, 2013.

[17] M. Prakash, D. Quéré, and J. W. M. Bush, "Surface tension transport of prey by feeding shorebirds: The capillary ratchet," *Science (80-.).*, vol. 320, no. 5878, pp. 931–934, 2008.

[18] É. Ruiz-Gutiérrez, J. H. Guan, B. Xu, G. McHale, G. G. Wells, and R. Ledesma-Aguilar, "Energy Invariance in Capillary Systems," *Phys. Rev. Lett.*, vol. 118, no. 21, pp. 1–5, May 2017.

[19] D. Baratian, A. Cavalli, D. van den Ende, and F. Mugele, "On the shape of a droplet in a wedge: new insight from electrowetting," *Soft Matter*, vol. 11, no. 39, pp. 7717–7721, 2015.

[20] É. Ruiz-Gutiérrez and R. A. Ledesma-Aguilar, "Lattice-Boltzmann Simulations of Electrowetting Phenomena," *Langmuir*, vol. 35, no. 14, pp. 4849–4859, 2019.

[21] B. Bera, "Ion and surfactant induced wetting transition," PhD Thesis, University of Twente, 2016.

[22] É. Ruiz-Gutiérrez, C. Semprebon, G. McHale, and R. Ledesma-Aguilar, "Statics and dynamics of liquid barrels in wedge geometries," *J. Fluid Mech.*, vol. 842, pp. 26–57, 2018.

[23] Z. Wang, D. Van Den Ende, A. Pit, R. Lagraauw, D. Wijnperlé, and F. Mugele, "Jumping drops on hydrophobic surfaces, controlling energy transfer by timed electric actuation," *Soft Matter*, vol. 13, pp. 4856–4863, 2017.

[24] M. R. Swift, E. Orlandini, W. R. Osborn, and J. M. Yeomans, "Lattice Boltzmann simulations of liquid-gas and binary fluid systems," *Phys. Rev. E*,

vol. 54, no. 5, p. 5041, 1996.

[25] K. Timm, H. Kusumaatmaja, and A. Kuzmin, "The lattice Boltzmann method: principles and practice." Springer: Berlin, Germany, 2016.

[26] X. Yin and J. Zhang, "An improved bounce-back scheme for complex boundary conditions in lattice Boltzmann method," *J. Comput. Phys.*, vol. 231, no. 11, pp. 4295–4303, 2012.

[27] R. Ledesma-Aguilar, D. Vella, and J. M. Yeomans, "Lattice-Boltzmann simulations of droplet evaporation," *Soft Matter*, vol. 10, no. 41, pp. 8267–8275, 2014.

7

Conclusion and Outlook

7.1. Conclusions

In this thesis we have employed the capabilities of electrowetting, as a powerful tool for tuning the wettability of droplets on a surface, to gain a better understanding of physics of droplets within two main contexts; i) condensate droplets, ii) droplets confined in complex structures. Our aim was to develop a comprehension of what EW brings in terms of changing the droplets behavior in each subject, and then assess how we can make use of it in the context of practical applications.

In the first domain (chapter 2-4), we have shown that we can actively control the condensate droplets on a surface (with embedded electrodes) via applying electric fields. The electrostatic energy landscape under EW (which induces migration and coalescence of condensate droplets), leads to unique breath figure

characteristics. The coalescing droplets align at the corresponding electrostatic energy minima, instead of remaining restricted at the center of mass of the parent droplets as seen in classical breath figures. The resulting periodicity of the droplet pattern under EW can be further controlled by simply tuning the electrode geometry. From a statistical analysis perspective, EW alters the size-distribution of droplet ensemble. While the breath figure patterns under EW manifests universal self-similarity prior to a critical time scale (similar to the classical condensation), the pattern of drop ensemble after a transition time (i.e. after major migration and coalescence of condensate droplets, induced by EW) shows significantly different functional form comparatively. The average radius of droplets also undergoes a rapid increase due to coalescence cascades.

Furthermore, we focus on the practical side of such an active control over the condensate droplets. We show that the variation of the breath figure characteristics under EW leads to lower surface coverage. This is potentially a driving factor to use EW for boosting the condensation rate, and therefore enhancing the energy transfer in thermal applications. Our thermal measurements show enhanced heat transfer of dropwise condensation of water under EW, in absence of NCG's. These measurements indicate that the heat fluxes depend on the EW voltage magnitude as well as to the AC frequency. The thermal performance of the system shows a max. of ~74% enhancement in heat transfer, corresponding to higher voltage levels and lower AC frequencies, when we compare it to the control case with no electric fields actuations. Image analysis of the condensate droplets confirms the change in their shedding dynamics under EW. Moreover, we study the sensitivity of heat flux and shedding properties to the EW parameters. The results show that with increasing the EW voltage and decreasing the AC frequency, the shedding radius reduces, the shedding frequency increases, and the heat transfer rates enhances. The mobility of the condensate droplets boosts through reduction in effective contact angle

hysteresis as well as the amplified coalescence. This effect is manifested in smaller shedding droplets, hence faster and more frequent shedding events compared to the classical condensation on passive surfaces. This different shedding characteristics result in more efficient sweeping of the surface by the shedding droplets, hence the surface coverage by droplets decreases, and this effect leaves more bare area on the condensing surface for re-nucleation. Therefore, heat flow of condensation increases under such improved shedding dynamics. In a nutshell, for condensation in absence of NCG's, the EW effect is manifested in i) higher measured heat flow, and ii) higher volumetric condensation rate, originating from increased shedding frequency of smaller shedding droplets. Both these manifestations show consistent results regarding the EW impacts.

In the second domain (chapter 5-6), we used electrowetting to analyze the equilibrium shape and position of a droplet between non-parallel walls. A wedge is a minimal example of a complex geometry in which a droplet can be confined. We see that the droplet maintains a consistent configuration under different wettability conditions. The experimental observations are in good agreement with a simple analytic model, showing that the equilibrium shape of the droplet is a section of a sphere. While we cannot rule out the existence of other equilibrium configurations, we showed that the spherical section model is descriptive and predictive over a wide range of contact angles and wedge openings, provided that the CAH is negligible. We obtain a simple correlation between the position of the droplet inside the wedge and the contact angle of the system. Moreover, we show that the equilibrium shape of the droplet deviates from our model in case of a finite buoyancy. However, for small Bond numbers, the position of the droplet is still well captured by a truncated sphere description.

Beyond the equilibrium analysis of the droplet where the motion was deliberately maintained in a quasi-static manner, we studied the dynamic transport of droplets in their fast deformations. We study the relaxation process of droplet once the electrowetting actuation is either applied or removed. Experimentally, we use a wedge geometry as a means to study the directed transport of the droplet. Upon electrowetting actuation, the droplet undergoes a translation towards the apex of the wedge, and this motion consists of two relaxation regimes with two distinguishable characteristic timescales. At first, the droplet has a relatively high mobility, indicating that it glides over a thick lubricating oil film. Then, the motion is followed by a low-mobility regime, indicating that the lubrication film ruptures and that slows the droplet down until the droplet equilibrates at its final spherical configuration. A similar 2-regime relaxation applies to backwards motion, once the EW voltage is removed. Initially, the drop has a relatively low mobility due to the presence of a dewetting front. Then, it is followed by a regime of higher mobility, indicating the detachment of the contact line from the walls. The dynamics of the lubricant film between the droplet and the substrate explain these distinct relaxations. We study the onset of film breakup during inwards motion in the context of the stability of the entrapped thin film. The underlying mechanism to the electrowetting-driven destabilization of the Landau-Levich film is shown by numerical calculations. In short, the speed of the liquid-liquid interface is set by the interplay between the driving electrowetting potential and the resistance of the Landau-Levich film, as well as the constraints imposed by the walls.

7.2. Outlooks

The research presented in this thesis is mainly addressing either fundamental or practical challenges for which we use the capabilities of EW as a unique tool for investigation. Afterwards, from an applied perspective, the idea is to extend these findings to the areas where EW opens up new room for improvements. These areas include the fields where active droplet control or manipulation would be of high interest. The work on the breath figures is one of the examples of using active EW control to modify the condensate patterns, thus make use of EW to boost the efficiency of condensation-based processes such as enhancing the heat transfer. There are further opportunities and fields yet to be explored.

In this context, the electrode geometry is a parameter which can be optimized further. The periodicity of the interdigitated electrodes governs the alignment patterns of condensate droplets, and can be tuned with respect to the capillary length of the condensing liquid. The electrode shape influences the EW-induced coalescence, and can impact the critical radius at which the droplet sheds down under gravity. In a follow-up study, EW-mediated condensation on zigzag electrodes has been explored [1]. The idea was that the trapezoid electrodes can be used to exert extra force, along the gradient of electric fields, to move droplets in the same direction as of gravity. The results show that such enhanced coalescence of droplets in conjunction with the electrically induced trapping effect due to the electrode geometry results in a larger shedding radius, but a lower shedding rate.

Another optimization aspect is the characteristics of applied EW itself. The impact of voltage magnitude and AC frequency on the condensate dynamics is depicted in chapter 4. However, beyond that, one can think of other smart actuation modes to enhance the shedding characteristics even further. For instance in one

attempt the electrical voltage was applied intermittently, as a containment to the trapping of droplets on zigzag electrodes [1]-[2]. Another possibility would be varying the AC frequency in correlation to the droplet growth rate to resonate the droplets at their principle eigen frequency, in order to maximize the EW-induced coalescence.

The other extension to the electrode designs in this context is the idea of active transport of condensate droplets using double-layer zigzag electrodes [3]. Hoek *et al* has used two isolated stacked zigzag electrodes that are vertically offset by half a period. Using out-of-phase actuation, they succeed to actively transport condensate down the surface in a conveyor-like behavior between electrical traps. For condensation of water in atmospheric ambient (air), a reduction of 50% in the drop shedding radius together with an increase of shedding frequency by 7 times have been reported in this study. In this work, the condensation rate is indicated by measuring the collected condensing water as well as calculating the shedding volume from image analysis of condensation images [3].

Implementation of EW-controlled condensation in larger scales – beyond the validation of this technique in research laboratories – requires significant improvement on some practical aspects such as development of durable hydrophobic coatings. The stability of the surfaces is among the items which are essentially the bottleneck to industrialization of DWC at the moment. Surface degradation has diminished the benefit of dropwise condensation on hydrophobic surfaces in phase change systems where the condensation turns into filmwise mode as the surfaces loses its hydrophobicity in such harsh environment i.e. in high temperature, pressure, and humidity. Next to the conventional Fluorinated coating such as Teflon, other alternatives need to be developed to provide proper surface chemistry for condensation applications. Super hydrophobic surfaces have not

shown promising performance when it comes to condensation as their wetting condition turns into the Wenzel state with the nucleation of droplets within the nano-structures [4]–[6]. Durable synthesized coating is an attempt to fabricate more stable condensing surfaces [7]. Liquid-infused surfaces also have shown both advantages and disadvantages in this respect [8]. These surfaces provide high mobility for droplet, originated from their low contact angle hysteresis. However, depletion of the lubricant liquid limits the stability of these surfaces significantly [9]. On top of that, "cloaking", as a common phenomenon in SLIPS surfaces, is the encapsulation of the condensate droplets by the oil film. This effect limits the vapor condensation on the droplet's surface, and can hinder easy coalescence of droplets with each other.

From a material perspective, the focus of the experiments in this thesis was on condensation of vapor into water. While a few experiments with low surface tension liquids e.g. Ethanol shows the proof of concept that the EW-actuation, significantly changes the condensation process in a pressure chamber, more extensive measurements need to be conducted to draw conclusions on the effect of electric fields with respect to phase transition of low surface tension liquids.

On the topic of EW-controlled drop manipulation between non-parallel walls, in this thesis we have demonstrated the precise and continuous control over the position of the droplet inside the wedge, which potentially raises new possibilities. and suggests interesting applications in microfluidics and droplet handling systems. Compared to some other designs in which the movement of the wedge walls are used to transport droplets, our electrowetting approach is completely independent from mechanical actuation. A natural possible application of this technique could be in the devices which already employ tapered micro-channel for specific purposes, such as on-demand drop generation. There, EW can bring an active control on the

release of the droplets, or use that for sorting purposes. Another potential idea from this concept is to implement it within an open-ended cone structure and employ the precise control of the droplet in order to adjust the volume of the immiscible ambient liquid which is confined by the droplet and tip of the cone. This way, one can set the inflow/outflow of the liquid at the opening of the cone which would be the principle idea for engineering a so-called EW-pipette!

Eventually, by looking into the future, we believe our results not only will trigger a general theoretical trend in analysis of drop condensation patterns in arbitrary energy landscapes, but also shed new light on active improvement of condensation processes using EW, in potential applications like breath figure templated self-assembly, electronic heat management, power plants, heat exchangers, and water harvesting systems.

References

[1] R. Dey, J. Gilbers, D. Baratian, H. Hoek, D. Van Den Ende, and F. Mugele, "Controlling shedding characteristics of condensate drops using electrowetting," *Appl. Phys. Lett.*, vol. 113, no. 24, pp. 0–5, 2018.

[2] H. Hoek, R. Dey, and F. Mugele, "Electrowetting-Controlled Dropwise Condensation with Patterned Electrodes: Physical Principles, Modeling, and Application Perspectives for Fog Harvesting and Enhanced Heat Transfer," *arXiv e-prints*, p. arXiv-2007, 2020.

[3] H. J. Hoek, "Enhancing dropwise condensation through active transport of drops using electrowetting." 03-Feb-2020.

[4] Y. Liu and C.-H. Choi, "Condensation-induced wetting state and contact angle hysteresis on superhydrophobic lotus leaves," *Colloid Polym. Sci.*, vol. 291, no. 2, pp. 437–445, 2013.

[5] C.-W. Lo, C.-C. Wang, and M.-C. Lu, "Scale effect on dropwise condensation on superhydrophobic surfaces," *ACS Appl. Mater. Interfaces*, vol. 6, no. 16, pp. 14353–14359, 2014.

[6] J. Cheng, A. Vandadi, and C. L. Chen, "Condensation heat transfer on two-tier superhydrophobic surfaces," *Appl. Phys. Lett.*, vol. 101, 2012.

[7] A. T. Paxson, J. L. Yagüe, K. K. Gleason, and K. K. Varanasi, "Stable dropwise condensation for enhancing heat transfer via the initiated chemical vapor deposition (iCVD) of grafted polymer films," *Adv. Mater.*, vol. 26, no. 3, pp. 418–423, 2014.

[8] S. Anand, A. T. Paxson, R. Dhiman, J. D. Smith, and K. K. Varanasi, "Enhanced Condensation on Lubricant- Impregnated Nanotextured Surfaces," *ACS Nano*, vol. 6, no. 11, pp. 10122–10129, 2012.

[9] T.-S. Wong *et al.*, "Bioinspired self-repairing slippery surfaces with pressure-stable omniphobicity," *Nature*, vol. 477, no. 7365, pp. 443–447, 2011.

Summary

Why is this important to gain a deeper understanding of the physics of droplets? How can we use the capabilities of electrowetting (EW) to this end? What are the areas where we can make use of active droplet manipulation to solve practical challenges? In this work, we focus on assemblies of condensate droplets as well as droplets confined in complex structures, to show how EW - as a powerful tool – is used to develop theoretical comprehension of each phenomenon and then employed in the context of practical applications.

On the pattern of condensate droplets on the surface, we show how EW modifies the distribution of droplets on the condensing surface by aligning the droplets along the electrode structure and by enhancing coalescence. Both these effects are governed by the electrostatic energy landscape, as described in chapter 2. There, we also provide practical insights towards optimizing applications involving dropwise condensation and how to control the condensate patterns. The impact of EW on the pattern of droplets is addressed in chapter 3. We demonstrate the significant alteration of statistical characteristics of the ensemble of droplets as the result of the migration and coalescence of condensate drops, controlled by EW. We talk about self-similarity, as a feature of droplet patterns and show how this feature deviates from its classical trend once the coalescence cascade sets in under EW, and consequently the drop size distribution undergoes a different evolution. These results suggest that the condensation performance is expected to increase, considering the changes in statistical properties under EW. Our hypothesis is proven

by heat transfer measurements as described in chapter 4, where we extend our study from a fundamental analysis towards feasibility for application opportunities. We show that dropwise condensation under alternating electric fields manifests significant changes in thermal characteristics and drop shedding dynamics compared to the classical dropwise condensation. In absence of non-condensable gases, we measure an enhanced heat transfer of ~74% with respect to the control case which is correlated to enhanced shedding dynamics of condensate droplets under EW.

On the behavior of droplets in complex structures, in chapter 5 we start with addressing the dilemma for the equilibrium morphology of liquid drops exposed to geometric constraints. The complex equilibrium shape of the droplet is monitored in different configurations between the wedge walls. While the morphology and positions of the droplet is controlled by EW, we observe that the droplet maintains a spherical shape under equilibrium conditions. The force analysis shows a net force of zero acting all over its interface. We show how the geometric constraint and EW can be used to position droplets inside a wedge in a controlled way, without mechanical actuation. Beyond the equilibrium analysis of the droplet where the motion was deliberately in a quasi-static manner, in the next chapter, we studied the dynamic transport of droplets in a wedge geometry. We analyzed the subsequent relaxation process of the droplet once the electrowetting actuation is either applied or removed. We explore the different mobility regimes and explain the characteristics of relaxation regimes by the status of lubrication layer between the droplet and the substrate during the motion. Using a combination of experiments and numerical simulations, we show that the cross-over between these regimes arises from the interplay between the small-scale dynamics of the thin film of ambient fluid and the large-scale motion of the droplet. On the practical side, our study can help the rational design of devices based on EW-driven droplet transport.

Samenvatting

Waarom is het belangrijk om een beter begrip te krijgen van het fysische gedrag van druppels? Hoe kunnen we de mogelijkheden van electrowetting (EW) hiervoor gebruiken? Op welke gebieden kunnen we actieve druppel manipulatie gebruiken om praktische problemen op te lossen? In dit werk focussen we op verzamelingen van condensatiedruppels en druppels beperkt in complexe structuren, om te laten zien hoe EW als een krachtig hulpmiddel kan worden gebruikt om een theoretisch begrip van elk fenomeen te ontwikkelen, om die vervolgens te gebruiken in de context van praktische toepassingen.

In het kader van oppervlaktedruppels laten we zien hoe EW de distributie van druppels op het condensatie oppervlak verandert door druppels langs de elektrodestructuur uit te lijnen en door de coalescentie tussen druppels te versterken. Beide effecten worden beheerst door het elektrostatische energielandschap, zoals beschreven in hoofdstuk 2. Daar geven we ook praktische inzichten voor het optimaliseren van toepassingen met druppelgewijze condensatie, en hoe we de condensatiedruppelpatronen kunnen controleren. De invloed van EW op de condensatiedruppelpatronen wordt behandeld in hoofdstuk 3. We laten zien dat vanwege de migratie encoalescentie van de druppels - gecontroleerd door EW - de statistische kenmerken van de druppelverzamelingen significant afwijken. We bespreken de zelfgelijke eigenschappen van condensatiedruppelpatronen en laten zien hoe deze eigenschap afwijkt van de klassieke trend zodra de EW-geïnduceerde coalescentie begint en de druppelgroottedistributie een andere evolutie ondergaat.

Deze resultaten suggereren, kijkende naar de statistische eigenschappen in de aanwezigheid van EW, dat de hoeveelheid condensatie zal toenemen. Deze hypothese wordt bewezen aan de hand van warmteoverdrachtsmetingen in hoofdstuk 4 waar we ons onderzoek uitbreiden van een fundamentele analyze naar mogelijkheden voor toepassingen. We laten zien dat druppelgewijze condensatie in elektrische wisselspanningsvelden significante veranderingen in thermische eigenschappen en druppelafglijdynamiek vertoont, in vergelijking met klassieke condensatie. In de afwezigheid van niet-condenseerbare gassen meten we een verhoogde warmteoverdracht van ~74% vergeleken met de referentiemetingen, wat gecorreleerd is aan een verbeterde afglijddynamiek van condensatiedruppels in de aanwezigheid van EW.

Aangaande het gedrag van druppels in complexe structuren beginnen we in hoofdstuk 5 met het aanpakken van het dilemma voor de evenwichtsmorfologie van druppels die worden blootgesteld aan geometrische beperkingen. De complexe evenwichtsvorm van de druppel wordt bestudeerd in verschillende configuraties tussen wigvormige wanden. Terwijl de morfologie en de posities van de druppels worden bepaald door EW, zien we dat de druppel bolvormig blijft onder evenwichtsomstandigheden. Analyse van de krachtbalans laat zien dat er geen nettokracht werkt op het gehele grensvlak van de druppel. We laten zien hoe de geometrische beperking in combinatie met EW kan worden gebruikt om druppels op een gecontroleerde manier te positioneren in een wig, zonder mechanische aansturing. Aansluitend aan de evenwichtsanalyse van de druppel, waarbij de beweging opzettelijk op een quasi-statische manier plaatsvond, hebben we in het volgende hoofdstuk het dynamische transport van druppels in de wig-geometrie bestudeerd. We hebben het relaxatieproces van de druppel onderzocht op het moment dat EW werd aangebracht of verwijderd. We bekijken de verschillende mobiliteitsregimes en verklaren de kenmerken van de relaxatieregimes op basis van

de status van de smeerlaag tussen de druppel en het substraat gedurende de beweging. Aan de hand van een combinatie van experimenten en numerieke simulaties laten we zien dat de transitie tussen deze regimes voortkomt uit het samenspel van de kleinschalige dynamiek van de dunne film van omringende vloeistof en de grootschalige beweging van de druppel. Ons onderzoek kan praktisch gezien helpen bij het weloverwogen ontwerpen van apparaten gebaseerd op EW-aangestuurd druppeltransport.

Scientific contributions

Scientific journals

From this thesis

Breath figures under electrowetting: electrically controlled evolution of drop condensation patterns

Physical review letters, *120*(21), p.214502. (2018)

Baratian, D., Dey, R., Hoek, H., van den Ende, D. and Mugele, F.

Electrowetting-enhanced heat transfer of dropwise condensation on functionalized surfaces using electrowetting

Under preparation (2020)

Baratian, D., Khalil, K., Dey, R., Hoek, H., Varanasi, K. and Mugele, F.

On the shape of a droplet in a wedge: new insight from electrowetting

Soft matter, *11*(39), pp.7717-7721. (2015)

Baratian, D., Cavalli, A., Van Den Ende, D. and Mugele, F.

Slippery when wet: mobility regimes of confined drops in electrowetting

Soft matter, *15*(35), 7063-7070. (2019)

Baratian, D., Ruiz-Gutiérrez, É., Mugele, F. and Ledesma-Aguilar, R.

Other publications

Controlling shedding characteristics of condensate drops using electrowetting

Applied physics letters, *113*(24), p.243703. (2018)

Dey, R., Gilbers, J., Baratian, D., Hoek, H., Van Den Ende, D. and Mugele, F.

Contact angle hysteresis and oil film lubrication in electrowetting with two immiscible liquids

Applied physics letters, 112(20), p.203703. (2018)

Gao, J., Mendel, N., Dey, R., Baratian, D. and Mugele, F.

SU-8 free-standing microfluidic probes

Biomicrofluidics, *11*(1), p.014112. (2017)

Kim, A.A., Kustanovich, K., Baratian, D., Ainla, A., Shaali, M., Jeffries, G.D.M. and Jesorka, A.

Conference contributions

Talks

68th Annual Meeting of the APS Division of Fluid Dynamics

Volume 60, Number 21

November 22nd to 24th 2015 / Boston, Massachusetts, USA

69th Annual Meeting of the APS Division of Fluid Dynamics

Volume 61, Number 20

November 20th to 22nd 2016 / Portland, Oregon, USA

MESA+ Annual Meeting

September 28th 2015 / Enschede, NL

Flow16 Fundamentals & Applications of micro-/nano-fluidics conference

2016 / Enschede, NL

MESA+ Annual Meeting

September 26th 2016 / Enschede, NL

Posters

9th International Meeting on Electrowetting and Related Micro and Electrofluidic Science and Technology

June 23rd to 25th 2014 / Cincinnati, Ohio, USA

Complex Motion in Fluids summer school (6th edition)

August 9th to 15th 2015 / Krogerup, Denmark

MESA+ Annual Meeting

September 25th 2017 / Enschede, NL

Poster award winner

FOM (Physics@Veldhoven)

2015-2017 / Veldhoven, NL

JMBC Bergursdag

2017 / Lunteren, NL

Davood Baratian was born in 1986 in Esfahan - the ancient capital city of Persia during the 16th century. Upon graduating from Sampad high school, he pursued his passion in mechanical engineering at Isfahan University of Technology (IUT) and obtained his B.Sc. degree. In 2010 he moved to Sweden once he got admitted to the Microtechnology and Nanoscience master program at Chalmers University of Technology in Gothenburg, where he also spent his internship at Volvo Technology, working on "energy harvesting for automotive sensors". He was awarded the M.Sc. degree by defending his thesis on a multidisciplinary project including microfluidics, cleanroom microfabrication, optics, and cell biology, under the supervision of dr. Gavin Jeffries, in Biophysical technology lab at Chalmers. Next, in 2013 he moved to the rainy Netherlands to start his PhD research in the Physics of Complex Fluids (PCF) group of prof. dr. Mugele at the University of Twente (UT), on the subject of controlling the behavior of droplets on surfaces by electrowetting. In 2017, he conducted a part of his PhD research in Varanasi research group at Massachusetts Institute of Technology (MIT) in Cambridge, United states. As for another research topic of his PhD project, he had a collaboration with Smart Materials & Surfaces group, Northumbria University, United Kingdom. He has communicated his research in the form of papers, posters, and talks in peer-reviewed journals, as well as (inter)national conferences. The results of his PhD research are manifested in this book.

Besides his research, he was involved in many extracurricular activities at the UT such as being a board member, and then the president of IrNUT, as well as the head of SPM at P-NUT. Apart from organizational roles, he takes an interest in design & visualization, nature photography, hiking, and sports. Since 2018 he works as a system performance data analyst and project integrator at ASML.

ISBN: 978-90-365-5009-3